

Self-assembled quantum dots in a fully tunable microcavity

Inauguraldissertation

zur

Erlangung der Würde eines Doktors der Philosophie

vorgelegt der

Philosophisch-Naturwissenschaftlichen Fakultät
der Universität Basel

von

Lukas Emanuel Greuter

aus Zürich, ZH



Basel, 2015

Originaldokument auf dem Dokumentenserver der Universität Basel edoc.unibas.ch



Dieses Werk ist lizenziert unter einer Creative-Commons Namensnennung – Nicht-kommerziell – Keine Bearbeitung 4.0 International Lizenz. Um eine Kopie dieser Lizenz einzusehen, besuchen Sie <http://creativecommons.org/licenses/by-nc-nd/4.0/>.

Genehmigt von der Philosophisch-Naturwissenschaftlichen Fakultät auf Antrag von

Prof. Dr. Richard J. Warburton

Prof. Dr. Peter Lodahl

Basel, den 19.05.2015

Prof. Dr. Jörg Schibler
Dekan



Namensnennung - Nicht kommerziell - Keine Bearbeitungen 4.0 International

(CC BY-NC-ND 4.0)

Dies ist eine alltagssprachliche Zusammenfassung der Lizenz (die diese nicht ersetzt).

Haftungsbeschränkung

Sie dürfen:

Teilen — das Material in jedwedem Format oder Medium vervielfältigen und weiterverbreiten

Der Lizenzgeber kann diese Freiheiten nicht widerrufen solange Sie sich an die Lizenzbedingungen halten.

Unter folgenden Bedingungen:



Namensnennung — Sie müssen angemessene Urheber- und Rechteangaben machen, einen Link zur Lizenz beifügen und angeben, ob Änderungen vorgenommen wurden. Diese Angaben dürfen in jeder angemessenen Art und Weise gemacht werden, allerdings nicht so, dass der Eindruck entsteht, der Lizenzgeber unterstütze gerade Sie oder Ihre Nutzung besonders.



Nicht kommerziell — Sie dürfen das Material nicht für kommerzielle Zwecke nutzen.



Keine Bearbeitungen — Wenn Sie das Material remixen, verändern oder darauf anderweitig direkt aufbauen dürfen Sie die bearbeitete Fassung der Materials nicht verbreiten.

Keine weiteren Einschränkungen — Sie dürfen keine zusätzlichen Klauseln oder technische Verfahren einsetzen, die anderen rechtlich irgendetwas untersagen, was die Lizenz erlaubt.

Hinweise:

Sie müssen sich nicht an diese Lizenz halten hinsichtlich solcher Teile des Materials, die gemeinfrei sind, oder soweit Ihre Nutzungshandlungen durch Ausnahmen und Schranken des Urheberrechts gedeckt sind.

Es werden keine Garantien gegeben und auch keine Gewähr geleistet. Die Lizenz verschafft Ihnen möglicherweise nicht alle Erlaubnisse, die Sie für die jeweilige Nutzung brauchen. Es können beispielsweise andere Rechte wie Persönlichkeits- und Datenschutzrechte zu beachten sein, die Ihre Nutzung des Materials entsprechend beschränken.

“was unsere väter schufen

war

da sie es schufen neu

bleiben wir später

den v Vätern

treu

schaffen wir neu”

– Mani Matter

Preface

The interaction of light with matter is at the heart of quantum optics, which itself enables insight into the fundamental aspects of quantum mechanics. First experimental access to this research field has been realized by coupling atoms to light. Here, the transition between discrete energy states of the atom is associated with the absorption and emission of a photon, a single quantum of the electromagnetic field. As a central aspect of quantum optics, the light–emitter interaction can be significantly enhanced by placing the emitter in optical cavity that is on resonance with the emitter. In recent years, this has led to a rapidly evolving research field known as cavity quantum electrodynamics (CQED). In CQED two different regimes are distinguished: the strong and the weak coupling regimes. In the strong coupling regime, the emitted photon is reflected from the cavity mirrors and eventually reabsorbed by the emitter. In contrast, the weak coupling regime describes the irreversible emission, where the photon leaks out of the cavity before it can be reabsorbed. Both the weak and strong coupling regimes enabled fundamental experiments for a better understanding of quantum optical phenomena.

CQED grants access to the quantum world and hence offers potentially revolutionizing applications, particularly in the field of quantum information processing. A central aspect for the successful implementation of quantum applications is the system’s scalability. Unfortunately, placing atoms deterministically inside a cavity remains technologically elaborate and hence minimizes the prospect of scaling a atom–CQED system.

A possibility to address this issue is to implement CQED in the solid state, where sophisticated fabrication strategies allow miniaturization and scalability of the system. Particularly the development of self-assembled quantum dots (QD) in semiconductors represent a promising route. QDs can be considered as artificial atoms that mimic the atomic two–level system. These structures interact strongly with light and therefore have the potential for replacing atoms in CQED. As a central advantage, QDs are naturally trapped, which greatly simplifies the deterministic incorporation into the cavity.

In recent years, many efforts have been made to couple self-assembled QDs to microcavities. Generally, the successful implementation of CQED requires a cavity with a

high quality factor Q and a low mode volume. In a majority of the approaches, the high Q /small mode volume cavities were monolithically defined around the QD, embedding the QD at a fixed position inside the cavity. Both the weak and strong coupling regimes have been reached with these systems. However, for future applications they suffer from several disadvantages. The fixed position of the QD inside the cavity minimizes the prospects for spectral tunability and spatial positioning the QD inside the cavity. Furthermore, prospects for further increasing of the cavity Q -factor and minimization of the mode volume remain limited in these systems.

In this thesis the mentioned disadvantages are addressed by developing a fully tunable miniaturized Fabry–Pérot microcavity with low mode volume. The design enables both spatial positioning of the emitter inside the cavity and spectral tunability. Successful coupling of a single QD to the microcavity is demonstrated including the strong coupling regime. Further a new approach to decrease the cavity mode volume is presented, where we demonstrate weak coupling is achieved.

The thesis is outlined as follows:

- **Chapter 1** gives an introduction to the field of CQED and elaborates the relevant aspects of a tunable microcavity.
- **Chapter 2** explains the fabrication of concave mirrors in order to achieve a small mode volume in the Fabry–Pérot cavity.
- **Chapter 3** describes and characterizes the microcavity setup.
- **Chapter 4** demonstrates the strong coupling regime, achieved with an InGaAs QD coupled to the microcavity. Here, the strong coupling regime is probed by a cross-polarized detection technique, which allowed the spectral broadening of the QD to be elucidated
- **Chapter 5** shows additional measurements in the strong coupling regime. Besides lifetime measurements, strong coupling is analyzed in a magnetic field.
- **Chapter 6** presents an approach to minimize the mode volume. Thereby an epitaxial lift-off technique has been established, which allows the transfer of a thin semiconductor layer onto a cavity mirror. A successful bonding of a layer that containing QDs is achieved resulting in a demonstration of QD weak coupling via the Purcell effect.

Contents

Preface	vii
Contents	ix
1 Background	1
1.1 Introduction to cavity quantum electrodynamics	2
1.1.1 Discussion of the CQED rates	2
1.1.2 The weak coupling regime – Purcell enhancement	3
1.1.3 Strong coupling	4
1.1.4 Collective interaction	6
1.2 Quantum Dots for CQED	7
1.2.1 Micropillars	9
1.2.2 Photonic crystals	9
1.3 Observations and applications of CQED	10
1.4 Coupling quantum dots to a tunable Fabry–Pérot microcavity	11
1.4.1 A plane–concave tunable Fabry–Pérot microcavities	11
References	20
2 CO₂ Laser ablation of miniaturized concave Fabry–Pérot mirrors	21
2.1 Introduction	22
2.2 The CO ₂ laser	22
2.2.1 Setup	22
2.2.2 Characterization of the CO ₂ laser setup	24
2.3 Fabrication and analysis of the ablated structures	26
2.3.1 Effect of high power fabrication	27
2.3.2 Additional smoothing pulse	28
2.4 Conclusion	30
References	31

3	Development and characterization of a small mode volume tunable micro-cavity	33
3.1	Introduction	34
3.2	Experimental setup	35
3.2.1	Cavity design	35
3.2.2	Top mirror fabrication	36
3.3	Optical performance	37
3.3.1	Finesse	39
3.3.2	Radius of curvature	39
3.3.3	Beam waist	41
3.3.4	Microcavity microscopy	41
3.4	Conclusion	43
	References	45
4	Strong coupling of a quantum dot in a tunable microcavity	47
4.1	Introduction	48
4.2	Setup	49
4.3	Excitation and Detection	50
4.4	Experimental results	51
4.5	Model	52
4.6	Analysis	53
4.7	Discussion	55
	References	60
5	Additional investigation of the strong coupling regime	61
5.1	Strong coupling in the magnetic field	61
5.2	Dynamics of the strong coupling regime	65
5.2.1	Interaction of the QD with the cavity in the time domain	65
5.2.2	Lifetime measurements	66
	References	69
6	Epitaxial lift-off for solid-state cavity quantum electrodynamics	71
6.1	Introduction	72
6.2	Sample	74
6.2.1	Epitaxial lif-off	75
6.2.2	Van der Waals bonding	75

6.3	Cavity characterization and performance	76
6.3.1	Measurement setup	76
6.3.2	Cavity properties	77
6.3.3	Cavity mode splitting	78
6.4	Coupling quantum dots to the cavity	80
6.4.1	Photoluminescence measurements	80
6.4.2	Lifetime measurements	81
6.4.3	Estimation of the coupling strength	82
6.5	Conclusion	83
	References	87
7	Conclusion and outlook	89
7.1	Conclusion	89
7.2	Outlook	91
7.2.1	Cavity Q -factor	91
7.2.2	Coupling strength g	91
7.2.3	Emitter decay γ	92
	References	94
	APPENDIX	95
A	Towards high cooperativity strong coupling of a quantum dot in a tunable microcavity, supplementary information	97
A.1	Sample structure	97
A.2	Model calculation (M1)	98
A.3	Model calculation (M2)	101
A.4	Contribution to signal from exciton decay	103
A.5	Bare emitter optical properties	103
	Acknowledgments	109
	Curriculum Vitae	111
	List of Publications	112

Chapter 1

Background

This chapter gives an introduction into the field of cavity quantum electrodynamics (CQED), where a single two level emitter is coupled to an optical resonator. We first discuss the relevant rates of the cavity–emitter coupling dynamics before we distinguish between the weak and the strong coupling regimes. Initial CQED experiments were performed with atoms coupled to Fabry–Pérot optical resonators. However, a lot of effort has been made in recent years to implement CQED in the solid state by coupling for example self assembled quantum dots (QDs) to photonic crystals or micropillars. These systems enabled the accomplishment of various CQED experiments, but they suffer from severe disadvantages such as limited spectral tuning and limitations in the performance of the optical cavity. We motivate a possibility that incorporates quantum dots coupled to tunable miniaturized Fabry–Pérot microcavities, in order to circumvent these drawbacks in future CQED experiments.

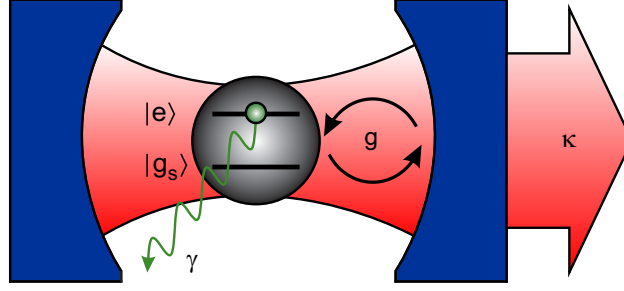


Figure 1.1. A two level emitter coupled to an optical resonator, where $|g_s\rangle$ ($|e\rangle$) denotes the ground (excited) state. The relevant CQED rates are indicated as g for the cavity–emitter coupling, κ the cavity decay rate and γ the emitter decay rate.

1.1 Introduction to cavity quantum electrodynamics

Cavity quantum electrodynamics (CQED) studies the interaction of an emitter coupled to an optical resonator as illustrated in figure 1.1. When the transition of the emitter is on resonance with the cavity, the interaction is determined by following rates: the photon loss rate of the cavity κ , the nonresonant decay rate of the emitter γ and the emitter–cavity coupling rate g . In the case where $g \gg \kappa, \gamma$ a photon can be reabsorbed by the emitter before it is lost. Here, the photon emission is a reversible process and the system is in the strong coupling regime giving rise to new eigenstates. If $g \ll \kappa, \gamma$ the system is in the weak coupling regime, where the photon is lost before it can be reabsorbed. Photon emission is therefore irreversible but nevertheless affected by the cavity.

A figure of merit to characterize the emitter–cavity interaction is the cooperativity value defined as $C = 2g^2/\kappa\gamma$ which was introduced for CQED experiments with atoms [1]. Here, C corresponds to the inverse of the critical atom number, corresponding to the number of atoms required in a cavity to observe a switching of the optical response [2]. Current CQED approaches aim at maximizing C in order to achieve a pronounced strong coupling effect, which is particularly interesting in the application of quantum information science.

1.1.1 Discussion of the CQED rates

In the following we consider the dependence of g, κ and γ on the cavity and emitter properties. The zero point energy in an optical cavity (resonant to the cavity frequency

ω) originates from the randomly fluctuating vacuum electric field which scales inversely with the mode volume V_0 of the cavity [3]:

$$E_{\text{vac}} = \sqrt{\frac{\hbar\omega}{2\epsilon_0 V_0}}. \quad (1.1)$$

The interaction of the cavity with the emitter $\Delta E = \mu_{12}E_{\text{vac}}$ is given by the interaction of the emitter's dipole μ_{12} with the vacuum field. The emitter–cavity coupling rate g can then be determined by setting $\hbar g = \mu_{12}E_{\text{vac}}$:

$$g = \sqrt{\frac{\mu_{12}^2 \omega}{2\epsilon_0 \hbar V_0}}. \quad (1.2)$$

The dipole moment μ_{12} is related to the radiative lifetime τ of the emitter via:

$$\frac{1}{\tau} = \frac{\omega^3}{3\pi\epsilon_0 \hbar c^3} \mu_{12}^2. \quad (1.3)$$

Here the spontaneous radiative lifetime τ defines the decay rate of an ideal two level emitter, $\gamma = \frac{1}{\tau}$. However, we note that the actual γ can also be affected by non-radiative decay (breaking the two level approximation) or by scattering events that cause dephasing. Finally, the cavity photon loss rate is governed by the quality factor (Q -factor) defined as:

$$Q = \frac{\omega}{\kappa}, \quad (1.4)$$

i.e. Q^{-1} is the fractional loss of energy per optical period. The loss rate is limited by the finite transmission and absorption of the mirrors that build up the optical resonator. From equations 1.1–1.4 we summarize the essential properties for the construction of a high cooperativity CQED system: a high Q cavity with low mode volume combined with a narrow linewidth emitter that exhibits a strong dipole transition μ_{12} .

1.1.2 The weak coupling regime – Purcell enhancement

As mentioned above, the weak coupling corresponds to the case where $g \ll \kappa, \gamma$. If κ is the dominant loss mechanism, the emitted photon from the emitter leaks out of the cavity before it can be reabsorbed. However, the coupling to cavity modifies the spontaneous emission rate, which is known as Purcell enhancement [4]. This effect is

understood from Fermi's golden rule that describes the spontaneous emission rate W :

$$W = \frac{2\pi}{\hbar^2} M_{12}^2 p(\omega), \quad (1.5)$$

where $p(\omega)$ is the photon density of states and $M_{12} = \mu_{12} E_{\text{vac}}$ is the transition matrix element. In a cavity with resonance linewidth $\Delta\omega_c = \omega/Q = \kappa$ the density of states is described by a Lorentzian lineshape:

$$p(\omega) = \frac{2}{\pi \Delta\omega_c} \frac{\Delta\omega_c^2}{4(\omega - \omega_c)^2 + \Delta\omega_c^2} \quad (1.6)$$

that satisfies $\int_0^\infty p(\omega) d\omega = 1$. In contrast, the free space density of states within a volume V_0 is $p(\omega) = \frac{\omega^2 V_0}{\pi^2 c^3}$. We compare the spontaneous emission rate of an emitter coupled to the cavity (W^{cav}) with the uncoupled emitter rate (W^{free}) and introduce the Purcell factor F_p :

$$F_p = \frac{W^{\text{cav}}}{W^{\text{free}}} = \frac{3Q\lambda_0^3}{4\pi^2 V_0}, \quad (1.7)$$

where $\frac{c}{\omega} = \frac{\lambda_0}{2\pi}$, λ_0 being the free space wavelength. Equation 1.7 indicates that the spontaneous emission is most enhanced, when the cavity resonance overlaps with the emitter transition, i.e. when $\omega - \omega_c = 0$. We emphasize that the Purcell enhancement is maximized by optimizing Q/V_0 . Purcell factors greater than one imply that the spontaneous emission is enhanced by the cavity, where $F_p < 1$ indicates an inhibition of the emission.

1.1.3 Strong coupling

In the strong coupling regime, g is the dominant rate which results in a reversible emission of the photon. To understand the features that arise in the strong coupling regime, we introduce the Jaynes–Cummings Hamiltonian to describe the cavity–emitter system [5, 6]:

$$\mathcal{H}_{\mathcal{JC}} = \hbar\omega_c a^\dagger a + \hbar\omega_e b^\dagger b + \hbar g(a^\dagger b + b^\dagger a). \quad (1.8)$$

Here, $H_c = \hbar\omega_c a^\dagger a$ defines the cavity field, $H_e = \hbar\omega_e b^\dagger b$ the emitter and $H_I = \hbar g(b^\dagger a + a^\dagger b)$ is the interaction between cavity and emitter at rate g . $a^\dagger(a)$ and $b^\dagger(b)$ denote the creation (annihilation) operator of the photon and the emitter excitation respectively. For further analysis we assume a CQED system without dissipation, which will be introduced further below.

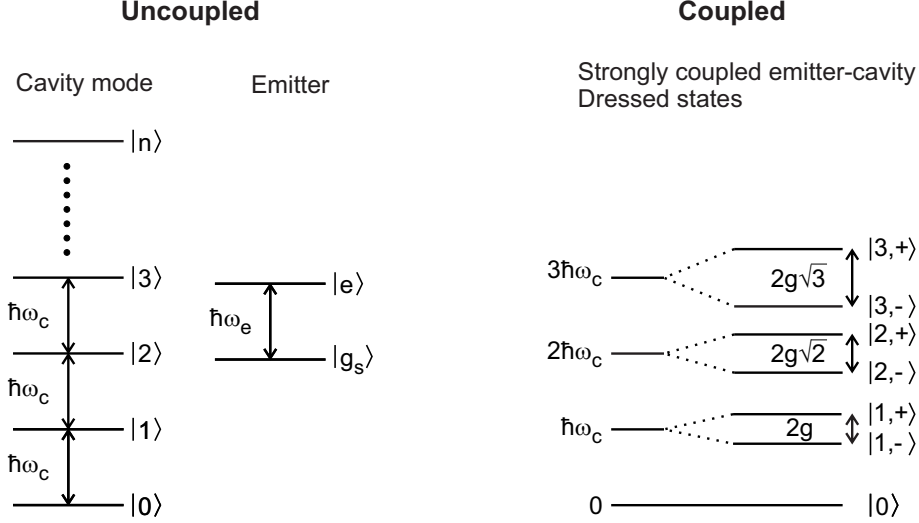


Figure 1.2. Jaynes–Cummings ladder. The ladder describes the eigenenergies when an emitter is strongly coupled to the cavity mode with coupling rate g . The energy splitting of the new eigenstates depends on the number of photons n in the cavity and is given by $2g\sqrt{n+1}$.

If the interaction is turned off (i.e $g = 0$) we can define a set of eigenstates: $|g_s, n+1\rangle$ is the state when the emitter is in its ground state, with $n+1$ photons in the cavity and $|e, n\rangle$ represents a state of the emitter being in the excited state with n photons in the cavity. If we turn on the interaction between the cavity and the emitter the total Hamiltonian in the $|e, n\rangle, |g_s, n+1\rangle$ basis is represented as:

$$\mathcal{H}_{\mathcal{JC}} = \begin{pmatrix} (n+1)\omega_c & g\sqrt{n+1} \\ g\sqrt{n+1} & n\omega_c + \omega_e \end{pmatrix}. \quad (1.9)$$

The corresponding eigenenergies of this Hamiltonian are:

$$E_{\pm} = \frac{\hbar\omega_e}{2} + \hbar\omega_c \left(n + \frac{1}{2} \right) \pm \sqrt{\hbar^2 g^2 (n+1) + \left(\frac{\hbar\delta}{2} \right)^2}, \quad (1.10)$$

where $\delta = \omega_c - \omega_e$ is the cavity–emitter detuning. At zero detuning $\delta = 0$,

$$E_{\pm} = \frac{\hbar\omega_e}{2} + \hbar\omega_c \left(n + \frac{1}{2} \right) \pm \hbar g \sqrt{n+1} \quad (1.11)$$

with the corresponding normalized eigenstates:

$$|n, +\rangle = \frac{|e, n\rangle + |g_s, n+1\rangle}{\sqrt{2}}, \quad (1.12a)$$

$$|n, -\rangle = \frac{|e, n\rangle - |g_s, n+1\rangle}{\sqrt{2}}. \quad (1.12b)$$

The $|n, +\rangle$ and $|n, -\rangle$ are the dressed states, namely the upper ($|n, +\rangle$) and lower ($|n, -\rangle$) polariton that arise in the strong coupling regime and are admixtures of the bare cavity–emitter states, $|g_s, n+1\rangle$ and $|e, n\rangle$. An important consequence of equation 1.11 is illustrated in the Jaynes–Cummings ladder (figure 1.2). The strong coupling results in a splitting between $|n, +\rangle$ and $|n, -\rangle$ which increases with the photon number n in the system, thereby inducing a nonlinearity in CQED. The splitting for $n = 0$ is $E_{\text{vac}} = 2\hbar g$ and is commonly denoted as the vacuum Rabi energy splitting.

As mentioned above the dissipation rates have been neglected so far. To include the CQED loss rates in expression 1.10 we introduce *ad hoc* the complex cavity and emitter frequencies: $\omega_c \rightarrow \omega_c + i\frac{\kappa}{2}$ and $\omega_e \rightarrow \omega_e + i\frac{\gamma}{2}$. From equation 1.10 we then arrive at the complex eigenfrequencies (for $n = 0$):

$$\omega_{\pm} = \frac{\omega_c + \omega_e}{2} + i\frac{\kappa + \gamma}{4} \pm \sqrt{g^2 + \left(\frac{\delta}{2} + i\frac{\kappa - \gamma}{4}\right)^2}. \quad (1.13)$$

We note that the same expression is obtained when solving the optical Bloch equations that are obtained by the Lindblad operator description (see chapter A). The decay rates of the dressed states are now described by twice the imaginary part of the eigenfrequencies, which yields $\frac{\kappa + \gamma}{2}$ at zero detuning. Furthermore, the condition to achieve strong coupling can now be extracted from equation 1.13: for $\delta = 0$, the expression under the square root must be positive in order to obtain a normal mode splitting, which applies only for $4g \geq |\kappa - \gamma|$.

1.1.4 Collective interaction

We next consider N emitters at a fixed position in the cavity that all couple to the single mode of the cavity for the case of $n = 0$. The overall ground state of the ensemble is defined when all emitters are in the ground state: $|\Psi_0\rangle = |g_s \dots g_s\rangle$. If the system is

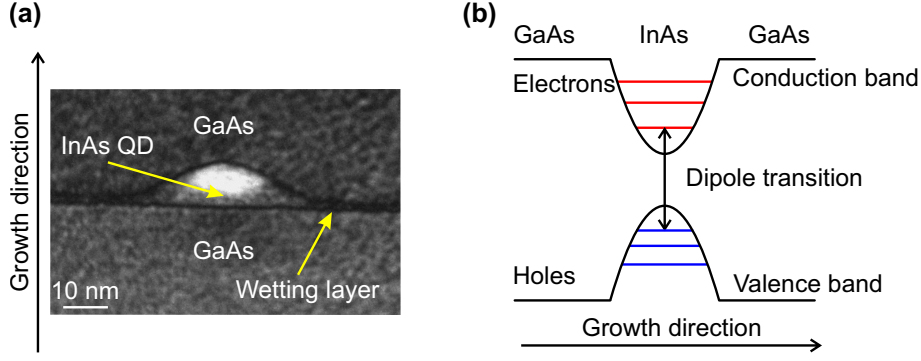


Figure 1.3. (a) TEM image of an InAs QD embedded in a GaAs semiconductor structure (courtesy of Jean-Michel Chauveau and Arne Ludwig). (b) Schematic level structure of an InAs QD embedded in GaAs. Due to the bandgap difference of InAs compared to GaAs a nanoscale confinement in three dimensions is obtained, resulting in the formation of discrete energy levels.

weakly excited the first collective excited state is given by [7]:

$$|\Psi_1\rangle = \frac{1}{\sqrt{N}} (|e, g_s \dots g_s\rangle + |g_s, e \dots g_s\rangle + \dots + |g \dots g, e\rangle). \quad (1.14)$$

If the cavity-emitter coupling g is similar for each emitter the interaction Hamiltonian becomes

$$H_I = \hbar g \sum_i^N (a^\dagger b_i + b_i^\dagger a) \quad (1.15)$$

The collective coupling strength g_N is then determined by the off diagonal matrix elements of the Jaynes-Cummings Hamiltonian within the basis $|\Psi_0, 1\rangle, |\Psi_1, 0\rangle$:

$$g_N = \langle \Psi_1, 0 | H_I | \Psi_0, 1 \rangle = \sqrt{N}g. \quad (1.16)$$

As an essential result of equation 1.16 we note that the interaction of an ensemble of N emitters with a single cavity mode of the radiation field is enhanced by the factor \sqrt{N} , which manifests itself by an increased vacuum Rabi energy splitting. This effect is known as the Dicke effect [7].

1.2 Quantum Dots for CQED

The strong coupling regime was first reached with atoms [8] and enabled various pioneering experiments that allowed for fundamental studies of CQED [9]. However, trapping single atoms remains technologically elaborate and therefore minimizes the prospects

for scaling the CQED technologies. A promising route is to replace the atoms with self assembled semiconductor quantum dots (QD) that mimic two level emitters. QDs are based on indium arsenide (InAs) grown on gallium arsenide (GaAs) by molecular beam epitaxy (MBE) [10]. Due to the lattice mismatch of InAs compared to GaAs, QDs are formed after 1.5 monolayers of InAs [11]. The QDs, accompanied by an InAs wetting layer, are then capped with GaAs and thereby embedded in a semiconductor heterostructure as shown in the transmission electron microscopy (TEM) image in figure 1.3a. The QDs have a typical diameter of 20 nm and a height of approximately 5 nm, where the exact shape depends on the growth details. Figure 1.3b shows the discrete conduction and valence levels that arise within the QD due to the nanoscale confinement in three dimensions. Typically, the conduction levels are separated by $\sim 20 - 50$ meV and the valence levels by $\sim 10 - 25$ meV [12]. The optical transition in the quantum dot is associated with the excitation/recombination of an electron hole pair. The optically excited state consisting of one electron and one hole is referred to as a neutral exciton. By incorporating the InGaAs QDs into a field effect structure, the QD can be selectively charged by a single electron or hole such that a negatively or positively charged exciton can be formed [13]. Considering the corresponding spin of the additional charge carrier has enabled a great variety of quantum dot spin-physics experiments [12]. The transition wavelength of the QD can be engineered to lie around the experimentally convenient wavelength of ~ 950 nm by thermal annealing during [14] and after [15] the growth process. The radiative lifetime of InGaAs QDs was shown to be as short as ~ 0.8 ns [16] corresponding to a relatively large electric dipole of 0.6 nm/e, where e is the electronic charge [17]. Moreover, the photons emitted by these dots exhibit narrow linewidths approaching the transform limit [18].

The fact that the QDs are embedded at a fixed location in the semiconductor greatly simplifies trapping them in an optical microcavity as compared to experiments with atoms. Furthermore, the relatively large dipole moment that is associated with the InGaAs QDs, makes them a suitable candidate as the interaction of the cavity field and the QD is expected to be strong. Several types of semiconductor microcavities for coupling QDs have been implemented, in each case monolithically fabricated around the QDs [19–21]. An interesting approach are QDs embedded in semiconductor microdisks, where the light is confined in a whispering gallery mode [22, 23]. The Q -factor of these devices is potentially high but comes at the cost of a large mode volume. The more prominent examples however are micropillars and photonic crystal nanocavities, discussed briefly in the following.

1.2.1 Micropillars

Micropillar cavities are typically established following MBE growth of alternating layers of GaAs and AlGaAs. The layers have a thickness of $\lambda/4n_{\text{GaAs}}$ and $\lambda/4n_{\text{AlGaAs}}$ respectively, where n_{GaAs} (n_{AlGaAs}) is the refractive index of GaAs (AlGaAs) and thus build a distributed Bragg reflector (DBR). In between the two DBRs a λ thick GaAs layer is included, with the optically active InGaAs at the centre, i.e at the antinode of the fundamental cavity mode [24]. The micropillars are then subsequently etched with a diameter of typically a few micrometers to reach a low mode volume. Q-factors of up to 65,000 [25] and mode volumes as small as $2.3 (\lambda/n)^3$ [26] have been demonstrated with micropillars. However, there are several disadvantages for the application in CQED. It has been shown that the Q-factor is limited by scattering from the sidewalls, which becomes more pronounced for small pillar diameters [27]. Ultimately, this sets a constraint for reducing the micropillar mode volume. Furthermore, the QDs form at a random position during MBE growth, there is only a statistical chance that they are optimally located at the micropillar centre after etching. Spectral tuning can be achieved by varying the temperature [28] or electro-optical tuning of the exciton via the Stark effect [29]. Temperature tuning is only optimal for small tuning ranges since the exciton linewidth is homogeneously broadened by an increased temperature [30]. Electro-optical tuning circumvents this but involves a complex fabrication procedure. Furthermore, the tuning range is only in the range of a few micro-electronvolts since the exciton charge state can switch unintentionally upon application of a high bias voltage. An attempt to address these drawbacks is a very complex fabrication procedure, where the QD is selected *in situ* prior to the etching of the micropillars [31].

1.2.2 Photonic crystals

In photonic crystals the dielectric properties are periodically modulated on the length-scale of the wavelength of the light. The light then undergoes Bragg scattering, which induces a photonic band gap, in which the light is unable to propagate. For CQED experiments, InGaAs QDs are incorporated in GaAs photonic crystals. The periodic modulation of the refractive index is achieved by etching a series of holes in the structure. By leaving out three holes in the periodic structure [32], a localized cavity mode with a frequency in the photonic band gap is created. The mode volume of these so called L3 nanocavities is less than $\sim (\lambda/n)^3$. The Q-factors were shown to be increased by displacing the holes at the end of the cavity [33]. Hence Q-factors of 2.5×10^4 are regu-

larly achieved for L3 nanocavities containing single QDs [34, 35]. Similar to micropillars the spatial *in situ* positioning of the QDs within the photonic crystal cavity remains impossible. Therefore, techniques have been established where the QDs are first located by scanning electron microscopy (SEM) [36] or atomic force microscopy (AFM) [34] before the nanocavity is fabricated around the dot. Tunability can be achieved electro-optically [37] or by temperature [38] with the same drawbacks as in micropillars. In addition, a digital wet etching technique [39] or the deposition of nitrogen gas [40] was established for tuning the cavity. However, these two methods are irreversible and therefore unsuitable for CQED applications.

1.3 Observations and applications of CQED

The successful coupling of QDs and atoms to optical resonators entails a large variety of possible applications both in the weak and strong coupling regimes.

Strong coupling with single atoms coupled to high Q Fabry–Pérot cavities has been observed for example with rubidium atoms [41] and with cesium atoms [42]. The strong coupling regime offers a possibility to manipulate the atom–cavity entanglement [43] and hence build a resource for the processing and distribution of quantum information [44]. Experiments in this context include the reversible transfer of quantum states [45] and photon–photon entanglement [46]. Furthermore, the strong coupling regime has the potential for deterministic atom–atom entanglement [47]. The collective interaction of many atoms with a single cavity mode was shown to exhibit the predicted \sqrt{N} [48, 49] dependence, with possible application as a quantum memory [50].

An interesting aspect of the strong coupling regime is the nonlinearity induced by the Jaynes–Cummings ladder as shown in figure 1.2. This is the basis for the so-called photon blockade effect [51]. When an excitation laser is resonant with the $|0\rangle \leftrightarrow |1, -\rangle$ transition, the second manifold $|2, -\rangle$ cannot be accessed since the excitation laser is not resonant with the $|1, -\rangle \leftrightarrow |2, -\rangle$ transition. The photon blockade regime represents a strong photon–photon interaction and enables the realization of a single photon transistor [52].

In the solid state, strong coupling of quantum wells in micropillar structures was first observed in 1992 [53] and allowed for the formation of Bose–Einstein–condensates (BECs) in some ways analogous to BECs of ultracold atoms [54, 55]. Coupling of single QDs is desirable, since electron spins interacting via a common high Q –cavity mode are a promising component for quantum information processing [56]. Strong coupling

of single self-assembled InGaAs QDs has been observed in micropillars [28], photonic crystal nanocavities [34, 57, 58] and microdisks [23]. This facilitated an investigation of the Jaynes–Cummings ladder [59] with the observation of photon blockade [35, 60], subsequently leading to the implementation of a two colour single photon switch [61]. In addition to the optical experiments, dressed states in the Gigahertz domain could be achieved by coupling a Cooper pair box to a superconducting microwave cavity [62].

The Purcell enhancement in the solid state has been experimentally observed for an ensemble of QDs coupled to micropillars [63]. The coupling of single quantum dots [64] was also demonstrated in photonic crystals [65] and recently in tunable Fabry–Pérot like microcavities [66, 67]. Generally, the weak coupling regime enhances greatly the quantum efficiency of a single photon source [68], important in the creation of indistinguishable single photons [69] for optical quantum communication [70]. In addition a Raman spin-flip transition induced by a cavity [71] can be used as a source for indistinguishable single photons [72]. Beyond the possible applications for quantum information science, the enhancement of spontaneous emission enables the realization of low-threshold lasers based on a few quantum dots [73].

1.4 Coupling quantum dots to a tunable Fabry–Pérot microcavity

Generally all CQED applications profit from a high cooperativity value, since only in the high- C regime effects such as the photon blockade become pronounced. This thesis aims at the realization of a high C CQED system using QDs coupled to a tunable plane-concave Fabry–Pérot microcavity with low mode volume [66]. Here, our microcavity exhibits the possibility of large range spectral tuning and spatial positioning of the QD within the cavity mode. In this approach the advantageous emission properties of the QD (narrow linewidth and short radiative recombination time) are combined with external high reflectivity mirrors in order to achieve a high cooperativity of the system.

1.4.1 A plane-concave tunable Fabry–Pérot microcavities

We summarize the main properties of a tunable plane-concave Fabry–Pérot microcavity. Figure 1.4a shows a plane concave cavity with an effective length L and a radius of curvature of the top mirror of \mathcal{R} . From a transfer matrix analysis, a stability criterion for the plane-concave cavity can be formulated which sets the constraint for a stable

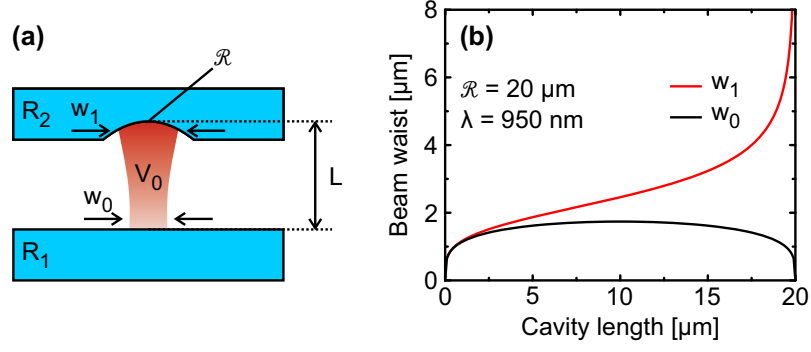


Figure 1.4. (a) Schematic view of a plane–concave microcavity with radius of curvature \mathcal{R} and length L which defines beam waists w_0 and w_1 and hence the volume V_0 of the cavity mode. (b) Beam waist at the planar mirror w_0 and beam waist at the curved mirror w_1 as a function of cavity length L . For small L , $w_0 \approx w_1$, so that a cylindrical mode can be assumed.

mode [74]:

$$0 \leq g \leq 1. \quad (1.17)$$

Here $g = 1 - \frac{L}{\mathcal{R}}$ is a dimensionless confocal parameter that accounts for the cavity geometry. In a plane–concave Fabry–Pérot cavity the stability criterion effectively becomes $L \leq \mathcal{R}$.

The geometry of the plane–concave cavity defines the Gaussian mode which is stable in the resonator and hence also the beam waist at the plane mirror w_0 and at the curved mirror w_1 are according to Gaussian optics [75]:

$$w_1 = \sqrt{\frac{\lambda_0 \mathcal{R}}{\pi}} \left(\frac{\mathcal{R}}{L} - 1 \right)^{-\frac{1}{4}}, \quad (1.18a)$$

$$w_0 = \sqrt{\frac{\lambda_0}{\pi}} (L\mathcal{R} - L^2)^{\frac{1}{4}}. \quad (1.18b)$$

Figure 1.4b shows the length dependence of the beam waist w_0 and w_1 for a cavity with $\mathcal{R} = 20 \mu\text{m}$ and $\lambda_0 = 950 \text{ nm}$. We notice that for small cavity length $w_0 \approx w_1$, from which the cavity mode volume can be estimated according to:

$$V_0 = \frac{\pi w_0^2}{2} L. \quad (1.19)$$

The stability criterion in equation 1.17 sets the geometric constraint for a stable Gaussian mode in the cavity. For a fixed geometry the eigenfrequencies of the cavity modes ν_{nmq} are evaluated under the constraint that the phase round trip is equal to an

integer multiple of 2π , in which case the field constructively interferes with itself:

$$\nu_{nmq} = \left(q + (n + m + 1) \frac{\cos^{-1} \pm \sqrt{g_1 g_2}}{\pi} \right) \frac{c}{2L}. \quad (1.20)$$

Here, n and m are the transverse Gaussian mode indices, while q is the longitudinal mode index. The term $\frac{c}{2L}$ represents the free spectral range (FSR) of the cavity, i.e the longitudinal mode splitting. A measure of the performance of a cavity is the finesse, which relates the FSR to the resonance linewidth $\Delta\nu$ of the cavity and is linked to the Q -factor:

$$F = \frac{FSR}{\Delta\nu} = \frac{\lambda_0 Q}{L} \quad (1.21)$$

where the frequency resolution definition of $Q = \frac{\nu}{\Delta\nu} = \frac{\omega}{\kappa}$ is used and $c = \lambda_0 \nu$. The finesse is determined essentially by the reflectivity of the two mirrors R_1 and R_2 :

$$F = \frac{\pi (R_1 R_2)^{(1/4)}}{1 - \sqrt{R_1 R_2}} \quad (1.22)$$

High reflectivity mirrors for CQED typically consist of alternating quarter wave dielectric layers (e.g. $\text{Ta}_2\text{O}_5/\text{SiO}_2$) that form a DBR. The reflectivity of the DBRs is given by the number of pairs used. A high refractive index contrast is desired for two reasons: the frequency range, where the light is reflected is larger and the penetration is reduced, important for short cavity length [76]. The DBR films are commonly produced by ion beam sputtering, which allowed for the demonstration of cavity finesse up to 10^6 [77]. In addition, DBRs can also be epitaxially grown using for example pairs of GaAs/AlGaAs which have a similar lattice constant but a different refractive index. These DBRs are nowadays widely used for vertical-cavity surface-emitting lasers (VCSELs) [78]. Furthermore, GaAs/AlGaAs alternating layers can be conveniently combined with InGaAs QD as shown for instance in micropillar CQED.

We motivate the use of a miniaturized plane-concave Fabry–Pérot microcavity for CQED applications. Here, the two mirrors can be individually prepared and then combined which enhances greatly the flexibility compared to monolithic cavities. We note that not only QDs but also nitrogen-vacancy centres in diamond [79] or quantum wells [80] can be incorporated in such a microcavity. The mode volume is reduced by choosing a small radius of curvature for the concave top mirror as indicated by equation 6.5. Spectral tunability and spatial positioning of the emitter within the cavity mode can be conveniently achieved by moving the two mirrors with respect to each other. The advantages associated with a tunable microcavity combined with the bene-

ficial properties of InGaAs QDs emphasize the potential for realizing high cooperativity CQED in the solid state.

References

- [1] H. J. Kimble, [Physica Scripta](#) **1998**, 127 (1998).
- [2] Q. A. Turchette, C. J. Hood, W. Lange, H. Mabuchi, and H. J. Kimble, [Physical Review Letters](#) **75**, 4710 (1995).
- [3] M. Fox, *Quantum Optics: An Introduction*, Vol. 6 (Oxford University Press, 2006).
- [4] E. Purcell, [Physical Review](#) **69**, 681 (1946).
- [5] E. Jaynes and F. Cummings, [Proceedings of the IEEE](#) **51**, 89 (1963).
- [6] E. del Valle, F. P. Laussy, and C. Tejedor, [Physical Review B](#) **79**, 235326 (2009).
- [7] R. H. Dicke, [Physical Review](#) **93**, 99 (1954).
- [8] R. J. Thompson, G. Rempe, and H. J. Kimble, [Physical Review Letters](#) **68**, 1132 (1992).
- [9] H. Mabuchi and A. C. Doherty, [Science](#) **298**, 1372 (2002).
- [10] R. J. Warburton, [Contemporary Physics](#) **43**, 351 (2002).
- [11] D. Leonard, K. Pond, and P. M. Petroff, [Physical Review B](#) **50**, 11687 (1994).
- [12] R. J. Warburton, [Nature Materials](#) **12**, 483 (2013).
- [13] R. J. Warburton, C. Schaflein, D. Haft, F. Bickel, A. Lorke, K. Karrai, J. M. Garcia, W. Schoenfeld, and P. M. Petroff, [Nature](#) **405**, 926 (2000).
- [14] J. Garcia, T. Mankad, P. Holtz, P. Wellman, and P. M. Petroff, [Applied Physics Letters](#) **72**, 3172 (1998).
- [15] W. Langbein, P. Borri, U. Woggon, V. Stavarache, D. Reuter, and A. D. Wieck, [Physical Review B](#) **69**, 161301 (2004).
- [16] P. A. Dalgarno, J. M. Smith, J. McFarlane, B. D. Gerardot, K. Karrai, A. Badolato, P. M. Petroff, and R. J. Warburton, [Physical Review B](#) **77**, 245311 (2008).
- [17] K. Karrai and R. J. Warburton, [Superlattices and Microstructures](#) **33**, 311 (2003).
- [18] A. V. Kuhlmann, J. H. Prechtel, J. Houel, A. Ludwig, D. Reuter, A. D. Wieck, and R. J. Warburton, [arXiv:1307.7109](#) (2013).

- [19] G. Khitrova, H. M. Gibbs, M. Kira, S. W. Koch, and A. Scherer, [Nature Physics](#) **2**, 81 (2006).
- [20] P. Lodahl, S. Mahmoodian, and S. Stobbe, [Reviews of Modern Physics](#) **87**, 347 (2015).
- [21] K. J. Vahala, [Nature](#) **424**, 839 (2003).
- [22] A. Kiraz, P. Michler, C. Becher, B. Gayral, A. Imamoglu, L. Zhang, E. Hu, W. Schoenfeld, and P. Petroff, [Applied Physics Letters](#) **78**, 3932 (2001).
- [23] K. Srinivasan and O. Painter, [Nature](#) **450**, 862 (2007).
- [24] S. Reitzenstein and A. Forchel, [Journal of Physics D: Applied Physics](#) **43**, 033001 (2010).
- [25] V. Loo, L. Lanco, A. Lemaître, I. Sagnes, O. Krebs, P. Voisin, and P. Senellart, [Applied Physics Letters](#) **97**, 241110 (2010).
- [26] M. Lerner, N. Gregersen, F. Dunzer, S. Reitzenstein, S. Höfling, J. Mørk, L. Worschech, M. Kamp, and A. Forchel, [Physical Review Letters](#) **108**, 057402 (2012).
- [27] T. Rivera, J.-P. Debray, J. M. Gérard, B. Legrand, L. Manin-Ferlazzo, and J. L. Oudar, [Applied Physics Letters](#) **74**, 911 (1999).
- [28] J. Reithmaier, G. Sek, A. Löffler, C. Hofmann, S. Kuhn, S. Reitzenstein, L. Keldysh, V. Kulakovskii, T. Reinecke, and A. Forchel, [Nature](#) **432**, 197 (2004).
- [29] C. Kistner, T. Heindel, C. Schneider, A. Rahimi-Iman, S. Reitzenstein, S. Höfling, and A. Forchel, [Optics Express](#) **16**, 15006 (2008).
- [30] B. Urbaszek, E. J. McGhee, M. Krüger, R. J. Warburton, K. Karrai, T. Amand, B. D. Gerardot, P. M. Petroff, and J. M. Garcia, [Physical Review B](#) **69**, 035304 (2004).
- [31] A. Dousse, L. Lanco, J. Suffczyński, E. Semenova, A. Miard, A. Lemaître, I. Sagnes, C. Roblin, J. Bloch, and P. Senellart, [Physical Review Letters](#) **101**, 267404 (2008).
- [32] D. Englund, I. Fushman, and J. Vučković, [Optics Express](#) **13**, 5961 (2005).
- [33] Y. Akahane, T. Asano, B.-S. Song, and S. Noda, [Nature](#) **425**, 944 (2003).

-
- [34] K. Hennessy, A. Badolato, M. Winger, D. Gerace, M. Atatüre, S. Gulde, S. Fält, E. L. Hu, and A. Imamoglu, [Nature](#) **445**, 896 (2007).
 - [35] A. Faraon, I. Fushman, D. Englund, N. Stoltz, P. Petroff, and J. Vučković, [Nature Physics](#) **4**, 859 (2008).
 - [36] A. Badolato, K. Hennessy, M. Atatüre, J. Dreiser, E. Hu, P. M. Petroff, and A. Imamoglu, [Science](#) **308**, 1158 (2005).
 - [37] A. Laucht, F. Hofbauer, N. Hauke, J. Angele, S. Stobbe, M. Kaniber, G. Böhm, P. Lodahl, M. Amann, and J. Finley, [New Journal of Physics](#) **11**, 023034 (2009).
 - [38] D. Englund, A. Majumdar, M. Bajcsy, A. Faraon, P. Petroff, and J. Vučković, [Physical Review Letters](#) **108**, 093604 (2012).
 - [39] K. Hennessy, A. Badolato, A. Tamboli, P. Petroff, E. Hu, M. Atatüre, J. Dreiser, and A. Imamoglu, [Applied Physics Letters](#) **87**, 021108 (2005).
 - [40] M. Kaniber, A. Laucht, A. Neumann, J. M. Villas-Bôas, M. Bichler, M.-C. Amann, and J. J. Finley, [Physical Review B](#) **77**, 161303 (2008).
 - [41] P. Maunz, T. Puppe, I. Schuster, N. Syassen, P. W. H. Pinkse, and G. Rempe, [Physical Review Letters](#) **94**, 033002 (2005).
 - [42] A. Boca, R. Miller, K. M. Birnbaum, A. D. Boozer, J. McKeever, and H. J. Kimble, [Physical Review Letters](#) **93**, 233603 (2004).
 - [43] J. M. Raimond, M. Brune, and S. Haroche, [Reviews of Modern Physics](#) **73**, 565 (2001).
 - [44] H. J. Kimble, [Nature](#) **453**, 1023 (2008).
 - [45] A. D. Boozer, A. Boca, R. Miller, T. E. Northup, and H. J. Kimble, [Physical Review Letters](#) **98**, 193601 (2007).
 - [46] T. Wilk, S. C. Webster, A. Kuhn, and G. Rempe, [Science](#) **317**, 488 (2007).
 - [47] M. B. Plenio, S. F. Huelga, A. Beige, and P. L. Knight, [Physical Review A](#) **59**, 2468 (1999).
 - [48] Y. Colombe, T. Steinmetz, G. Dubois, F. Linke, D. Hunger, and J. Reichel, [Nature](#) **450**, 272 (2007).

- [49] F. Brennecke, T. Donner, S. Ritter, T. Bourdel, M. Köhl, and T. Esslinger, [Nature](#) **450**, 268 (2007).
- [50] L.-M. Duan, M. D. Lukin, J. I. Cirac, and P. Zoller, [Nature](#) **414**, 413 (2001).
- [51] K. M. Birnbaum, A. Boca, R. Miller, A. D. Boozer, T. E. Northup, and H. J. Kimble, [Nature](#) **436**, 87 (2005).
- [52] D. E. Chang, A. S. Sorensen, E. A. Demler, and M. D. Lukin, [Nature Physics](#) **3**, 807 (2007).
- [53] T. B. Norris, J.-K. Rhee, C.-Y. Sung, Y. Arakawa, M. Nishioka, and C. Weisbuch, [Physical Review B](#) **50**, 14663 (1994).
- [54] J. Kasprzak, M. Richard, S. Kundermann, A. Baas, P. Jeambrun, J. M. J. Keeling, F. M. Marchetti, M. H. Szymanska, R. Andre, J. L. Staehli, V. Savona, P. B. Littlewood, B. Deveaud, and L. S. Dang, [Nature](#) **443**, 409 (2006).
- [55] R. Balili, V. Hartwell, D. Snoke, L. Pfeiffer, and K. West, [Science](#) **316**, 1007 (2007).
- [56] A. Imamoglu, D. D. Awschalom, G. Burkard, D. P. DiVincenzo, D. Loss, M. Sherwin, and A. Small, [Physical Review Letters](#) **83**, 4204 (1999).
- [57] T. Yoshie, A. Scherer, J. Hendrickson, G. Khitrova, H. M. Gibbs, G. Rupper, C. Ell, O. B. Shchekin, and D. G. Deppe, [Nature](#) **432**, 200 (2004).
- [58] D. Englund, A. Faraon, I. Fushman, N. Stoltz, P. Petroff, and J. Vučković, [Nature](#) **450**, 857 (2007).
- [59] J. Kasprzak, S. Reitzenstein, E. A. Muljarov, C. Kistner, C. Schneider, M. Strauss, S. Hofling, A. Forchel, and W. Langbein, [Nature Materials](#) **9**, 304 (2010).
- [60] A. Reinhard, T. Volz, M. Winger, A. Badolato, K. J. Hennessy, E. L. Hu, and A. Imamoglu, [Nature Photonics](#) **6**, 93 (2012).
- [61] T. Volz, A. Reinhard, M. Winger, A. Badolato, K. J. Hennessy, E. L. Hu, and A. Imamoglu, [Nature Photonics](#) **6**, 605 (2012).
- [62] A. Wallraff, D. I. Schuster, A. Blais, L. Frunzio, R.-S. Huang, J. Majer, S. Kumar, S. M. Girvin, and R. J. Schoelkopf, [Nature](#) **431**, 162 (2004).

-
- [63] J. Gérard, B. Sermage, B. Gayral, B. Legrand, E. Costard, and V. Thierry-Mieg, *Physica Review Letters* **81**, 1110 (1998).
- [64] M. Bayer, T. L. Reinecke, F. Weidner, A. Larionov, A. McDonald, and A. Forchel, *Physical Review Letters* **86**, 3168 (2001).
- [65] P. Lodahl, A. Floris van Driel, I. S. Nikolaev, A. Irman, K. Overgaag, D. Vanmaekelbergh, and W. L. Vos, *Nature* **430**, 654 (2004).
- [66] R. J. Barbour, P. A. Dalgarno, A. Curran, K. M. Nowak, H. J. Baker, D. R. Hall, N. G. Stoltz, P. M. Petroff, and R. J. Warburton, *Journal of Applied Physics* **110**, 053107 (2011).
- [67] A. Muller, E. B. Flagg, M. Metcalfe, J. Lawall, and G. S. Solomon, *Applied Physics Letters* **95**, 173101 (2009).
- [68] S. Strauf, N. G. Stoltz, M. T. Rakher, L. A. Coldren, P. M. Petroff, and D. Bouwmeester, *Nature Photonics* **1**, 704 (2007).
- [69] C. Santori, D. Fattal, J. Vuckovic, G. S. Solomon, and Y. Yamamoto, *Nature* **419**, 594 (2002).
- [70] A. J. Shields, *Nature Photonics* **1**, 215 (2007).
- [71] A. Kiraz, M. Atatüre, and A. Imamoglu, *Physical Review A* **69**, 032305 (2004).
- [72] T. M. Sweeney, S. G. Carter, A. S. Bracker, M. Kim, C. S. Kim, L. Yang, P. M. Vora, P. G. Brereton, E. R. Cleveland, and D. Gammon, *Nature Photonics* **8**, 442 (2014).
- [73] S. Strauf, K. Hennessy, M. T. Rakher, Y.-S. Choi, A. Badolato, L. C. Andreani, E. L. Hu, P. M. Petroff, and D. Bouwmeester, *Physical Review Letters* **96**, 127404 (2006).
- [74] A. Yariv and P. Yeh, *Photonics: Optical Electronics in Modern Communications* (Oxford University Press, 2006).
- [75] W. Nagourney, *Quantum Electronics for Atomic Physics* (Oxford University Press, 2010).
- [76] D. I. Babic and S. Corzine, *Quantum Electronics, IEEE Journal of* **28**, 514 (1992).

- [77] G. Rempe, R. Lalezari, R. J. Thompson, and H. J. Kimble, [Optics Letters](#) **17**, 363 (1992).
- [78] C. W. Wilmsen, H. Temkin, and L. A. Coldren, *Vertical-Cavity Surface-Emitting Lasers*, Vol. 1 (1999).
- [79] R. Albrecht, A. Bommer, C. Deutsch, J. Reichel, and C. Becher, [Physical Review Letters](#) **110**, 243602 (2013).
- [80] S. Dufferwiel, F. Fras, A. Trichet, P. M. Walker, F. Li, L. Giriunas, M. N. Makhonin, L. R. Wilson, J. M. Smith, E. Clarke, M. S. Skolnick, and D. N. Krizhanovskii, [Applied Physics Letters](#) **104**, 192107 (2014).

Chapter 2

CO₂ Laser ablation of miniaturized concave Fabry–Pérot mirrors

This chapter describes the development of miniaturized concave mirrors before they are coated with a distributed Bragg reflector consisting either of alternating layers of Ta₂O₅/SiO₂ or TiO₂/SiO₂. The concave structures are fabricated by laser ablation of fused silica using a CO₂ laser with wavelength of 10.6 μm . The laser radiation is efficiently absorbed and locally melts the silica, resulting in an imprint of the CO₂ laser's intensity profile. Owing to the surface tension of the molten silica, the surface roughness of the ablated spots is smoothened. The fabrication geometries are determined by adjusting the fabrication power and pulse width with an acousto optical modulator (AOM). It is possible to fabricate a large range of radii of curvature from below 10 μm to up to 1 mm. Atomic force microscopy measurements reveal a surface roughness in the ablated crater of 0.2 nm.

2.1 Introduction

Our approach to developing a small mode volume Fabry–Pérot–like microcavity consists of fabricating a concave top mirror with a small radius of curvature. A candidate for the fabrication of such a top mirror is CO₂ laser–ablation of fused silica. The CO₂ laser wavelength of 10.6 μm is efficiently absorbed by the silica resulting in a local melting of the irradiated silica. Due to the surface tension in the molten silica layer, the surface roughness of the irradiated area is smoothened, a key advantage of this technique. This was shown to be an effective technique to polish silica substrates [1, 2] and local repair of damaged silica optics [3]. Furthermore, CO₂ laser machining allowed for the fabrication of convex microlenses [4], microtoroidal resonators [5] and microlenses on one end of single–mode optical fibers [6].

Here, we present the fabrication of concave silica structures by means of CO₂ laser ablation. These concave structures are later coated with a distributed Bragg reflector (DBR) and build one end mirror of our miniaturized Fabry–Pérot–like cavity design. By adjusting the laser power and exposure time incident on the fused silica substrate, we were able to produce a wide range of craters with radii of curvature from 1 mm down to less than 10 μm . An additional smoothing pulse flattens out possible silica residuals in the crater that may emerge during the ablation process. Atomic force microscopy (AFM) measurements reveal root mean square roughnesses (rms) down to 0.2 nm in the crater. Throughout the ablation process we use moderate power, since high power was shown to eject silica during the process and contaminates the vicinity of the crater as also shown in [7].

2.2 The CO₂ laser

2.2.1 Setup

The setup accompanying with the CO₂ laser (Synrad Inc., Firestar v30) is shown in figure 2.1. We use an acousto optical modulator (AOM) (Brimrose Corporation, GEM–40–1–10.6) to control the power and exposure time incident on the silica substrate: where the first order of the deflection is guided towards the silica sample. The zeroth order is collected by a thermopile detector (Thorlabs Inc., S314C) with a slow risetime (≈ 1 s) and a high damage threshold (2kW/cm²) to monitor the long term stability of the CO₂ laser power. A combination of a linear polarizer (Thorlabs Inc., PHB–7) and a $\lambda/4$ waveplate (II–VI infrared, WPM–10.6–.35–90–U) minimizes back reflection

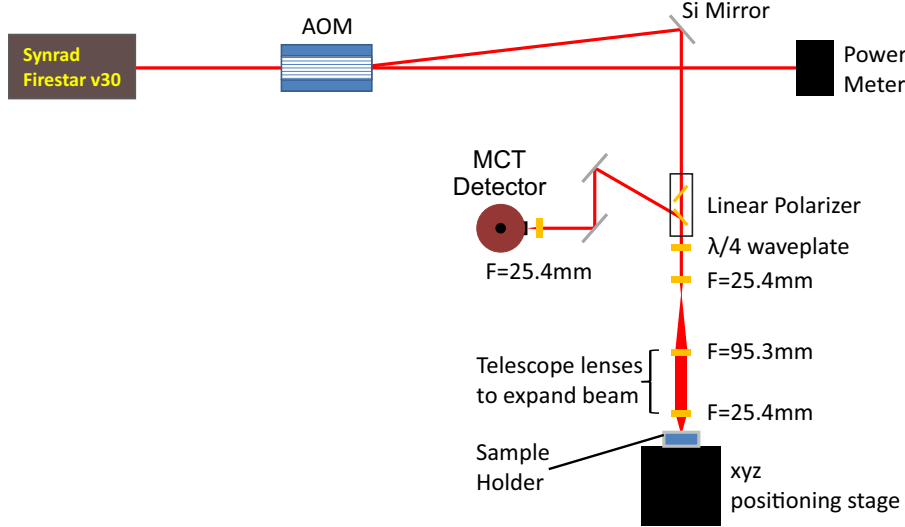


Figure 2.1. CO₂-laser setup for the fabrication of low radii of curvature Fabry-Pérot top mirrors for the tunable microcavity. The CO₂ laser is typically operated at a PWM of 8% at a repetition rate of 20 kHz. We adjust the length and power of the fabrication pulse with an acousto optical modulator (AOM), that deflects the first order onto the silica substrate. A combination of a linear polarizer and a $\lambda/4$ waveplate minimized back reflection into the laser. Focussing and positioning of the sample is achieved by analyzing the reflected power with a fast MCT photodiode.

into the laser. The linear polarizer consists of two ZnSe-plates incorporated at the Brewster angle such that horizontal polarized radiation is transmitted, while vertically polarized light is reflected. The incident laser output is initially horizontally polarized and a quarter waveplate translates the polarization to σ^- , which upon reflection is converted into σ^+ and translated by the $\lambda/4$ waveplate into horizontally polarized light. The Brewster plates in the polarizer then reflect the vertically polarized light, which is then collected by a nitrogen cooled mercury-cadmium-telluride (MCT or HgCdTe) photodetector with a risetime of 150 ns (Hamamatsu Photonics K.K., P9697-01). Two aspheric ZnSe lenses (ULO Optics Ltd.) incorporated after the $\lambda/4$ waveplate with focal length of 25.4 and 95.3 mm act as telescope lenses to expand the beam diameter such that the laser beam is efficiently focused by the focusing lens ($f = 25.4$ mm). We use a 5×5 mm² square silica substrate, which is clamped to an xyz stepper motor positioner stage (Physik Instrumente GmbH, M-112.12S). The focusing and positioning of the sample is controlled by analyzing the reflected radiation with the MCT detector as a function of the stage positions.

2.2.2 Characterization of the CO₂ laser setup

The active medium of the laser consists of a CO₂–He–N₂ gas mixture filled into a discharge tube [8]. A radiofrequency (RF) signal (frequency: 83.5 MHz) pumps the N₂ molecules to the first vibrational level. The nitrogen molecules can collide with the CO₂–molecules and excite them into the first symmetric stretch vibrational mode (001) that acts as the upper lasing level. A decay from this state into the asymmetric stretch vibrational mode (100) occurs under the emission of a photon at wavelength 10.6 μm and is the prerequisite for lasing. Via collision with He–atoms the CO₂ molecules efficiently decay into their ground state before they are reexcited by the N₂ molecules.

The RF–pumping is gated by a 20 kHz transistor–transistor logic (TTL) signal and the mean laser power is controlled by adjusting the pulse width modulation (PWM)–duty cycle. Figure 2.2a illustrates the control of the laser pulse on the silica sample. The top row shows the TTL–pulses with a certain duty cycle that gates the RF–pumping signal. The effective laser output is illustrated on the second line and measured in figure 2.2b for three different PWM–duty cycles of the TTL signal. For this measurement the laser is only weakly diffracted by the AOM and the light was recorded with the MCT after reflection from a glass plate. The MCT detector is fast enough to record the pulse shapes of the CO₂ laser. However, we further treat the pulses incident on the silica substrate as cw–like, as we assume that the pulses timescale is much shorter than the heat transfer rate within the silica.

The AOM is driven at 40 MHz by a modulator driver, which in turn is modulated by an external voltage between 0 and 1 V. The modulation voltage height V defines the applied power to the AOM and thus determines the diffraction efficiency. By applying a certain voltage V for a time τ , we therefore define the length of the pulse and power incident on the silica sample as illustrated in figure 2.2a. Figure 2.2c shows the deflected mean laser power at the sample position relative to the mean laser power in the zeroth order as a function of AOM modulation voltage. We fit the curve to a parabola and describe the AOMs diffraction efficiency D as a function of the modulation voltage $U[V]$ as:

$$D(U) = a + bU + cU^2 \quad (2.1)$$

where we obtain the calibration parameters $a = 0.459 \pm 0.186$, $b = -7.573 \pm 0.691 \text{ V}^{-1}$ and $c = 29.312 \pm 0.566 \text{ V}^{-2}$. These parameters are used for setting the desired power of the fabrication pulse.

To characterize the dimensions of the CO₂–laser focal spot we use a partially gold–

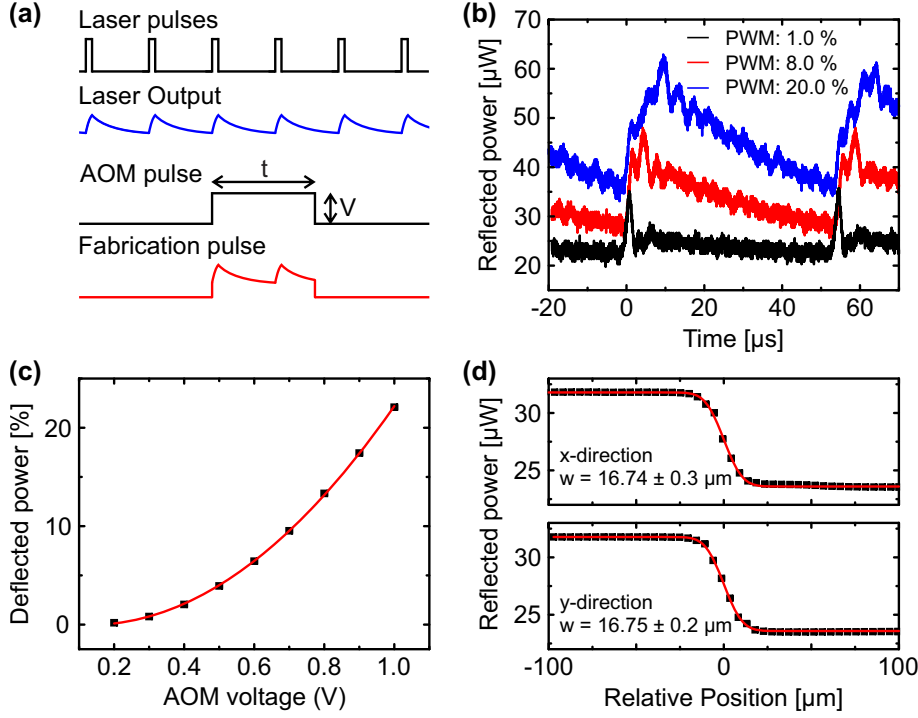


Figure 2.2. Performance of the CO₂ laser. (a) Generation of the fabrication pulse. The CO₂ laser is gated with a TTL-signal (top), resulting in the CO₂ laser pulse shapes shown by the blue curves. The AOM pulse height V and the pulse length τ determine the fabrication power and pulse width. The red curve shows the actual pulse that is applied to the silica substrate. The pulse shapes for different PWM are recorded in (b) using an AOM modulation voltage of 20 mV. (c) AOM calibration. The parabola fit is used for controlling the power during CO₂ ablation. (d) Reflection measurements across a sharp gold edge reveal a symmetrical focalspot.

coated glass plate with a defined sharp edge. The edge is moved across the focal spot, where we used an AOM voltage of 20 mV and a PWM of 2.5 %. Figure 2.2d shows the mean reflected power recorded with the MCT detector as a function of sample position. High power corresponds to gold and low power to the glass plate. We assume a Gaussian focal spot with intensity I :

$$I(r) = I_0 e^{-2\frac{r^2}{w^2}}, \quad (2.2)$$

with $r^2 = x^2 + y^2$ and fit the position dependent reflection $R(x)$ as:

$$R(x) = \text{erf}(\sqrt{2}x/w), \quad (2.3)$$

where $\text{erf}(x) = \int_0^x e^{-u^2} du$ is the error function. From this fit we obtain a symmetrical focal spot width w of $16.74 \pm 0.3 \mu\text{m}$ in x direction and $16.75 \pm 0.2 \mu\text{m}$ in y direction.

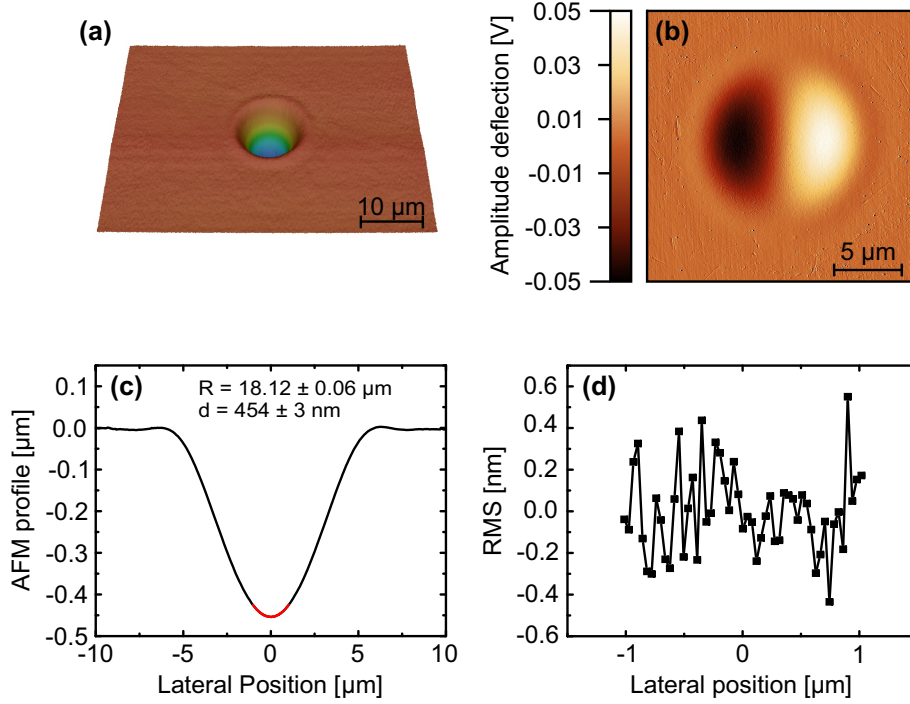


Figure 2.3. Ablated crater fabricated with a power of 250 mW and pulse length of $\tau = 58$ ms. (a) Height image obtained by a confocal scanning laser microscope. (b) AFM amplitude deflection image of the crater qualitatively shows a low surface roughness. (c) AFM height profile. The red line represents a circular fit in the vicinity of the center of the crater. Figure (d) shows the measured height data subtracted by the fit and we deduce a rms surface roughness of 0.2 nm.

2.3 Fabrication and analysis of the ablated structures

Having full control over the focus and the fabrication pulse incident on the silica substrate, we proceed to produce a large set of cavity geometries for different parameters. A typical ablated structure results from an exposure with 250 mW and a pulse length of 58 ms. We analyze the craters with a 3D confocal laser scanning microscope (Keyence, VK-x200) with a height resolution of 1 nm and lateral resolution of 5 nm. A 3D image from the laser scanning microscope is shown in figure 2.3a from which we deduce a crater depth of 432 ± 3 nm and a radius of curvature of $17.44 \pm 0.5 \mu\text{m}$. The radius of curvature is obtained by a circular fit 2 μm around the center of the crater.

For roughness measurements of the ablated craters we use an atomic force microscope (AFM) (Veeco Instruments, Veeco Dimensions 3100). The AFM is operated in the tapping mode in order to gain resolution [9]. Thereby the cantilever is driven slightly below its resonance frequency (typically around 290 kHz) at a fixed driving amplitude to maintain a constant force between tip and surface. Topological features of the surface

under study change the tip–surface interaction and alternate the oscillation amplitude. This error signal is fed to a feedback loop to keep the tip–surface height constant. Figure 2.3b shows the amplitude deflection image as the tip is scanned across a crater. This image allows for a qualitative statement regarding the smoothness of the surface in the ablated craters. The simultaneously recorded height image is shown in figure 2.3c and reveals a crater depth of 400 nm. The red line shows a circular fit $\pm 1 \mu\text{m}$ around the crater center and we deduce a radius of curvature of $18.12 \pm 0.06 \mu\text{m}$ in agreement with the measurements from the 3D confocal laser scanning image. Subtracting the curvature fit from the recorded data shows the surface roughness in figure 2.3d and we obtain a rms surface roughness of 0.2 nm, which is close to the height resolution of the AFM ($\approx 0.1 \text{ nm}$).

A general dependence of crater depth and radius of curvature is indicated in figure 2.4a and b. Here, the depths and radii are determined with the confocal laser scanning microscope for a set of three different fabrication powers (250, 255 and 260 mW). For each power, we observe a sublinear dependence of the depth on the exposure time, which is in contrast to the model assumed in [10], where an exponential increase of the crater depth is predicted for a prolonged laser pulse.

We use a wide range of fabrication parameters with powers ranging from 240 mW up to 900 mW and exposure times between 50 μs and 120 ms. The characterization of the created geometries is carried out by a phase interference microscope (Zygo Maxim–NT), the AFM and the confocal laser scanning microscope. We observe a wide range of radii of curvature of 1 mm down to less than 10 μm as indicated in figure 2.4a. Furthermore, the radius of curvature and the depth of the crater show a strong correlation, where we find deeper craters for low radii of curvature. We note that this correlation is relatively stable and independent of the power used. This behaviour represents a limitation to our current fabrication procedure: for a small cavity mode volume a small radius of curvature is desired but it comes at the cost of deep craters that result in a longer cavity length.

2.3.1 Effect of high power fabrication

We observe silica ejection in the AFM measurements shown in figure 2.5. Here, a crater using a power of 900 mW and an exposure time of 65 μs is fabricated, resulting in a radius of curvature of $33.08 \pm 0.24 \mu\text{m}$ with a corresponding depth of $298 \pm 3 \text{ nm}$. The AFM profile in figure 2.5a shows an enhanced surface roughness (rms 3.1 nm) in the vicinity of the crater compared to the vicinity of the crater fabricated with lower

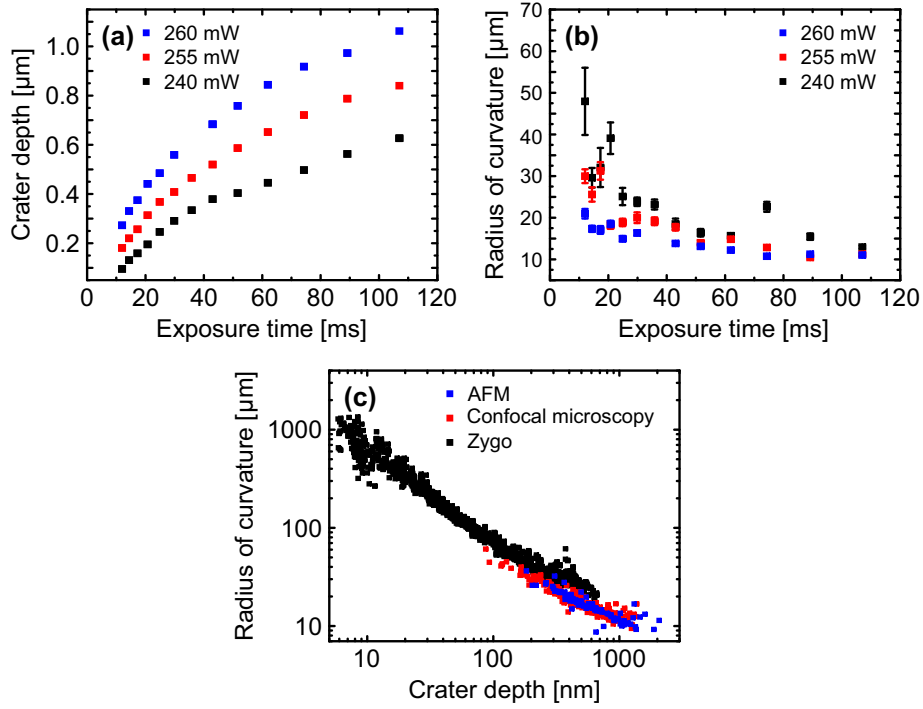


Figure 2.4. (a) Depth of the ablated craters vs exposure time for different powers. We observe a sublinear dependence on the exposure time. (b) Radius of curvature as a function of exposure time. (c) Overview of fabricated cavity geometries. We observe a strong correlation of between radius of curvature and depth. The craters are analyzed by a phase interference microscope, a scanning confocal microscope and atomic force microscopy (AFM).

laser power in figure 2.3 (rms surface roughness 0.8 nm). The melt ejection is also revealed by the amplitude deflection image in figure 2.5b. This finding suggests that the ablation dynamics of fused silica is significantly different for high laser powers. To gain a certain redundancy during the cavity experiment we fabricate several craters on the same silica substrate. It is therefore important to avoid melt ejection during the ablation process that may pollute previously processed craters. Consequently, we choose fabrication powers according to a regime where mass loss is dominated by either evaporation and/or dissociation [7]. For later cavity experiments, we focus on radii of curvatures between 10 and 20 μm with corresponding depths of 500 nm to 1.0 μm that are fabricated with moderate powers around 250 mW.

2.3.2 Additional smoothing pulse

As a last step in the fabrication protocol, we apply an additional short smoothing on the craters in order to quickly melt and flatten the surface. This smoothing pulse is chosen

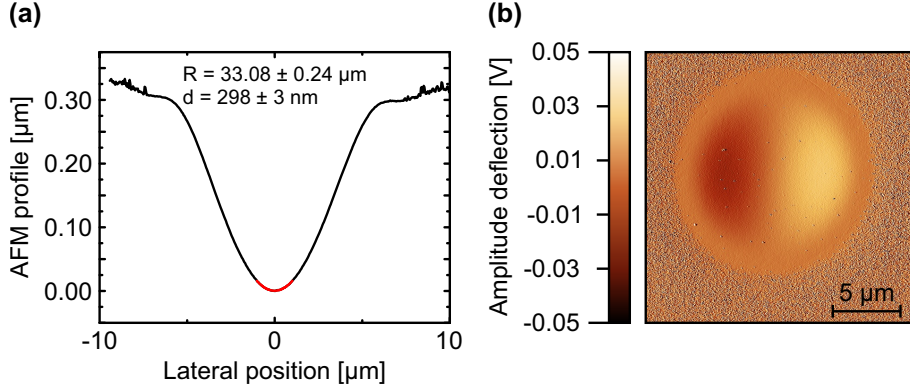


Figure 2.5. AFM profile (a) and amplitude deflection (b) image of an crater fabricated at high power (900 mW) and short exposure time (65 μs). The area around the ablated crater is significantly roughened due to silica ejection during the ablation process.

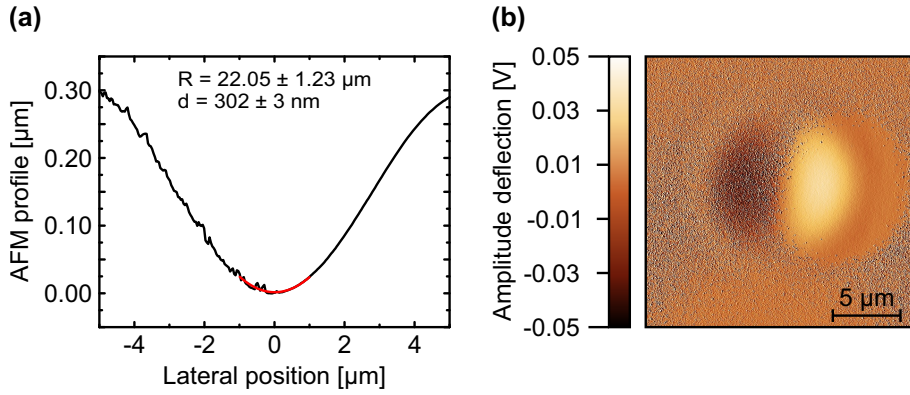


Figure 2.6. Influence of the smoothing pulse. A previously fabricated crater is polluted by silica ejection of a crater fabricated nearby with high power before subsequent treatment with a short smoothing pulse that is slightly misaligned with the initial crater. The smoothing pulse parameters are chosen such that the geometry of the crater is not significantly influenced as shown by the AFM profile in (a). The amplitude deflection image in (b) indicates the flattening effect of the smoothing pulse.

such that the geometry of the crater is not disturbed, while there is still a polishing effect.

A successful smoothing is shown in figure 2.6. Here, we first fabricate a crater with 250 mW and 58 ms. This crater is then purposely polluted by silica ejection of a crater shot at high power (500 mW; 198 μs) with the center at a distance of 20 μm from the initial crater. A subsequent smoothing pulse of 5 ms at 250 mW slightly misaligned with respect to the initial crater then flattens out the pollution from the high power pulse. This smoothing pulse is chosen such that the silica is locally melted and the surface tension in the molten silica layer smoothens out the surface roughness without a significant loss of mass. The AFM profile in figure 2.6a shows that this smoothing pulse

does not alternate the overall geometry and we also observe a flattening of the roughness in the amplitude image.

2.4 Conclusion

In conclusion we demonstrate the fabrication of concave structures by CO₂ laser ablation of a fused silica substrate. The silica substrate is then coated with a DBR consisting of either TiO₂/SiO₂ or Ta₂O₅/SiO₂ to build one end mirror of the miniaturized Fabry–Pérot cavity. By adjusting incident power and exposure times we can reproducibly control the desired concave mirror geometry. A large range of radii of curvature with very low surface roughness are produced with this technique. The possibility of fabricating craters with very low radii of curvature demonstrates the potential of these technique to lay the basis for the development of low mode volume tunable microcavities.

References

- [1] F. Laguarda, N. Lupon, and J. Armengol, [Applied Optics](#) **33**, 6508 (1994).
- [2] K. M. Nowak, H. J. Baker, and D. R. Hall, [Applied Optics](#) **45**, 162 (2006).
- [3] E. Mendez, K. M. Nowak, H. J. Baker, F. J. Villarreal, and D. R. Hall, [Applied Optics](#) **45**, 5358 (2006).
- [4] M. Wakaki, Y. Komachi, and G. Kanai, [Applied Optics](#) **37**, 627 (1998).
- [5] D. K. Armani, T. J. Kippenberg, S. M. Spillane, and K. J. Vahala, [Nature](#) **421**, 925 (2003).
- [6] H. M. Presby, A. F. Benner, and C. A. Edwards, [Applied Optics](#) **29**, 2692 (1990).
- [7] G. A. J. Markillie, H. J. Baker, F. J. Villarreal, and D. R. Hall, [Applied Optics](#) **41**, 5660 (2002).
- [8] M. Csele, *Fundamentals of light sources and lasers* (John Wiley & Sons, 2011).
- [9] N. Jalili and K. Laxminarayana, [Mechatronics](#) **14**, 907 (2004).
- [10] D. Hunger, C. Deutsch, R. J. Barbour, R. J. Warburton, and J. Reichel, [AIP Advances](#) **2**, 012119 (2012).

Chapter 3

Development and characterization of a small mode volume tunable microcavity

Adapted from:

Lukas Greuter, Sebastian Starosielec, Daniel Najer, Arne Ludwig, Luc Duempelmann, Dominik Rohner and Richard J. Warburton,

“A small mode volume tunable microcavity: development and characterization”,
[Applied Physics Letters](#) **105**, 121105 (2014).

We report the realization of a spatial and spectrally tunable air-gap Fabry-Pérot type microcavity of high finesse and cubic-wavelength-scale mode volume. These properties are attractive in the fields of opto-mechanics, quantum sensing and foremost cavity quantum electrodynamics. The major design feature is a miniaturized concave mirror with atomically smooth surface and radius of curvature as low as $10\text{ }\mu\text{m}$ produced by CO_2 laser ablation of fused silica. We demonstrate excellent mode-matching of a focussed laser beam to the microcavity mode and confirm from the frequencies of the resonator modes that the effective optical radius matches the physical radius. With these small radii, we demonstrate wavelength-size beam waists. We also show that the microcavity is sufficiently rigid for practical applications: in a cryostat at 4 K, the root-mean-square microcavity length fluctuations are below 5 pm.

3.1 Introduction

An enhanced interaction between photons and quantum emitters offers a rich field of quantum applications, including single photon transistors and emitter–emitter coupling. Tailoring the vacuum properties of high-Q optical resonators facilitates this enhanced interaction, and ultimately allows a coherent and reversal exchange of energy quanta, the strong coupling regime, challenging to achieve at optical frequencies. [1] In solid state systems, successful frameworks for cavity quantum electrodynamics (CQED) have been demonstrated with photonic crystal cavities [2, 3] and micropillars. [4] Both approaches allow only very limited in situ tuning.

Upcoming air-gap type resonators such as fiber-based microcavities [5–8] offer intrinsic tunability both in the spectral and spatial domains, and continual advancements in thin-film mirror techniques potentially enable ultra-high Q-factors. In this approach, the fiber terminus is fabricated into a concave mirror, where the radius of curvature $\mathcal{R} \approx \mathcal{O}(100\,\mu\text{m})$ defines the resulting cavity mode volume. Such systems however lack precise control over the fiber-to-cavity mode-matching and polarization. In fact, mode-matching is likely to be poor once \mathcal{R} is strongly reduced at which point the beam waist of the cavity mode is substantially smaller than the beam waist of the propagating mode in a typical optical fiber.

We present an open-geometry realization of a miniaturized high-Q Fabry-Pérot microcavity which allows both spectral and spatial tuning yet overcomes the disadvantages of a fiber-cavity related to mode-matching and polarization. The microcavity is optically accessed by free beam coupling allowing good mode-matching and offers full polarization control in excitation and detection. We present here significant improvements on an earlier approach [9–11]: radii of curvatures down to $10\,\mu\text{m}$ have been achieved and the microcavity finesse has been significantly enhanced. We demonstrate wavelength-size beam waists. We measure the frequencies of the microcavity modes in order to determine an effective “optical” \mathcal{R} and demonstrate that the physical and optical \mathcal{R} s match closely. The microcavity has a non-monolithic design and therefore is sensitive to acoustic noise. We quantify the acoustic noise under hostile cryostat conditions. Finally, we estimate relevant CQED parameters for a prototype solid-state emitter, a semiconductor quantum dot, and speculate that large cooperativities can be achieved.

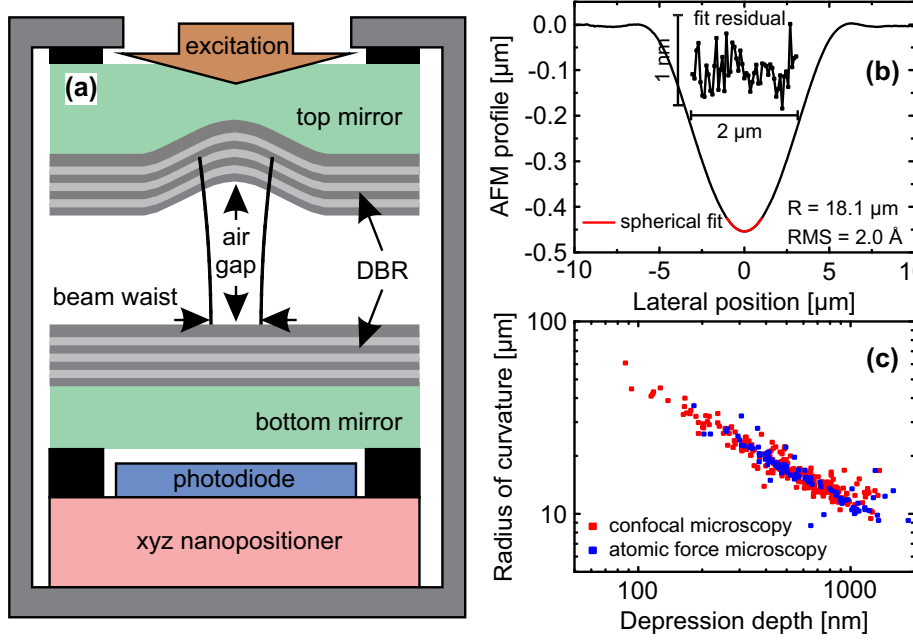


Figure 3.1. (a) The mechanical setup of the concave-planar Fabry-Pérot air-gap microcavity. A top mirror is produced by CO₂ laser ablation on fused silica and subsequent coating with a high-reflectivity DBR mirror. An opposing bottom mirror with similar reflectivity is mounted on a 3-axis nano-positioner for spectral and spatial tuning. Optical access is through the transparent top mirror substrate; the design of the bottom mirror remains application-dependent. (b) Profile following ablation of a top mirror template measured with atomic force microscopy. Defect-less near-parabolic craters are achieved with low roughness of 2 Å. (c) Radius of curvature versus crater depth following ablation. Control of the ablation process parameters gives a wide range of radii of curvatures down to 10 μm, with a linear correlation between radius and depth.

3.2 Experimental setup

3.2.1 Cavity design

A highly reflective planar-concave mirror pair on fused silica, separated by a wavelength-sized air-gap, forms the high-finesse resonator and is shown in figure 6.2a. Spectral and spatial tunability is achieved by mounting the planar bottom mirror on a 3-axis piezo stack (attocube ANPx/z51, Germany) allowing for sub-nm precise positioning relative to the top mirror. The whole microcavity setup is mounted on an additional 3-axis piezo stack (attocube ANPx/z101) allowing for free positioning with respect to an aspherical lens with NA = 0.55 (not shown). The transmitted intensity is measured with a Si photodiode mounted below the bottom substrate.

This scheme offers control of mode-matching to the microcavity mode [12] and full

polarization control both in excitation and detection. In stark contrast, mode-matching in fiber-microcavities is inherently difficult to achieve: In the regime of high radius of curvature, for perfect axis alignment, the spatial overlap mismatch of the fiber and cavity mode dominates the coupling efficiency. With fiber beam waist $w_{\text{fib}} \approx 3.5 \mu\text{m}$ and cavity beam waist $w_{\text{cav}} \approx 2.3 \mu\text{m}$ (these are typical parameters for a single mode fiber and a cavity with radius of curvature $\mathcal{R} \approx 100 \mu\text{m}$ and a length of $3 \mu\text{m}$), the coupling efficiency is $\epsilon = [2w_{\text{fib}}w_{\text{cav}}/(w_{\text{fib}}^2 + w_{\text{cav}}^2)]^2 \approx 82\%$ [6], a reasonable result in the high- \mathcal{R} regime. However, if the radius is reduced to $\mathcal{R} \approx 10 \mu\text{m}$ (corresponding to $w_{\text{cav}} = 1.4 \mu\text{m}$), the mode overlap drops to $\epsilon \approx 47\%$. In addition, for small radii the effect of wavefront mismatch becomes equally prominent [6], reducing the coupling efficiency further towards $\epsilon \approx 23\%$.

For optical characterization we employ different sets of mirror coatings. In a high-reflectivity configuration (HRC), both top and bottom mirror are coated with a $\text{Ta}_2\text{O}_5/\text{SiO}_2$ distributed Bragg reflector (DBR) by ion beam sputtering (Evaporated Coatings Inc., USA) with reflectivity reaching $R \approx 99.980\%$. The low-reflectivity configuration (LRC) consists of a $\text{TiO}_2/\text{SiO}_2$ DBR top mirror coating of proprietary fabrication (OIB GmbH, Germany) with $R > 99.8\%$ paired with a low reflective bottom mirror consisting of a polished GaAs substrate coated with a structured 80 nm Au film ($R \approx 98\%$) defined by lift-off electron beam lithography. In both configurations the DBR stopband is centered at 940 nm .

The compact microcavity setup operates both under ambient conditions and also at low temperature. The entire microcavity setup fits into a 50 mm diameter stainless steel tube containing He exchange gas, the tube is then inserted into a liquid He bath cryostat. The 4 K conditions favor the mechanical properties of the nano-positioners, reduce photocurrent noise, and demonstrates the low-temperature conformance required for nanostructure systems. The cryostat itself is mounted on an optical table with passive vibrational isolation from the building floor and is situated in a steel chamber damped with acoustic foam.

3.2.2 Top mirror fabrication

Prior to coating, the top mirror template is fabricated by laser ablation of fused silica. [13, 14] We use an RF-pumped CO_2 -laser with wavelength $10.6 \mu\text{m}$ operating at a repetition rate of 20 kHz . A typical duty cycle of 8% results in an average output power of 7.8 W . The light is diffracted by an acousto optical modulator, which allows sufficient control over the incident power and pulse train length in the first order diffracted beam. We

reject back-reflection by a linear polarizer and quarter-wave plate. The laser intensity fluctuation in the entire system is less than 1 %. The laser is then focused by an aspherical ZnSe lens ($\text{NA} = 0.45$) onto the silica surface. The silica substrate is mounted on a 3-axis stepper motor stage. In contrast to Hunger *et al.*[6], a nitrogen-cooled HgCdTe detector monitors the focal point reflectance as a function of substrate displacement achieving micrometer control over the substrate alignment with respect to the incident laser light. After ablation, the resulting craters are characterized by confocal scanning microscopy and atomic force microscopy. We observe rotationally symmetric micro-craters with a root-mean-square (RMS) surface roughness as low as 2 Å (figure 6.2b). Incident powers of 250 mW with pulse length between 10 – 100 ms result in a controlled range of craters with a depth of a few hundred nanometers to $1.5\text{ }\mu\text{m}$ and corresponding radii of curvature down to less than $10\text{ }\mu\text{m}$ (figure 6.2c). These geometries result from the strong absorption of the CO_2 -laser radiation by vibrational modes of the silica, where the melting and evaporation of the material within the first few micrometers of the substrate's surface is roughly proportional to the local intensity. Significantly, the surface tension of the molten silica smooths the ablation craters.

As a central result of this work, craters with radii of curvature down to less than $10\text{ }\mu\text{m}$ are consistently achieved by ablation, reducing the previous reported minimum value ($20\text{ }\mu\text{m}$ [13]) by more than a factor of two. We attribute the superior production scheme to an enhanced alignment precision. We observe a strong link between the crater radius and depth in this one-shot fabrication process (figure 6.2c), independent of the experimental parameters (power and pulse train length). For microcavities with $\mathcal{R} \simeq 10\text{ }\mu\text{m}$, the corresponding depth is $\simeq 1\text{ }\mu\text{m}$, ideally suited to stable low mode volume cavities. The link extends to the very smallest radius, $\mathcal{R} = 5.2\text{ }\mu\text{m}$, where the depth is $5.0\text{ }\mu\text{m}$, unsuitable for a stable cavity, and additional fabrication steps become necessary, the focus of future work.

3.3 Optical performance

Performance characterization of the microcavity is carried out using transmission detection at a fixed probing wavelength $\lambda = 950\text{ nm}$. Coarse tuning of the microcavity length is achieved by the friction-based inertial driving mode of the nano-positioner (attocube ANPz51), adjusting the air-gap in $\approx 10\text{ nm}$ steps over a 2.5 mm traveling range. For fine tuning over several micrometers, a DC piezo voltage V_z is applied. Figure 3.2a shows the resonance associated with the fundamental microcavity mode (degenerate with respect

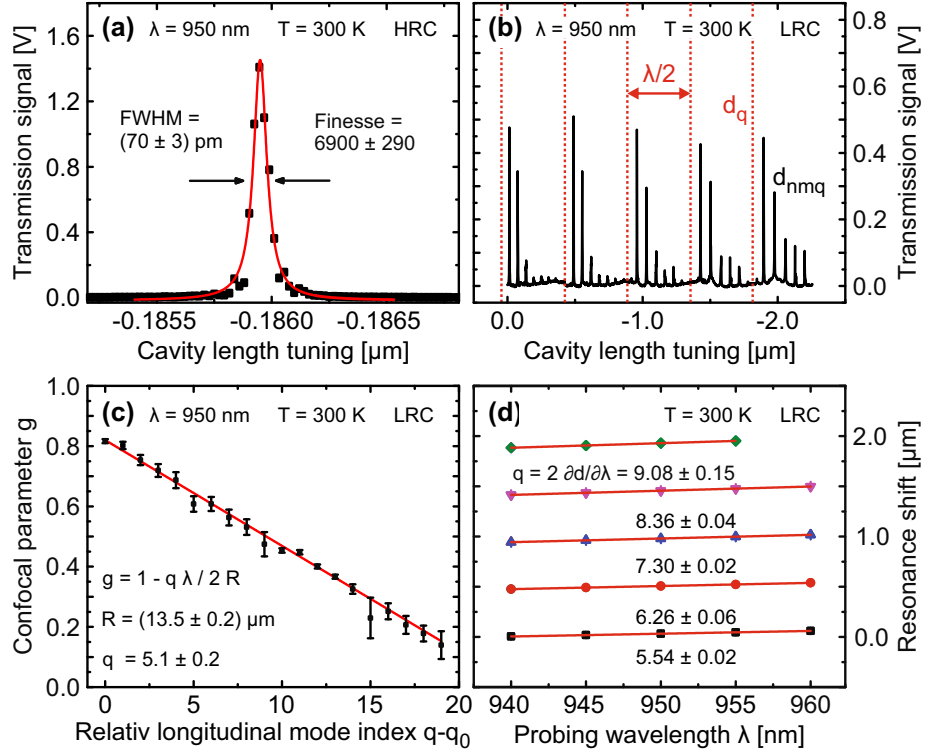


Figure 3.2. Cavity transmission with relative length tuning scans in high-reflectivity configuration (HRC) and low-reflectivity configuration (LRC). (a) An exemplary resonance in HRC. The full-width-at-half-maximum (FWHM) detuning length of (70 ± 3) pm is measured, corresponding to a finesse of $6,700 \pm 290$. (b) Intentionally poor mode-matching in LRC reveals the transverse modes giving a handle on the confocal parameter g . (c) The linear relation between g and longitudinal mode index q follows the Gaussian optics model and reveals the top mirror radius of curvature $R = (13.5 \pm 0.2) \mu\text{m}$. The intercept at $g = 1$ reveals the longitudinal mode index offset to be $q_0 = 5.1 \pm 0.2$. (d) Independent measurements of the longitudinal mode index for the first five resonances are in very good agreement with q_0 .

to both possible polarizations). There is very good mode-matching: the integrated signal of the fundamental mode is 85 % of the signal integrated over the fundamental and higher order transverse microcavity modes. To reveal the exact location of the higher order modes, the mode-matching can be made poor intentionally by displacing the entire microcavity setup vertically with respect to the objective lens: Figure 3.2b shows the transmitted signal as a function of microcavity length tuning, where each peak arises from a particular transverse microcavity mode.

3.3.1 Finesse

In cavity performance, a representative figure of merit is the finesse usually defined as $F = \Delta\nu_{\text{FSR}}/\delta\nu$, [15] where $\delta\nu$ is the resonance linewidth and $\Delta\nu_{\text{FSR}}$ is the free spectral range (FSR), i.e. the frequency spacing between subsequent longitudinal modes. This definition is ill-defined for DBR-based microcavities as the FSR may become comparable (or even larger) than the DBR stopband. Instead we identify $2\pi/F$ as the fractional energy loss per round-trip at resonance, or $F = c/(2d\delta\nu)$, where we introduce the microcavity length d . On tuning d experimentally, the FWHM resonance width δd is immediately accessible. Neglecting the effects of the Gaussian optics (discussed below), we identify $\delta\nu/\nu = \delta d/d$ and measure $F = \lambda/(2\delta d)$ in the distance domain for fixed vacuum wavelength λ . Exemplary data in figure 3.2a show resonance widths of $\delta d = (70 \pm 3)$ pm and thus $F = 6,700 \pm 290$ with good lorentzian lineshape (recorded here under ambient conditions). Resonances with FWHM below 30 pm have been resolved under the same conditions (thus $F \approx 15,000$), but their non-lorentzian lineshapes imply a low-frequency broadening as quantified by acoustic noise measurements (also discussed below). In the absence of other cavity losses, reflectivities $R_{1,2} \simeq 99.980\%$ as specified for the DBR in HRC, the expected finesse is $F = \pi\sqrt[4]{R_1 R_2}/(1 - \sqrt{R_1 R_2}) \simeq 15,700$, in very good agreement with the largest observed values.

3.3.2 Radius of curvature

We model the mode structure of the microcavity with Gaussian optics, a similar approach to Muller *et al.*[8] Under the paraxial approximation of optical wavefront normals making only a small angle to the direction of propagation, the propagating electromagnetic field are described by Hermite-Gaussian TEM_{*nm*} modes. Imposing two reflective boundaries, the standing wave field is at resonance at mirror separations

$$d_{qnm} = \left[q + \frac{n+m+1}{\pi} \cos^{-1} \sqrt{g} \right] \frac{\lambda}{2}, \quad (3.1)$$

where q (n, m) is the longitudinal (transverse) resonator mode index and $|g| < 1$ is the geometry-dependent confocal parameter. [15] In a planar-concave configuration $g = 1 - d/\mathcal{R}$ depends itself on the mirror separation d and on the concave mirror's radius of curvature \mathcal{R} . The focal point is located at the planar mirror with beam waist $w_0 = \sqrt{\lambda/\pi} \times \sqrt[4]{d\mathcal{R} - d^2}$.

The above analysis holds for idealized mirrors of unity reflection amplitude coeffi-

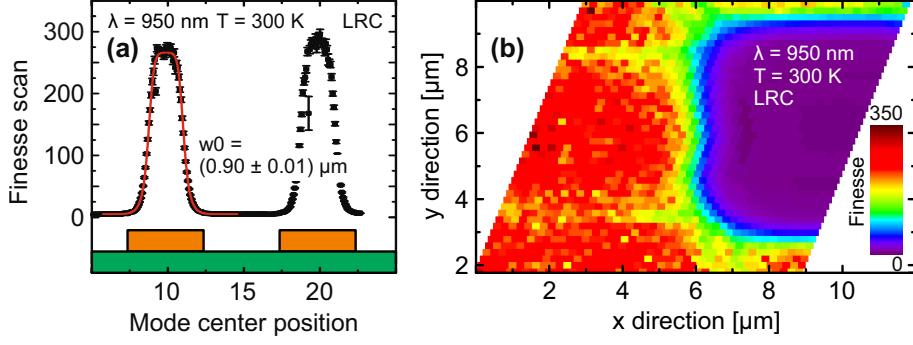


Figure 3.3. Cavity mode beam waist measurements using a Au knife-edge structured bottom mirror. (a) A knife edge with 10 μm periodicity for *in-situ* calibration. A spatial scan of the finesse over knife-edge fits to the model with a beam waist of $w_0 = (0.90 \pm 0.01) \mu\text{m}$. (b) Demonstration of two-dimensional microcavity scanning microscopy with a finesse scan over a Au on GaAs panel structure.

cient. This is not realized in the experiment: the DBR thin-film structures show significant group delay τ even at the stopband center wavelength. [16] A corresponding effective phase penetration depth $d_{\text{DBR}} = c/(2\tau)$ of the intracavity field into the DBR affects the resonances by a renormalization of the microcavity length $d_{\text{renorm}} = d_{\text{air-gap}} + d_{\text{DBR,bottom}} + d_{\text{DBR,top}}$ and radii $\mathcal{R}_{\text{renorm}}$. The resonance analysis is sensitive to the renormalized microcavity parameters, which in turn are the relevant parameters for CQED applications. We therefore drop the renormalized index in notation and differentiate to the geometrical parameters when needed.

According to eq. (3.1), the splitting of the higher order transverse modes depends on the confocal parameter $g = 1 - d/\mathcal{R}$ and gives a handle on the effective radius of curvature \mathcal{R} . An explicit solution of d is cumbersome owing to the implicit nature of eq. (3.1) through $g(d)$. We instead exploit the algebraic structure of the splitting and extrapolate g_q at unphysical resonances $m + n + 1 \rightarrow 0$ for each longitudinal mode q with $d_q = q\lambda/2$. Figure 3.2c shows the extracted confocal parameter g_q as a function of integer q with a free offset parameter q_0 . The Gaussian model relation $g = 1 - q\lambda/(2\mathcal{R})$ is reproduced for renormalized mirror radius $\mathcal{R} = (13.5 \pm 0.2) \mu\text{m}$ and offset $q_0 = 5.1 \pm 0.2$. An independent measurement of the absolute longitudinal mode index $q = 2\partial d/\partial\lambda$ is performed by changing the probe wavelength (figure 3.2d) for the first five modes. With the exception of the lowest mode close to the mechanical contact of the mirrors, both the integer spacing as well the offset $q_0 \approx 5.3$ are in very good agreement with the Gaussian optics treatment. In comparison, confocal laser scanning microscopy reveals a geometric radius $\mathcal{R}_{\text{geom}} = 11.2 \mu\text{m}$.

3.3.3 Beam waist

For measurement of the Gaussian beam waist parameter w_0 in LRC, the Au bottom mirror is structured with electron beam lift-off lithography into a periodic knife-edge with segment dimensions of $5\mu\text{m}$ and periodicity of $10\mu\text{m}$. A finesse scan for each position is performed as the edge is moved in the lateral x direction through the microcavity mode. We model the effective reflectivity of the bottom mirror as $R_2^{\text{eff}} = \alpha R_{\text{Au}} + (1 - \alpha) R_{\text{GaAs}}$, namely the average reflectivity of the GaAs substrate and Au, where $\alpha(x) = \frac{1}{2}[1 + \text{erf}(\sqrt{2}x/w_0)]$ is the spatial overlap of the Gaussian mode intensity with the Au segments. This simplistic model describes well the observed finesse as a function of bottom mirror position as shown in figure 3.3a. We determine the beam waist parameter to be $w_0 \approx (0.90 \pm 0.01)\mu\text{m}$, equivalently $w_0/\lambda \approx 0.95 \pm 0.01$: w_0 is smaller than the wavelength. For quantitative comparison of a planar-concave microcavity in Gaussian optics, the beam waist at the focus evaluates to $w_0 = \sqrt{\lambda/\pi} \times \sqrt[4]{d\mathcal{R} - d^2} \approx 1.2\mu\text{m}$ for $d \approx 2.5\mu\text{m}$ and $\mathcal{R} \approx 13\mu\text{m}$, in good agreement with the experimental result. We use a one dimensional transfer matrix method to calculate the intracavity electric field distribution and estimate an effective energy distribution length $L_e = \int \epsilon_r(z) E^2(z) dz / (\epsilon_r(z_0) E^2(z_0)) \approx 1.34\mu\text{m}$ with respect to the field's antinode $z = z_0$ inside the airgap, the prospective location of an emitter. The corresponding effective mode volume is then $V = \pi w_0^2/2 \times L_e \approx 2.0\lambda^3$, i.e. close to a cubic-wavelength in size.

3.3.4 Microcavity microscopy

The above scheme is readily extended to two-dimensional microcavity scanning microscopy, sensitive to the local reflection amplitude coefficient (both in magnitude and phase) with wavelength-scale spatial resolution. A proof of principle is demonstrated in figure 3.3b for a finesse scan over a Au on GaAs panel structure allowing imperfections in the shape and Au coverage to be detected.

We use the strong dependence of the resonance location to the microcavity length as a highly sensitive acoustic noise microphone. Tuning the microcavity to the maximum slope at the resonance edge (working point A in figure 3.4a) gives a linear response in transmission intensity to small air-gap length fluctuations, and hence direct access to the acoustic noise power spectrum affecting the microcavity. Parasitic noise sources such as laser intensity fluctuations and electrical noise are probed at maximum resonance (B) and at significant detuning (C), respectively. The laser intensity is adjusted at

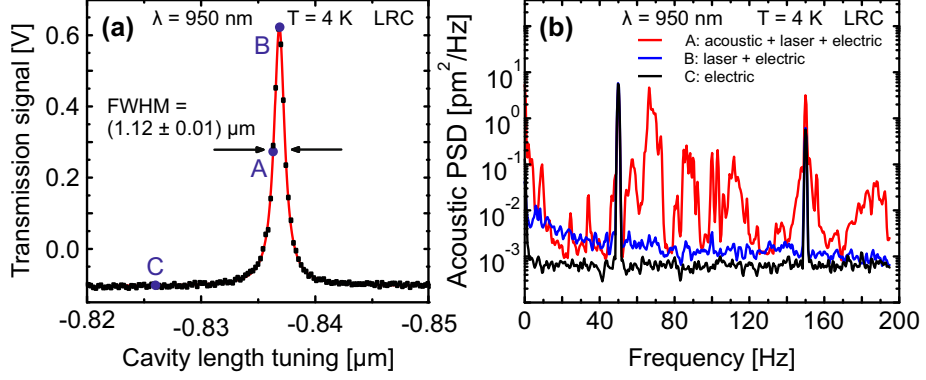


Figure 3.4. Acoustic noise measurements in the low reflectivity configuration: a fluctuating microcavity length results in a fluctuating resonance position for a constant wavelength. (a) Three working points with sensitivity to different noise sources. Calibration to acoustic amplitudes is given by the resonance slope at working point A. (b) Acoustic noise power spectral density at each working point. Red line at A reveals the acoustic noise contribution superimposed on detection noise such as laser intensity noise (blue line, B) and electric noise (black line, C). Noise power is below $1 \text{ pm}/\sqrt{\text{Hz}}$ with the exception of a small band at about 70 Hz. The integrated RMS noise amplitude is 4.3 pm.

each working point to give the same transmitted intensity. The resonance slope in A determines the calibration to acoustic amplitudes and is used in B and C for direct comparison (figure 3.4b).

Electrical noise (C) sets the detectable equivalent noise floor to $\approx 8 \times 10^{-4} \text{ pm}^2/\text{Hz}$. Mains pick-up noise (50 Hz and odd-multiples) is present in the detection channel. From the observed spectral shape in B, laser intensity fluctuations are at most the same order of magnitude as the electrical noise. The acoustic noise spectrum (A) shows rich resonance-like features. However, the acoustic noise amplitudes are still below $10 \text{ pm}^2/\text{Hz}$, and with the exception of the two major contributions at 62 – 74 Hz and 150 Hz well below $1 \text{ pm}^2/\text{Hz}$. Above 200 Hz no further significant acoustic noise contribution is detected (not shown). The acoustic noise RMS amplitude is $\delta d_{\text{acoustic}} = 4.3 \text{ pm}$ which must be compared to the FWHM resonance microcavity length $\delta d_{\text{resonance}} = \lambda/(2F) = 71 \text{ pm}$ in the HRC setup. If a tolerance of $\delta d_{\text{acoustic}}/\delta d_{\text{resonance}} \leq 10^{-1}$ is acceptable, a finesse of $F \lesssim 11,000$ is unaffected by acoustic noise. Indeed in the experiment, resonances of $\delta d_{\text{resonance}} = 30 \text{ pm}$ corresponding $F \approx 15,000$ consistently feature non-lorentzian lineshapes and in the light of this analysis, this arises most likely from the acoustic noise.

3.4 Conclusion

In conclusion, we have demonstrated the experimental realization of a fully tunable open-gap Fabry-Pérot microcavity. The microcavity modes have small volume and are well described with Gaussian optics. We achieve excellent mode-matching to the microcavity mode from a propagating Gaussian beam. The major facilitators are, first, the successful fabrication of atomically smooth, small radius of curvature top mirrors by CO₂ laser ablation and second, a rigid piezo-driven nano-positioning system.

We speculate further on the cooperativity that can be reached with our setup when operated with an InGaAs self-assembled quantum dot in a GaAs host matrix grown on a GaAs/AlGaAs DBR. For this configuration, due to the high phase penetration depth into the DBR, the renormalized microcavity length is estimated to be $8.5\,\mu\text{m}$. A Gaussian optics estimate yields an average beam waist of $2.0\,\mu\text{m}$. The energy distribution length is $0.37\,\mu\text{m}$ with respect to the GaAs host, corresponding to an effective mode volume of $V = 2.4\,\mu\text{m}^3$ or $120(\lambda/n)^3$. The vacuum electric field amplitude is estimated to be $E_{\text{vac}} = 2.0 \times 10^4\,\text{V/m}$ at the location of the quantum dot. A typical free space radiative lifetime of $0.8\,\text{ns}$ corresponds to an optical dipole moment of $\mu_{12} = 1.2\,\text{nm} \times e$ resulting in an emitter-cavity interaction energy of $\hbar g = \mu_{12} E_{\text{vac}} = 24\,\mu\text{eV}$. The demonstrated finesse of 6,700 translates into a photon decay of $\hbar\kappa = 22\,\mu\text{eV}$. Quantum dot linewidths as low as $\hbar\gamma = 2\,\mu\text{eV}$ are routinely achieved, resulting in an upper limit cooperativity as high as $C = 2g^2/(\kappa\gamma) \approx 26$. Active acoustic shielding and a further reduction in $\kappa \ll g$ by supermirror DBR coatings ($R > 99.995\%$) may even enhance the cooperativity towards 100.

The authors thank M. Montinaro who performed the electron-beam lithography of the checkerboard calibration sample. The authors gratefully acknowledge financial support by SNF and NCCR QSIT.

References

- [1] K. J. Vahala, [Nature](#) **424**, 839 (2003).
- [2] K. Hennessy, A. Badolato, M. Winger, D. Gerace, M. Atatüre, S. Gulde, S. Fält, E. L. Hu, and A. Imamoglu, [Nature](#) **445**, 896 (2007).
- [3] T. Yoshie, A. Scherer, J. Hendrickson, G. Khitrova, H. M. Gibbs, G. Rupper, C. Ell, O. B. Shchekin, and D. G. Deppe, [Nature](#) **432**, 200 (2004).
- [4] J. Reithmaier, G. Sek, A. Löffler, C. Hofmann, S. Kuhn, S. Reitzenstein, L. Keldysh, V. Kulakovskii, T. Reinecke, and A. Forchel, [Nature](#) **432**, 197 (2004).
- [5] T. Steinmetz, Y. Colombe, D. Hunger, T. W. Hänsch, A. Balocchi, R. J. Warburton, and J. Reichel, [Applied Physics Letters](#) **89**, 111110 (2006).
- [6] D. Hunger, T. Steinmetz, Y. Colombe, C. Deutsch, T. W. Hänsch, and J. Reichel, [New Journal of Physics](#) **12**, 065038 (2010).
- [7] A. Muller, E. B. Flagg, M. Metcalfe, J. Lawall, and G. S. Solomon, [Applied Physics Letters](#) **95**, 173101 (2009).
- [8] A. Muller, E. B. Flagg, J. R. Lawall, and G. S. Solomon, [Optics Letters](#) **35**, 2293 (2010).
- [9] R. J. Barbour, P. A. Dalgarno, A. Curran, K. M. Nowak, H. J. Baker, D. R. Hall, N. G. Stoltz, P. M. Petroff, and R. J. Warburton, [Journal of Applied Physics](#) **110**, 053107 (2011).
- [10] D. Ziyun, H. V. Jones, P. R. Dolan, S. M. Fairclough, M. B. Wincott, J. Fill, G. M. Hughes, and J. M. Smith, [New Journal of Physics](#) **14**, 103048 (2012).
- [11] S. Dufferwiel, F. Fras, A. Trichet, P. M. Walker, F. Li, L. Giriunas, M. N. Makhonin, L. R. Wilson, J. M. Smith, E. Clarke, M. S. Skolnick, and D. N. Krizhanovskii, [Applied Physics Letters](#) **104**, 192107 (2014).
- [12] H. Kogelnik and T. Li, [Proceedings of the IEEE](#) **54**, 1312 (1966).
- [13] D. Hunger, C. Deutsch, R. J. Barbour, R. J. Warburton, and J. Reichel, [AIP Advances](#) **2**, 012119 (2012).

- [14] B. Petrak, K. Konthasinghe, S. Perez, and A. Muller, [Review of Scientific Instruments](#) **82**, 123112 (2011).
- [15] W. Nagourney, *Quantum Electronics for Atomic Physics* (Oxford University Press, 2010).
- [16] D. I. Babic and S. Corzine, [Quantum Electronics, IEEE Journal of](#) **28**, 514 (1992).

Chapter 4

Strong coupling of a quantum dot in a tunable microcavity

Adapted from:

Lukas Greuter, Sebastian Starosielec, Andreas V. Kuhlmann, and Richard J. Warburton,

“Towards high cooperativity coupling of a quantum dot in a tunable microcavity”,
Submitted, [arXiv:1504.06223](https://arxiv.org/abs/1504.06223) (2015).

We investigate the strong coupling regime of a self-assembled quantum dot in a tunable microcavity with dark-field laser spectroscopy. The high quality of the spectra allows the lineshapes to be analyzed revealing subtle quantum interferences. Agreement with a model calculation is achieved only by including exciton dephasing which reduces the cooperativity from a bare value of 9.0 to the time-averaged value 5.5. In the pursuit of high cooperativity, besides a high-Q and low mode-volume cavity, we demonstrate that equal efforts need to be taken towards lifetime-limited emitter linewidths.

4.1 Introduction

Cavity quantum electrodynamics (QED) involves an exchange of energy quanta between a single emitter and a cavity photon. The coupling rate $\hbar g = \mu_{12} E_{\text{vac}}$, depending on the emitter's dipole moment μ_{12} and the vacuum electric field at the location of the emitter E_{vac} , sets the relevant timescale of the coupled dynamics. If g is considerably smaller than the emitter relaxation rate γ or the cavity photon decay rate κ , on resonance the cavity mode acts as an additional decay channel to the emitter giving rise to an enhanced spontaneous emission rate (the Purcell effect of the weak coupling regime). If g is much larger than the energy loss rates, a coherent exchange of energy quanta takes place giving rise to new eigenstates, “polaritons”, split in energy by $2\hbar g$ (the strong coupling regime). The efficacy of the coherent coupling is commonly denoted by the cooperativity parameter $C = 2g^2/(\kappa\gamma)$, the figure of merit for this work. The coherent exchange was first realized with single Cs atoms in a high finesse cavity [1].

The strong coupling regime is a potentially powerful tool in quantum information processing [2], notably in quantum networks [3], since it enables for instance atom–atom entanglement [4] or the distribution of quantum states [5]. Furthermore, strong coupling enables a nonlinear photon–photon interaction and hence the observation of photon blockade [6, 7], a prerequisite for the creation of a single photon transistor [8, 9].

It is clearly desirable to implement cavity–QED in the solid–state as the solid–state host acts as a natural trap for the emitter. Furthermore, on–chip integration of multiple elements is feasible. As emitter, self–assembled quantum dots have desirable properties: high oscillator strength, narrow linewidths and weak phonon coupling [10]. As host, a semiconductor such as GaAs is very versatile: heterostructures can be realized; there is a wide array of post–growth processing techniques. Photoluminescence experiments on single InGaAs SAQD coupled to a photonic crystal cavity or a micropillar cavity revealed an anticrossing, the signature of the strong coupling regime [11–13]. For micropillars, recent experiments exhibit cooperativity values of around $C \simeq 3$ [14]. For photonic crystal cavities, a much higher C is achieved [15] but C is skewed by the fact that $g \gg \gamma$ yet $g \gtrsim \kappa$. The photon decay rate κ at the emitter wavelength is relatively high in both geometries, limiting the cooperativity. In addition, micropillars and photonic crystals offer only limited spectral tuning to the emitter transition, and spatial positioning of the emitter relative to the cavity antinode is achieved either by good fortune or by fabricating the cavity around a particular emitter [16, 17]. These are challenging issues resulting in a low yield.

In this work we demonstrate a strong coupling of a single self-assembled InGaAs quantum dot to a fully tunable, miniaturized Fabry–Pérot cavity [18, 19]. The coupled emitter–cavity system is investigated by dark-field laser spectroscopy, yielding extremely high spectral resolution, high sensitivity, a high contrast and good mode-matching. The strong coupling regime is accessed definitively: we reach a cooperativity of $C = 5.5$, significantly larger than that achieved with micropillars [14] or a fibre-cavity [20]. The high quality of the data allows for a quantitative lineshape analysis. We demonstrate an interference in the polariton gap. However, the interference is less pronounced than expected from the “standard model”, the Jaynes–Cummings Hamiltonian. We show that the missing interference arises as a consequence of an additional emitter broadening. Including the emitter broadening allows us to reproduce both the exact lineshapes and polariton eigenenergies with a single parameter set for all cavity–emitter detunings. A key point emerges. Achieving a high cooperativity requires more than a focus on the cavity properties (small mode volume and high Q -factor): this has to be matched with an equal effort on improving the linewidth of the emitter. Here, we show that suppressing the emitter broadening would yield a cooperativity as high as $C = 9.0$ even with the present microcavity. Characterization of the quantum dots shows that here the main emitter broadening arises from a spectral fluctuation (rather than a true dephasing process): the fluctuations can be circumvented in lower-noise devices. Our system therefore represents an extremely promising route to implementing cavity–QED in the solid-state.

4.2 Setup

The emitter is a self-assembled InGaAs quantum dot grown by MBE at UCSB California. The background doping is small and p-type. The details of the heterostructure are depicted in figure 6.2b: a 32.5 pair $\lambda/4$ AlGaAs/GaAs distributed Bragg reflector (DBR) is terminated by a λ layer of GaAs which incorporates the InGaAs quantum dots in the center. Further details of the sample are given in Appendix A.1. The bottom DBR with reflectivity $R_{\text{bot}} = 99.99\%$ forms the planar end mirror of the cavity. The concave top mirror consists of a fused silica substrate with a depression formed by CO₂ laser ablation [21], and is coated with a Ta₂O₅/SiO₂ DBR of reflectivity $R_{\text{top}} = 99.95\%$. The radius of curvature is approximately $13\,\mu\text{m}$. The bottom semiconductor sample is mounted on an xyz piezo stack that allows for sub-nm positioning with respect to the top mirror enabling both spectral and spatial tuning. The whole microcavity is then

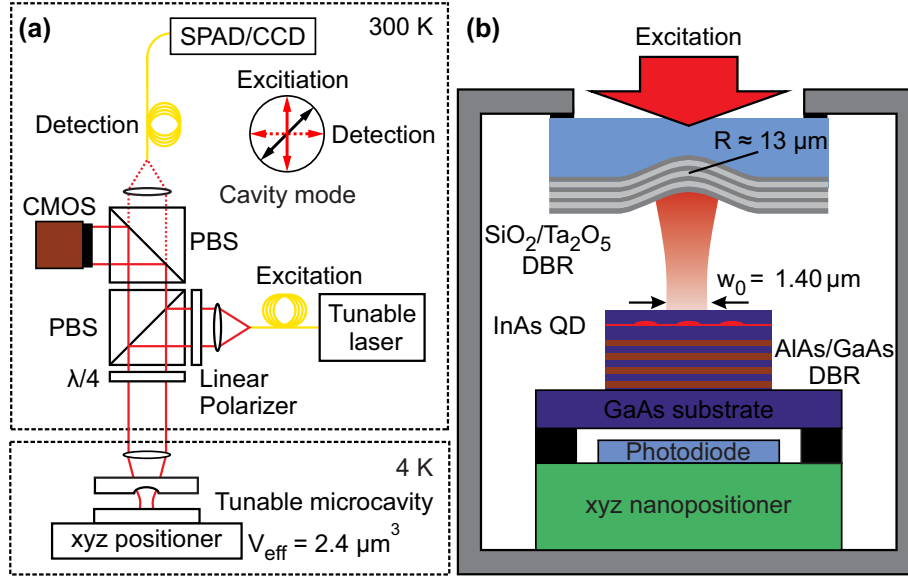


Figure 4.1. (a) Experimental setup to probe the cavity–quantum dot system. The microscope head is at room temperature and consists of two polarizing beam splitters (PBS), a linear polarizer and a $\lambda/4$ waveplate. (b) Microcavity setup with a GaAs/AlGaAs bottom mirror and a curved top mirror with radius of $13 \mu\text{m}$ coated with $\text{Ta}_2\text{O}_5/\text{SiO}_2$ DBR. The InGaAs quantum dots are embedded in a semiconductor heterostructure, at distance $\lambda/2$ from the surface and $\lambda/2$ from the bottom mirror.

mounted on another xyz piezo stack that allows the microcavity to be positioned with respect to an aspherical coupling lens ($\text{NA} = 0.55$), facilitating efficient mode matching with the excitation beam. A Si–photodiode mounted underneath the bottom mirror is used for transmission measurements to characterize and optimize the mode matching. By determining the longitudinal mode index $q_0 = 2\partial L/\partial\lambda = 18$, we estimate an effective cavity length of $L = q_0\lambda/2 = 8.5 \mu\text{m}$. From these parameters, a Gaussian optics estimate results in a beam waist of $w_0 = 1.4 \mu\text{m}$ at the sample. The cavity finesse is 4,000; the quality factor is $Q = 6 \times 10^4$.

4.3 Excitation and Detection

We measure the coupled cavity–quantum dot dynamics with confocal cross–polarized dark–field laser spectroscopy [22], sketched in figure 6.2a. The polarizing beam splitters (PBS) define two orthogonal linearly–polarized arms (excitation and detection) each coupled to the microcavity via the same objective lens. A linear polarizer and a quarter–wave plate mounted on piezo–driven rotational stages compensate for small imperfections in the optics and enable a suppression of the excitation laser of 10^{-7} to be reached, stable

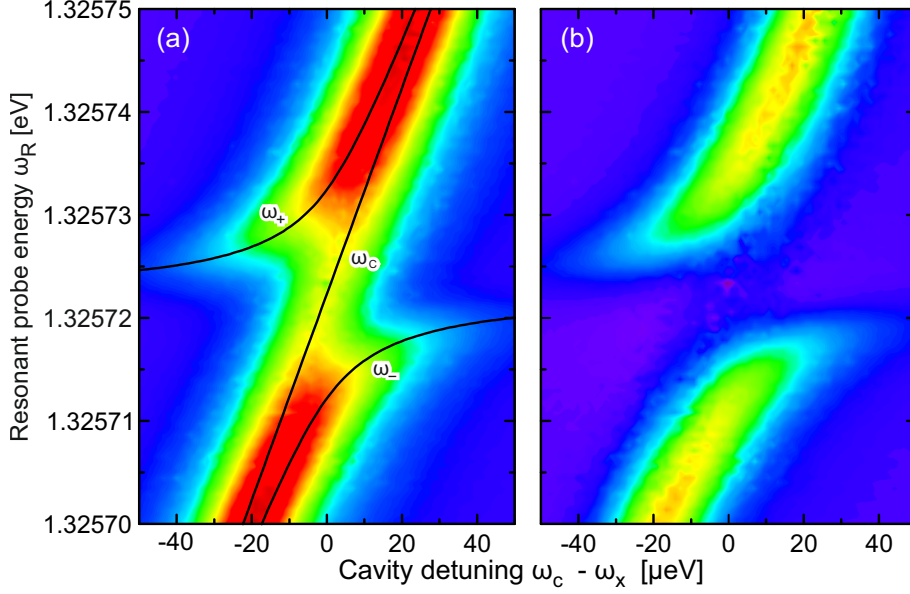


Figure 4.2. Dark-field resonant laser spectroscopy on a coupled quantum dot-cavity system for varying cavity detuning. (a) A triplet is observed at resonances $\omega_R = \omega_{\pm}, \omega_C$. We interpret the spurious (bare) cavity resonance ω_C as a consequence of an unstable emitter state resulting in telegraph-like dynamics. (b) The data in (a) after subtracting the bare cavity resonance revealing the normal mode splitting characteristic of the strong coupling regime.

over several days. The cavity exhibits non-degenerate linearly-polarized longitudinal modes with a splitting of about $200 \mu\text{eV}$, conveniently larger than the bandwidth required to probe fully the dynamics of the strong coupling. The cavity modes are aligned with respect to the polarization axis of the microscope at an angle $\phi \approx \pi/4$ allowing a good coupling of the cavity mode to both detection and excitation channels. We measure the wavelength of the tunable excitation laser with a wavemeter and use this information to calibrate the cavity detuning on applying a voltage to the microcavity z-piezo. While the polarization optics are all at room temperature, the microcavity setup is inserted into a stainless steel tube containing He exchange gas and cooled to 4 K in a He bath cryostat.

4.4 Experimental results

Tuning the microcavity resonance with respect to the emitter transition, and sweeping the excitation frequency with respect to the microcavity resonance, reveals the exact lineshape of the coupled emitter-cavity system for various detunings, as shown in figure 4.2a. We observe a triplet structure featuring the bare cavity resonance ω_C along

with two detuning–depending resonances identified as the polariton states of the strong coupling regime. The bare cavity contribution can be determined accurately from the data in the polariton gap at zero detuning. A subtraction of the bare cavity resonance from the raw data reveals the clear anticrossing of the polariton modes, figure 4.2b.

The anticrossing feature figure 4.2 is visible only if the sample is illuminated with an additional ultraweak non–resonant excitation laser ($\lambda = 830\text{ nm}$). In free space laser spectroscopy experiments on a sample from the same MBE, an “optical gating” by weak non–resonant excitation is described [23]. However, it is only partially successful: observation of the bare–cavity mode shows that the quantum dot detunes abruptly (and out of resonance with the microcavity) in a telegraph fashion. A bare–cavity contribution to resonance spectra has been observed also on photonic crystal cavities [13] and was attributed to charge noise in the vicinity of the quantum dot, a mechanism which is active here. The experiment integrates over a much longer timescale than is typical for this telegraph noise, thus capturing photons from the scattering off the bare cavity a significant fraction of time. We do not observe a fine structure splitting of the exciton at zero magnetic field. A neutral exciton without fine structure is unlikely for these quantum dots [24] so that we can safely assume that the studied exciton coupling to the cavity in figure 4.2 is a charged exciton.

4.5 Model

We model the experiment with the Jaynes–Cummings Hamiltonian modified for coherent excitation at frequency ω_R

$$\mathcal{H} = \hbar\omega_C a^\dagger a + \hbar\omega_X b^\dagger b + [\hbar g a^\dagger b + \hbar\epsilon a^\dagger e^{-i\omega_R t} + \text{h.c.}] , \quad (4.1)$$

Here, a (b) is the bosonic (fermionic) annihilation operator of the microcavity photon (exciton transition) with energy $\hbar\omega_C$ ($\hbar\omega_X$); g denotes the coherent coupling rate between photon and exciton; and ϵ is the effective coupling rate from the resonant excitation to the cavity field. Losses in the system are described by the Lindblad formalism including the photon energy loss rate κ and the exciton relaxation rate γ . The cavity emission is modeled to be weakly coupled to a continuum of detection modes with overall collection efficiency η : the detected count rate is thus $\dot{N} = \eta\kappa\langle a^\dagger a \rangle$.

With model M1 we investigate the system’s response as a function of the resonant probe frequency ω_R , treating ϵ as a perturbative parameter. The linear coupling gives rise

to two polariton modes (\pm) at Rabi frequencies ω_{\pm} . The steady-state cavity population (proportional to the photon count rate) evaluates to

$$\begin{aligned} \langle a^\dagger a \rangle(\omega_R) = & A_-^L \mathcal{L}(\omega_R - \omega_-) + A_+^L \mathcal{L}(\omega_R - \omega_+) \\ & + A^D \mathcal{D}(\omega_R - \omega_+) - A^D \mathcal{D}(\omega_R - \omega_-) , \end{aligned} \quad (4.2)$$

where $\mathcal{L}(\omega) = \text{Im}[(\pi\omega)^{-1}]$ is the unit-area Lorentzian function, $\mathcal{D}(\omega) = \text{Re}[(\pi\omega)^{-1}]$ its dispersive function counterpart, each with peak location $\text{Re } \omega = 0$ and FWHM parameter $2|\text{Im } \omega|$. The peak areas A_{\pm}^L , A^D and Rabi frequencies ω_{\pm} are closed form functions of the dynamical parameters $(g, \kappa, \gamma, \epsilon)$, see Appendix A.2.

4.6 Analysis

Figure 4.3 shows (black dots) two exemplary lineshapes, (a) for zero cavity-exciton detuning $\omega_C - \omega_X = 0 \mu\text{eV}$, and (b) for significant detuning $\omega_C - \omega_X = -17 \mu\text{eV}$. The purple solid line shows a best χ^2 fit of the observed counts to the model M1, eq. (4.2), where the fit results in a single set of dynamical parameters $(g, \kappa, \gamma, \epsilon)$, a set used for all employed detunings (table 4.1). The green and blue solid lines show the Lorentzian and dispersive constituents of the model, while the black dashed line represents the spurious bare-cavity contribution. The dynamical parameters obtained from the fit result in a cooperativity of $C = 2g^2/(\kappa\gamma) = 5.5 \pm 0.1$.

Qualitatively, the model M1 agrees well with the observed polariton resonances in terms of splitting, linewidths as well as their shift with cavity-exciton detuning. Quantitatively however, the count rates within the polariton gap are significantly underestimated with respect to the experimental data for all detunings. In the polariton gap, the model (neglecting of course the bare-cavity contribution) predicts a strong destructive interference: the positive Lorentzian contributions are reduced considerably by the two dispersive constituents, both of which turn negative. In the experiment, this interference is observed to a lesser degree than that predicted by model M1. This lack of interference is particularly prominent for large detunings at the exciton-like polariton resonance (figure 4.3b) and points strongly to an emitter dynamic not considered by the model.

To investigate this missing dynamic, we performed independent linewidth measurements on the same sample region but without the top mirror. The linewidths are measured under the same conditions, i.e. with resonant laser spectroscopy in the presence of an ultraweak non-resonant excitation (see Appendix A.5). The results demonstrate a

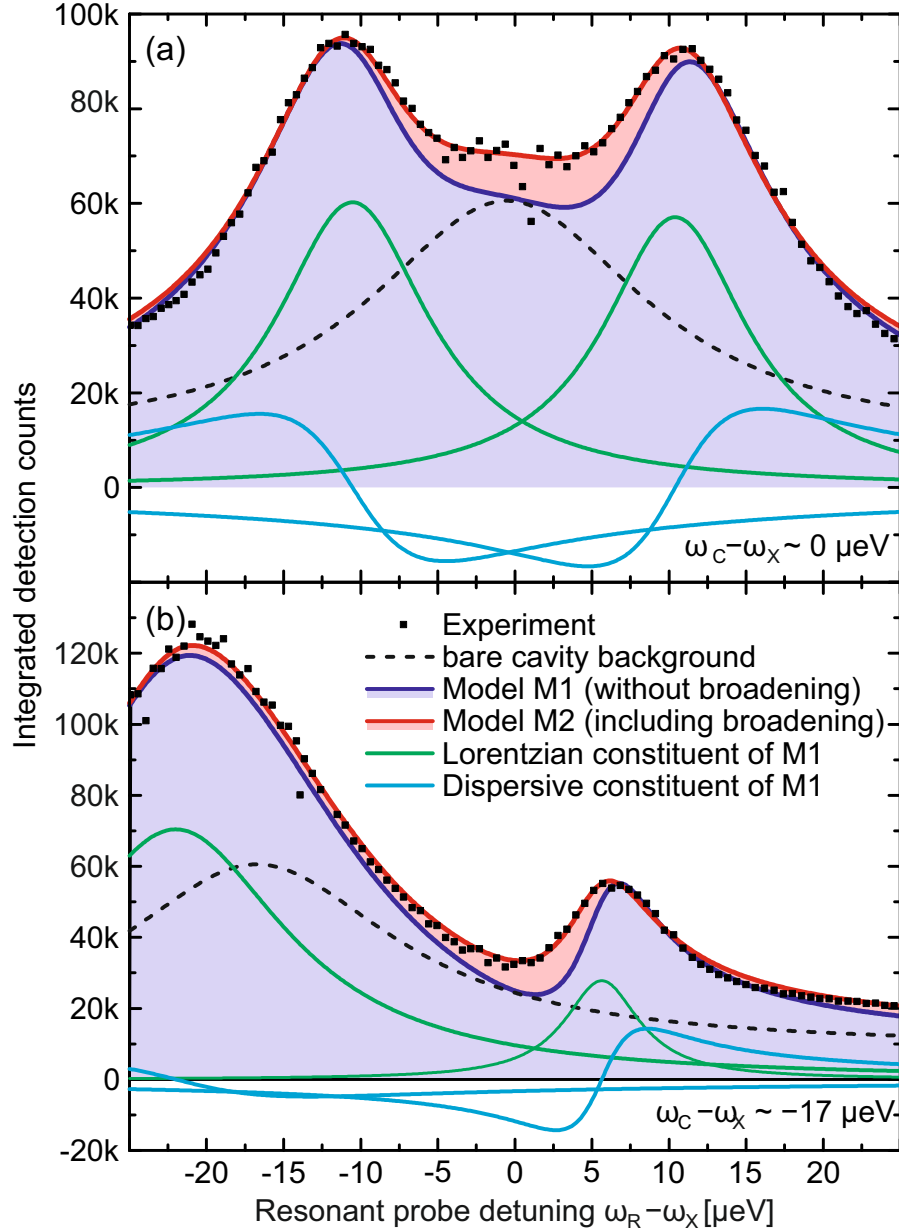


Figure 4.3. Dark-field laser spectroscopy: spectra for (a) zero and (b) $-17 \mu\text{eV}$ cavity-emitter detuning. The experimental values (black dots) are globally fitted to model M1 (purple solid line), with Lorentzian and dispersive constituents (green and blue solid line), and to model M2 (red solid line). M2, which includes an additional broadening mechanism of the emitter, describes the experimental data much better than M1. The improvement is partially masked by the bare cavity resonance background (black dashed line).

significant contribution to the exciton linewidth beyond that determined by spontaneous emission: typical linewidths are $3 - 4 \mu\text{eV}$; the radiative-lifetime limited linewidth (the

“transform limit”) corresponds to $0.8 \mu\text{eV}$. There are two culprits for this additional broadening: a spectral fluctuation (i.e. a wandering of the exciton central frequency on timescales longer than the radiative decay time) and pure exciton dephasing. The analysis (Table A.1) suggests spectral fluctuations are dominant, but the exact conclusion is quantum dot dependent. Linewidth broadening on this scale is commonly observed and arises from electric charge noise [25].

As a refinement to the previous model, we incorporate an emitter broadening by convoluting the emitter resonance ω_X with a Lorentzian distribution of free FWHM parameter Γ : this is model M2. The convolution gives an analytical result, eq. (A.15). A fit to the complete experimental data determines the dynamical parameters $(g, \kappa, \gamma, \epsilon, \Gamma)$, as shown in table 4.1. The model M2 results are shown in figure 4.3 as the red solid line. The reduced χ^2 is reduced by 25% but remains high (table 4.1) but nonetheless M2 offers a strong improvement in the interpretation of the experimental data. This is also demonstrated in figure 4.4: the parameters A_{\pm}^L , A^D and ω_{\pm} from eq. (4.2) are shown from both models M1 and M2 along with the experimental data. M2 significantly improves the FWHM parameters $2\text{Im}\omega_{\pm}$ and Lorentzian areas A_{\pm}^L at all cavity–exciton detuning ranges. Also, M2 resolves the discrepancy in the polariton gap in figure 4.3: M2 accounts perfectly for the experimental data both at zero detuning and at large negative detuning. Only M2 is consistent with the experimental data. The microcavity experiment is therefore sensitive to the emitter linewidth in a way that low–power laser spectroscopy alone is not. (We note that the microcavity experiment cannot distinguish easily between a spectral fluctuation and pure exciton dephasing: the M2 predictions are very similar, see discussion in Appendix A.3). The increase in emitter linewidth has a major effect on the cooperativity, table 4.1: M2 shows that emitter broadening alone reduces C from 9.0, the “bare” value, to 5.5.

4.7 Discussion

The dynamical parameters of the experiment are summarized in table 4.1. The freespace emitter lifetime of 800 ps corresponds to a transform–limited linewidth $\gamma = 0.8 \mu\text{eV}$ and an dipole moment $\mu_{12} = 1.2 \text{ e} \times \text{nm}$. The microcavity Q–factor $Q = 6 \times 10^4$ results in $\kappa = 22 \mu\text{eV}$. From a simulation of the microcavity, a vacuum electric field maximum of $E_{\text{vac}} \simeq 2 \times 10^4 \text{ V/m}$ is expected, yielding $g = \mu_{12} E_{\text{vac}} \simeq 24 \mu\text{eV}$. Experimentally, g is smaller than this best–case estimate. From model M1 a cooperativity of $C = 2g^2/(\kappa\gamma) = 5.5 \pm 0.1$, a result depending only weakly on the model assumptions.

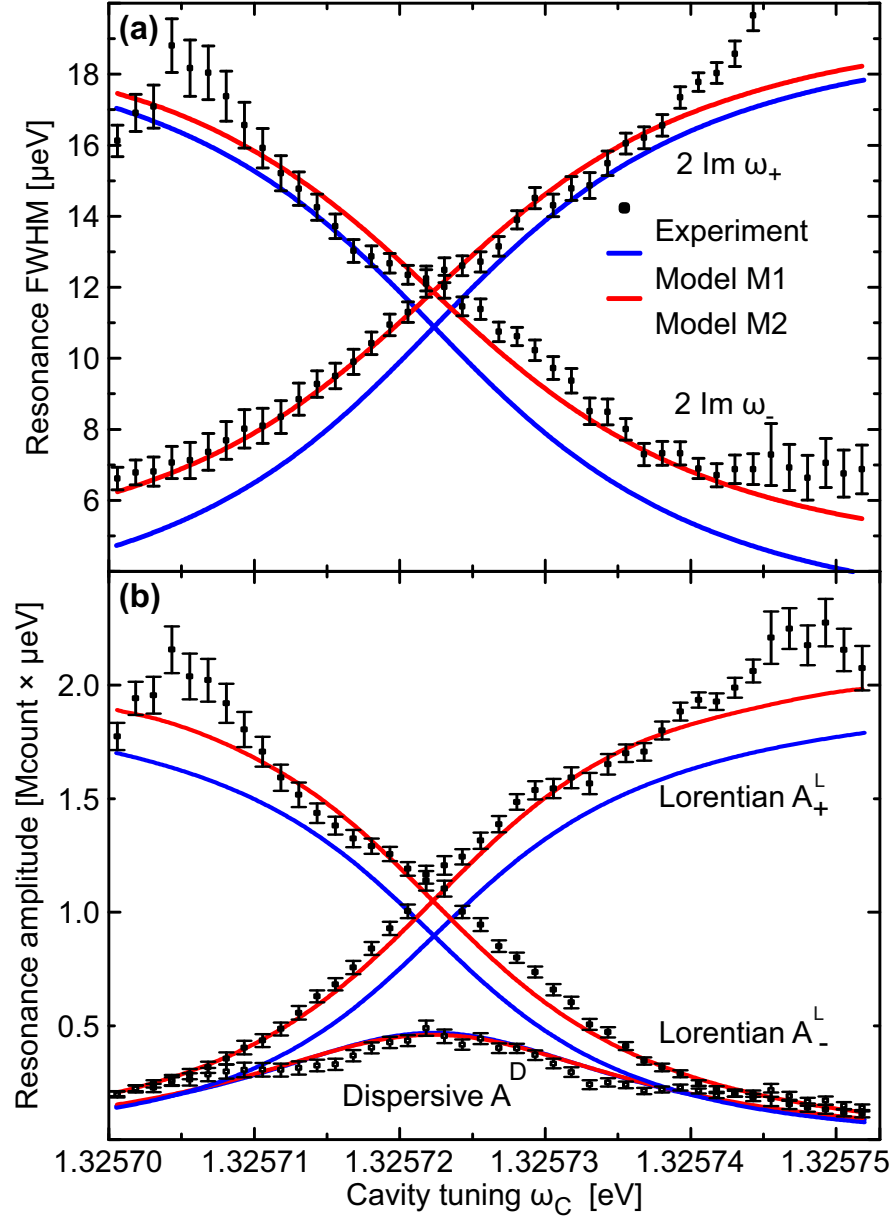


Figure 4.4. Comparison of model M1 and M2 with the experimental data over the whole cavity–emitter tuning range. (a) The polariton FWHM parameter ($2 \text{Im } \omega_{\pm}$) and (b) the Lorentzian/dispersive areas A_{\pm}^L , A^D versus cavity detuning. M2 provides a much better fit than M1.

An obvious route to higher cooperativity for the presented microcavity system is to improve the mirrors, i.e. to reduce the photon loss rate κ . Presently, the dielectric DBR is the limiting factor and this can be readily improved with “supermirror” coatings [26]. The coupling g should also be improved: presently, slight errors in the microcavity manufacture reduce g from its best-case value. Further, g would increase by a factor of

Table 4.1. Quantitative fit results of the dynamical parameters for models M1 (no emitter broadening) and for model M2 (with emitter broadening Γ).

Quantity	Unit	M1	M2
g	$\mu\text{eV}/\hbar$	11.05 ± 0.02	11.13 ± 0.02
κ	$\mu\text{eV}/\hbar$	19.48 ± 0.09	19.84 ± 0.09
γ	$\mu\text{eV}/\hbar$	2.28 ± 0.04	1.38 ± 0.04
Γ	$\mu\text{eV}/\hbar$	-	1.26 ± 0.05
$\eta\kappa t \epsilon ^2^*$	Mcount, $(\mu\text{eV}/\hbar)^2$	6.15 ± 0.04	7.08 ± 0.04
$C = 2g^2/(\kappa\gamma)$		5.5 ± 0.1	9.0 ± 0.3
reduced χ^2		123	94

* with integration time the overall collection efficiency of the cavity emission.

$\sqrt{2}$ (the cooperativity by a factor of 2) if the mode splitting in the fundamental cavity mode (presently $\approx 200 \mu\text{eV}$) could be eliminated. However, the point we wish to stress in this work is the equal importance of the emitter dynamics. If the additional broadening can be eliminated by improved emitter quality, the cooperativity can be increased from $C = 5.5$ to $C = 9.0$ even without an improvement in the microcavity. This is an entirely realistic proposition: approaches exist by which the additional broadening is routinely sub- μeV [27], in certain cases eliminated altogether [28], without telegraph-like noise by embedding the quantum dots in a vertical tunneling structure. Such a scheme is realistic in the cavity geometry by exploiting the good optical properties of epitaxial gates. The present experiment demonstrates that the use of such emitters will easily allow a cooperativity exceeding 10 to be achieved, a powerful route to the application of cavity-QED to quantum control in the solid-state.

We thank P. M. Petroff for provision of the semiconductor wafer; we acknowledge financial support from NCCR QSIT and from SNF project 200020_156637.

References

- [1] A. Boca, R. Miller, K. M. Birnbaum, A. D. Boozer, J. McKeever, and H. J. Kimble, [Physical Review Letters](#) **93**, 233603 (2004).
- [2] A. Imamoglu, D. D. Awschalom, G. Burkard, D. P. DiVincenzo, D. Loss, M. Sherwin, and A. Small, [Physical Review Letters](#) **83**, 4204 (1999).
- [3] H. J. Kimble, [Nature](#) **453**, 1023 (2008).
- [4] M. B. Plenio, S. F. Huelga, A. Beige, and P. L. Knight, [Physical Review A](#) **59**, 2468 (1999).
- [5] T. Wilk, S. C. Webster, A. Kuhn, and G. Rempe, [Science](#) **317**, 488 (2007).
- [6] K. M. Birnbaum, A. Boca, R. Miller, A. D. Boozer, T. E. Northup, and H. J. Kimble, [Nature](#) **436**, 87 (2005).
- [7] A. Reinhard, T. Volz, M. Winger, A. Badolato, K. J. Hennessy, E. L. Hu, and A. Imamoglu, [Nature Photonics](#) **6**, 93 (2012).
- [8] D. E. Chang, A. S. Sorensen, E. A. Demler, and M. D. Lukin, [Nature Physics](#) **3**, 807 (2007).
- [9] T. Volz, A. Reinhard, M. Winger, A. Badolato, K. J. Hennessy, E. L. Hu, and A. Imamoglu, [Nature Photonics](#) **6**, 605 (2012).
- [10] R. J. Warburton, [Nature Materials](#) **12**, 483 (2013).
- [11] J. Reithmaier, G. Sek, A. Löffler, C. Hofmann, S. Kuhn, S. Reitzenstein, L. Keldysh, V. Kulakovskii, T. Reinecke, and A. Forchel, [Nature](#) **432**, 197 (2004).
- [12] T. Yoshie, A. Scherer, J. Hendrickson, G. Khitrova, H. M. Gibbs, G. Rupper, C. Ell, O. B. Shchekin, and D. G. Deppe, [Nature](#) **432**, 200 (2004).
- [13] K. Hennessy, A. Badolato, M. Winger, D. Gerace, M. Atatüre, S. Gulde, S. Fält, E. L. Hu, and A. Imamoglu, [Nature](#) **445**, 896 (2007).
- [14] M. Lerner, N. Gregersen, F. Dunzer, S. Reitzenstein, S. Höfling, J. Mørk, L. Worschech, M. Kamp, and A. Forchel, [Physical Review Letters](#) **108**, 057402 (2012).

-
- [15] D. Englund, A. Faraon, I. Fushman, N. Stoltz, P. Petroff, and J. Vuckovic, *Nature* **450**, 857 (2007).
- [16] A. Badolato, K. Hennessy, M. Atatüre, J. Dreiser, E. Hu, P. M. Petroff, and A. Imamoglu, *Science* **308**, 1158 (2005).
- [17] A. Dousse, L. Lanco, J. Suffczyński, E. Semenova, A. Miard, A. Lemaître, I. Sagnes, C. Roblin, J. Bloch, and P. Senellart, *Physical Review Letters* **101**, 267404 (2008).
- [18] R. J. Barbour, P. A. Dalgarno, A. Curran, K. M. Nowak, H. J. Baker, D. R. Hall, N. G. Stoltz, P. M. Petroff, and R. J. Warburton, *Journal of Applied Physics* **110**, 053107 (2011).
- [19] L. Greuter, S. Starosielec, D. Najer, A. Ludwig, L. Duempelmann, D. Rohner, and R. J. Warburton, *Applied Physics Letters* **105**, 121105 (2014).
- [20] J. Miguel-Sánchez, A. Reinhard, E. Togan, T. Volz, A. Imamoglu, B. Besga, J. Reichel, and J. Estève, *New Journal of Physics* **15**, 045002 (2013).
- [21] D. Hunger, C. Deutsch, R. J. Barbour, R. J. Warburton, and J. Reichel, *AIP Advances* **2**, 012119 (2012).
- [22] A. V. Kuhlmann, J. Houel, D. Brunner, A. Ludwig, D. Reuter, A. D. Wieck, and R. J. Warburton, *Review of Scientific Instruments* **84**, 073905 (2013).
- [23] H. S. Nguyen, G. Sallen, C. Voisin, P. Roussignol, C. Diederichs, and G. Cassaboïs, *Physical Review Letters* **108**, 057401 (2012).
- [24] S. Seidl, B. D. Gerardot, P. A. Dalgarno, K. Kowalik, A. W. Holleitner, P. M. Petroff, K. Karrai, and R. J. Warburton, *Physica E* **40**, 2153 (2008).
- [25] J. Houel, A. V. Kuhlmann, L. Greuter, F. Xue, M. Poggio, B. D. Gerardot, P. A. Dalgarno, A. Badolato, P. M. Petroff, A. Ludwig, D. Reuter, A. D. Wieck, and R. J. Warburton, *Physical Review Letters* **108**, 107401 (2012).
- [26] G. Rempe, R. Lalezari, R. J. Thompson, and H. J. Kimble, *Optics Letters* **17**, 363 (1992).
- [27] A. V. Kuhlmann, J. Houel, A. Ludwig, L. Greuter, D. Reuter, A. D. Wieck, M. Poggio, and R. J. Warburton, *Nature Physics* **9**, 570 (2013).

- [28] A. V. Kuhlmann, J. H. Prechtel, J. Houel, A. Ludwig, D. Reuter, A. D. Wieck, and R. J. Warburton, [arXiv:1307.7109](#) (2013).

Chapter 5

Additional investigation of the strong coupling regime

5.1 Strong coupling in the magnetic field

We further study the QD–cavity coupling in a magnetic field of 3.00 T applied along the growth direction of the semiconductor sample. As argued in chapter 4, we assume here that we couple an X^{1-} to the microcavity, since we do not observe a fine structure splitting at zero magnetic field. In this case the ground state is split into the electronic spin states $|\uparrow\rangle$ and $|\downarrow\rangle$ by the Zeeman effect. Consequently, the X^{1-} trion, which consists of two spin-paired electrons and a hole spin is split into $|\uparrow\downarrow, \uparrow\rangle$ and $|\uparrow\downarrow, \downarrow\rangle$ by the hole Zeeman energy. Assuming a pure heavy-hole state, only the $|\uparrow\rangle \leftrightarrow |\uparrow\downarrow, \uparrow\rangle$ and $|\downarrow\rangle \leftrightarrow |\uparrow\downarrow, \downarrow\rangle$ transitions are allowed due to angular momentum conservation, where they couple to light with σ^+ or σ^- polarization respectively. Both transitions are coupled to the cavity. The transitions are separated by $\sim 300 \mu\text{eV}$ in energy corresponding to the typical values for the electron ($\sim -30 \mu\text{eV/T}$) and hole ($\sim 70 \mu\text{eV/T}$) Zeeman splitting [1].

As for the zero field, we measure the coupled QD–cavity system in a magnetic field with a cross-polarized detection scheme, where the cavity is tuned for different laser excitation frequencies. Figure 5.1a shows the higher energy $|\uparrow\rangle \leftrightarrow |\uparrow\downarrow, \uparrow\rangle$ transition coupled to the microcavity while the lower energy transition $|\downarrow\rangle \leftrightarrow |\uparrow\downarrow, \downarrow\rangle$ is shown in figure 5.1c. In both cases we observe a strong coupling signature. We note that, similar to zero field, a weak nonresonant excitation is required to observe strong coupling. Figures 5.1b and 5.1d show cross sections of the spectra at zero cavity–QD detuning and at a negative detuning. The spectra are globally analyzed with the same models as described above. The red curves correspond to fits of the model that includes a broadening of the emitter

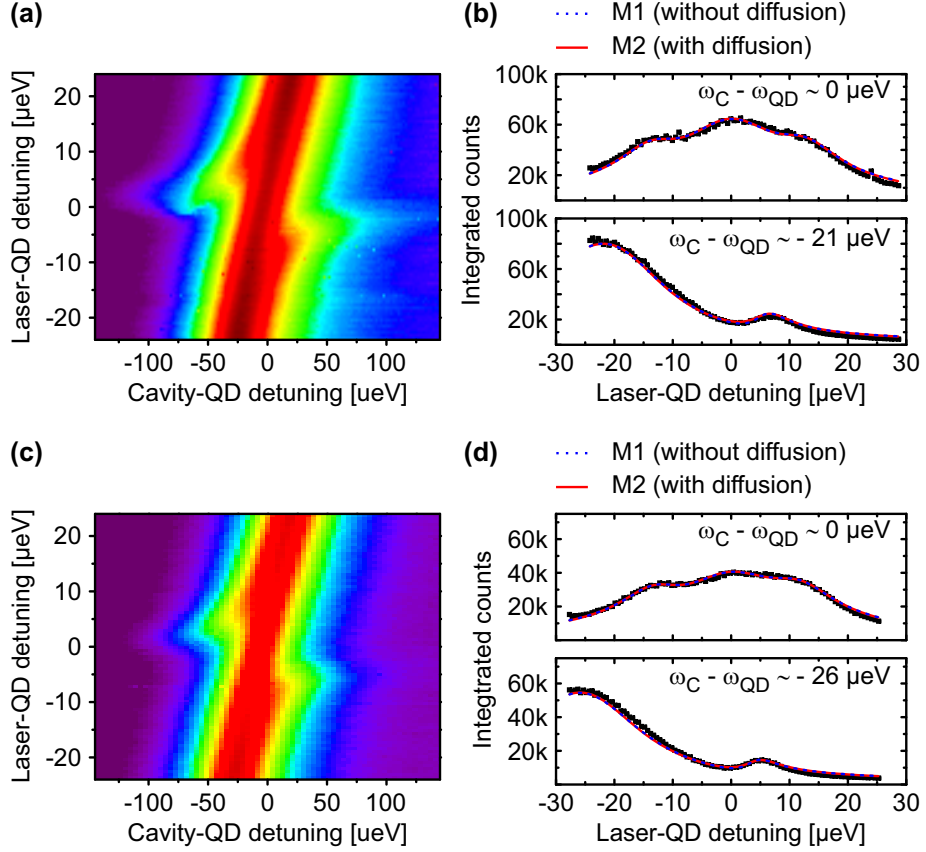


Figure 5.1. Strong coupling in a magnetic field of 3.00 T. Coupling of the $|\uparrow\rangle \leftrightarrow |\uparrow\downarrow, \uparrow\rangle$ transition is shown in (a) and (b), where the $|\downarrow\rangle \leftrightarrow |\uparrow\downarrow, \downarrow\rangle$ transition is shown in (c) and (d). (a) and (c) illustrate the dark-field resonant laser spectroscopy, where the microcavity is tuned for different laser-excitation frequencies. (b) and (d): cross-sections of the spectra at zero detuning (top) and negatively detuned (bottom). The red (blue dashed) curves show a fit of the JC model, which includes (neglects) a correction for spectral diffusion. The fit parameters are listed in table 5.1 and 5.2.

due to spectral diffusion (Γ), which is neglected in the blue curves. The values obtained from the fits are summarized in table 5.1 for the $|\uparrow\rangle \leftrightarrow |\uparrow\downarrow, \uparrow\rangle$ transition and in table 5.2 for the $|\downarrow\rangle \leftrightarrow |\uparrow\downarrow, \downarrow\rangle$ transition.

For both transitions the fits result in a higher coupling rate g for a broader cavity decay rate κ . In the $|\uparrow\rangle \leftrightarrow |\uparrow\downarrow, \uparrow\rangle$ transition the emitter rate γ and diffusion Γ are in accordance with the values obtained at zero magnetic field resulting in comparable cooperativity values (compare table 5.1 with table 4.1). However, for the $|\downarrow\rangle \leftrightarrow |\uparrow\downarrow, \downarrow\rangle$ transition a lower cooperativity is achieved, due to the higher QD and cavity decay rate obtained from the fit (table 5.2).

From this data we cannot identify a magnetic field dependence on the QD diffusion Γ . We further note that for the measurements at a magnetic field of 3.00T, it is not evident

Table 5.1. Quantitative fit results of the dynamical parameters for the $|\uparrow\rangle \leftrightarrow |\uparrow\downarrow, \uparrow\rangle$ transition at $3.00T$.

 M1: model with no emitter broadening; M2: model with emitter broadening (Γ).

Quantity	Unit	M1	M2
g	$\mu eV/\hbar$	13.47 ± 0.03	13.57 ± 0.03
κ	$\mu eV/\hbar$	23.22 ± 0.05	22.38 ± 0.07
γ	$\mu eV/\hbar$	2.63 ± 0.06	1.68 ± 0.06
Γ	$\mu eV/\hbar$	-	1.31 ± 0.08
$C = 2g^2/(\kappa\gamma)$		5.9 ± 0.2	9.8 ± 0.4

Table 5.2. Quantitative fit results of the dynamical parameters for the $|\downarrow\rangle \leftrightarrow |\uparrow\downarrow, \downarrow\rangle$ transition at $3.00T$.

 M1: model with no emitter broadening; M2: model with emitter broadening (Γ).

Quantity	Unit	M1	M2
g	$\mu eV/\hbar$	12.70 ± 0.05	12.76 ± 0.03
κ	$\mu eV/\hbar$	23.61 ± 0.08	23.04 ± 0.11
γ	$\mu eV/\hbar$	3.33 ± 0.09	2.71 ± 0.11
Γ	$\mu eV/\hbar$	-	0.86 ± 0.11
$C = 2g^2/(\kappa\gamma)$		4.1 ± 0.2	5.2 ± 0.3

that the model which includes the spectral diffusion represents the data more accurately than a model without them. We argue that this is due to the fact that here the bare cavity contribution dominates the spectra as illustrated in figure 5.2. Therefore, the correction by the spectral diffusion in the model only has a limited effect, since it only alters the signature of the coupled QD, whereas the signature of the bare cavity itself is not affected by the broadening of the QD.

We speculate on the origin of the bare cavity contribution by comparing the relative intensities of the bare cavity–mode (green curves in figure 5.2) to the intensity of the polariton signatures (blue curves in figure 5.2) at zero (figure 5.2a) and at a magnetic field of $3.00T$ (figure 5.2b and c). The two contributions make up the overall model (red curves in figure 5.2), where spectral diffusion was taken into account.

Presumably, the bare cavity contribution arises due to a QD state which does not couple to the cavity mode and hence the empty cavity is probed by the crosspolarized detection. Generally, this might be due to the fact that the charge required for an X^{-1} tunnels in and out of the dot. We compare the area of the bare cavity contribution (green curves) and the polariton signal (blue curves). At zero magnetic field (figure 5.2a) we

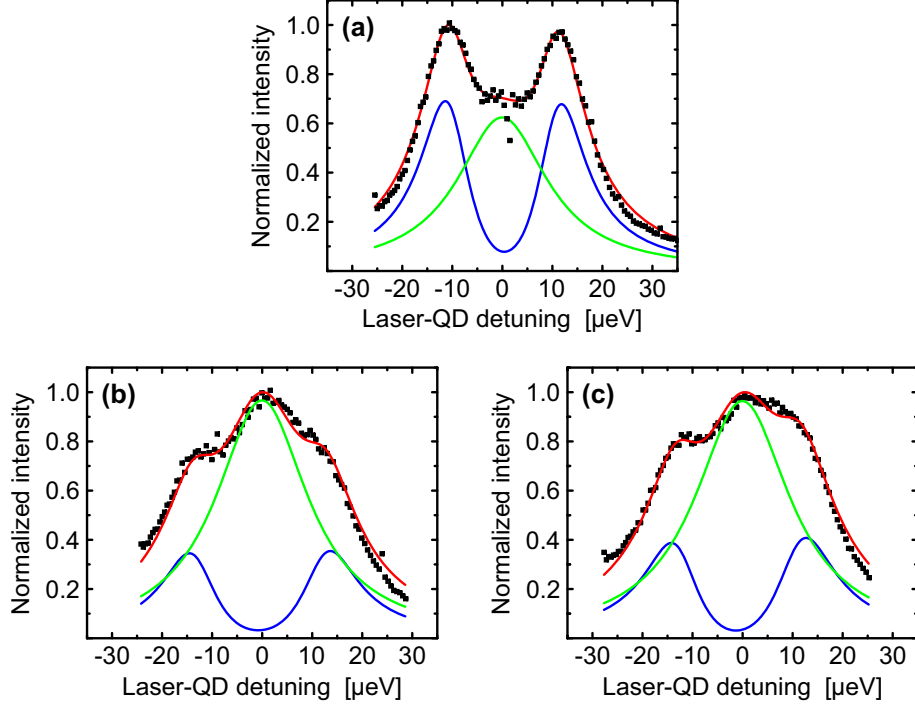


Figure 5.2. Intensity for different laser-QD detuning, when the QD is in resonance with the micro-cavity, normalized for the maximum signal. The data are fitted with the model M2 (red), which includes spectral diffusion and is composed of a bare cavity contribution (green) and a polariton contribution (blue). (a) At zero field, the polariton and bare cavity contribution are approximately the same. While for both transitions at 3.00 T ($|\uparrow\rangle \leftrightarrow |\uparrow\downarrow, \uparrow\rangle$ in (b) and $|\downarrow\rangle \leftrightarrow |\uparrow\downarrow, \downarrow\rangle$ in (c)) the bare cavity intensity exceeds the polariton intensity approximately by a factor of 3.

find a bare cavity : polariton signal ratio of 1 : 1.16 and argue that the dot spends approximately the same amount of time in a charged and in an empty state. In a magnetic field (figure 5.2b and c), the quantum dot is still in an uncharged state half of the time. Furthermore, the electron spin states are split by the Zeeman energy, where only one of the spin states can couple to the cavity mode for a certain detuning. We assume that both spin states are equally likely to be occupied and overall the QD spends in total 1/4 of the time in a state where it couples to the cavity. Therefore, it is expected that in 3/4 of the time the bare cavity is probed by the laser. This argumentation corresponds well with the observed intensities for the two transitions at a magnetic field of 3.00 (figure 5.2b and c). We find a bare cavity : polariton ratio of 2.57 : 1 for the $|\uparrow\rangle \leftrightarrow |\uparrow\downarrow, \uparrow\rangle$ transition (figure 5.2b) and a ratio of 2.26 : 1 for the $|\downarrow\rangle \leftrightarrow |\uparrow\downarrow, \downarrow\rangle$ transition (figure 5.2c).

At this point, we briefly discuss the possibility of spin pumping, which has already been observed for electron [2] and hole spins [3]. Here, a spin state is shelved such

that it is not accessible to the excitation any more. This spin-shelved state lives for a relatively long time, when the tunneling rate in and out of the QD is suppressed by an applied electric field [2]. Following the above argumentation with the observed intensity ratios, we note that here the QD is in a regime where its charge state fluctuates and spin shelving is inefficient.

5.2 Dynamics of the strong coupling regime

In addition to the spectral experiments, we attempt to describe the strong coupling regime in the time domain at zero magnetic field. Here, the dynamics are governed by the back action of the cavity on the QD, where an emitted photon can be reabsorbed before it is lost. We first derive the probability of the photon being in the cavity at a time t after excitation, which corresponds directly to the probability of detecting a photon since we couple to the cavity mode in the measurement. For simplicity, we assume that the system is deep in the strong coupling regime and neglect QD dephasing and spectral diffusion in the derivation. Cavity-QD detuning lifetime measurements then aim to reveal the time dependent nature of the strongly coupled system.

5.2.1 Interaction of the QD with the cavity in the time domain

The Jaynes-Cummings (JC) Hamiltonian in the absence of a weak external excitation reads:

$$\mathcal{H} = \hbar\omega_C a^\dagger a + \hbar\omega_X b^\dagger b + \hbar g (a^\dagger b + b^\dagger a) \quad (5.1)$$

where a and b denote the annihilation operators of the cavity (C) and the exciton (X) respectively. In the strong coupling regime, the coupled cavity-QD state can be described as a superposition of the QD in the excited state and cavity in the empty state $|e, 0\rangle$ with the QD in the ground state and a photon in the cavity mode $|g_s, 1\rangle$:

$$|\Psi(t)\rangle = c_{e,0}(t) |e, 0\rangle + c_{g_s,1}(t) |g_s, 1\rangle. \quad (5.2)$$

Solving the time dependent Schrödinger equation $i\hbar \frac{d}{dt} |\Psi(t)\rangle = \mathcal{H} |\Psi(t)\rangle$, we obtain the time dependent coefficients $c_{e,0}(t)$ and $c_{g_s,1}(t)$:

$$c_{e,0}(t) = c_{e,0}(0) \cos gt - ic_{g_s,1}(0) \sin gt, \quad (5.3a)$$

$$c_{g_s,1}(t) = c_{g_s,1}(0) \cos gt - ic_{e,0}(0) \sin gt. \quad (5.3b)$$

Here the QD is initially in the excited state (i.e.: $c_{e,0}(0) = 1$ and $c_{gs,0}(0) = 0$). The probability of finding the photon in the cavity after a time t is then given by [4]:

$$p_e(t) = |\langle g_s, 1 | \Psi(t) \rangle|^2 = \frac{1}{2} (1 - \cos 2gt). \quad (5.4)$$

From equation 5.4 it is evident that the system coherently oscillates back and forth between the cavity and the exciton at a frequency corresponding to twice the coupling rate $2g$. So far the incoherent decay, stemming from the cavity (κ) and from the QD (γ) is not considered. For $g \gg \kappa, \gamma$, the oscillations derived in equation 5.4 are damped with an averaged rate since the system oscillates between QD and cavity [5]. The probability to detect a photon is then given by:

$$p'_e(t) = \frac{1}{2} (1 - 2 \cos gt) e^{-\frac{\kappa+\gamma}{2}t}. \quad (5.5)$$

This equation exposes the difference in the dynamics of the strong coupling regime compared to the weak coupling regime. In the weak coupling regime, the coupled QD decays exponentially [6] with a rate that is enhanced by the Purcell factor F_p compared to the free space decay rate. However, in the strong coupling regime, the QD population undergoes coherent oscillations that are damped exponentially with a rate $(\kappa + \gamma)/2$. This backaction of the cavity on the QD leads to non-Markovian dynamics as has already been observed for QDs coupled to micropillars [7].

Furthermore, in the case of weak coupling, the Purcell factor is proportional to the enhanced photon density of states in the cavity. Therefore the detuning dependent decay rate exhibits a Lorentzian lineshape according to the cavity mode. We note that the decay rates can also be described by evaluating the imaginary part of the eigenvalues of the JC-model (equation 1.13). As a consequence a non Lorentzian lineshape is obtained in the strong coupling regime, where the maximum decay rate is $(\kappa + \gamma)/2$ at zero detuning.

5.2.2 Lifetime measurements

Here, we study the dynamics of the strongly coupled cavity-QD system by performing lifetime measurements for different cavity-QD detunings. We excite the QD nonresonantly with a Q-switched pulsed laser diode emitting at $\lambda = 830$ nm with a repetition rate of 80 MHz and a pulse width of 50 ps. The excitation pulse defines the start signal and the stop signal is provided by an avalanche photodiode (APD) with a 340 ps timing

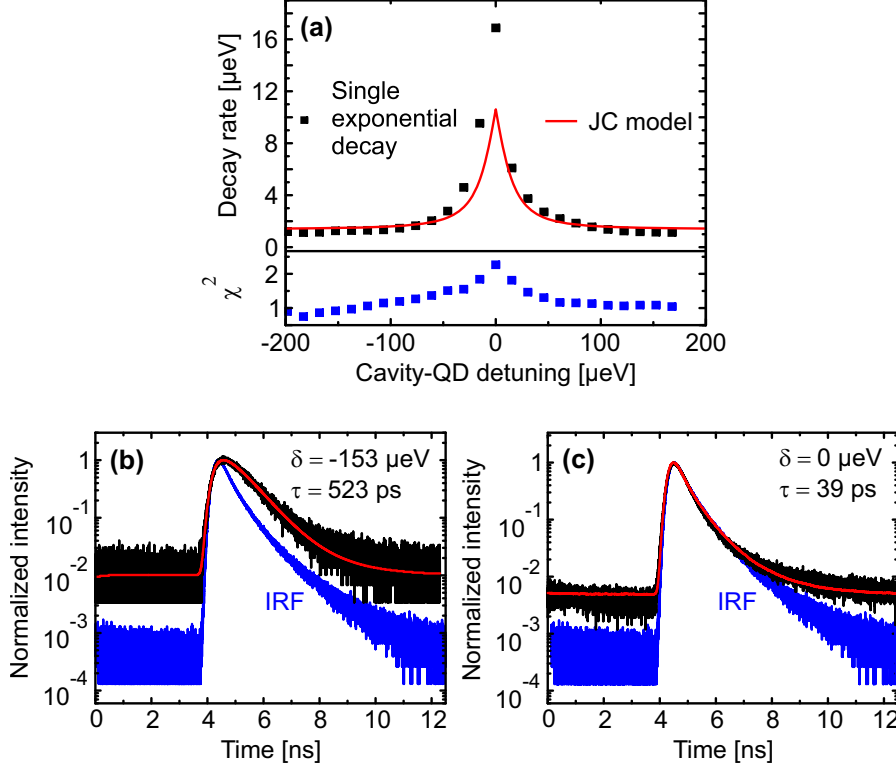


Figure 5.3. Lifetime measurements in the strong coupling regime. (a) The decay rates obtained by a single exponential fit are plotted as a function of detuning. The corresponding reduced χ^2 , which quantify the quality of the fits are shown in blue. A strong deviation from the ideal value of 1 is obtained for zero cavity-QD detuning. The red curve shows the expected decay rates from the JC-model with $\hbar\kappa = 19.84 \mu\text{eV}$, $\hbar\gamma = 1.38 \mu\text{eV}$ and $\hbar g = 11.13 \mu\text{eV}$. (b) Decay curve measured when the microcavity is $-153 \mu\text{eV}$ detuned from the resonance. A single exponential lifetime of 523 ps is obtained accompanied by a χ^2 of 0.918. (c) For zero detuning the decay follows almost the IRF, which indicates that the underlying cavity-QD dynamics are too fast to be observed.

resolution and a darkcount rate of 20 counts per second.

Figure 5.3b shows a normalized decay curve in black where the cavity is $-153 \mu\text{eV}$ detuned from the QD transition. A single exponential fit (red) that takes the internal response function (IRF) (shown in blue) into account yields a lifetime of 523 ps with a reduced χ^2 of 0.918. When the cavity is tuned into resonance with the QD (figure 5.3c), the lifetime is reduced but we do not resolve any oscillatory behavior as expected from equation 5.5. This is because the involved timescales are too fast to be observed: the rates obtained by the fit at zero field in chapter 4 ($\hbar\kappa = 19.84 \mu\text{eV}$, $\hbar\gamma = 1.38 \mu\text{eV}$ and $\hbar g = 11.13 \mu\text{eV}$) translate into an oscillation and decay timescale of $\sim 60 \text{ ps}$, which is significantly smaller than the temporal width of the IRF ($\sim 600 \text{ ps}$). Moreover, we measure a decay that coincides closely with the IRF in figure 5.3c. A single exponential

fit reveals a lifetime of 39 ps accompanied by a relatively high reduced χ^2 of 2.265, which indicates that here the fit routine fails to describe the cavity-QD dynamics. This is consistent with the model as a single exponential decay is not expected.

The decay rates obtained from the single exponential fits are plotted in figure 5.3a as a function of cavity-QD detuning (black) accompanied by the reduced χ^2 values (blue). For comparison, the decay rates expected from the JC model (two times the imaginary part of equation 1.13) are plotted in red using the rates obtained from the model fit: $\hbar\kappa = 19.84 \mu\text{eV}$, $\hbar\gamma = 1.38 \mu\text{eV}$ and $\hbar g = 11.13 \mu\text{eV}$. The decay qualitatively follows the JC model. However, for small detuning our broad IRF does not allow us to resolve the dynamics of the strongly coupled QD-cavity system and the single exponential fit routine overestimates the decay. We note generally that the direct observation of the coherent oscillations described by equation 5.5 in cavity-QD systems is very demanding with the available infrastructure due mainly to the limited time resolution of the APDs. A possibility to circumvent this limit is the use of a pump-probe measurement, demonstrated for e.g. quantum wells coupled to a semiconductor microcavity [8].

References

- [1] R. J. Warburton, [Nature Materials](#) **12**, 483 (2013).
- [2] M. Kroner, K. M. Weiss, B. Biedermann, S. Seidl, A. W. Holleitner, A. Badolato, P. M. Petroff, P. Öhberg, R. J. Warburton, and K. Karrai, [Physical Review B](#) **78**, 075429 (2008).
- [3] B. D. Gerardot, D. Brunner, P. A. Dalgarno, P. Ohberg, S. Seidl, M. Kroner, K. Karrai, N. G. Stoltz, P. M. Petroff, and R. J. Warburton, [Nature](#) **451**, 441 (2008).
- [4] D. F. Walls and G. J. Milburn, *Quantum Optics* (Springer Science & Business Media, 2007).
- [5] H. J. Carmichael, R. J. Brecha, M. G. Raizen, H. J. Kimble, and P. R. Rice, [Physical Review A](#) **40**, 5516 (1989).
- [6] P. Lodahl, S. Mahmoodian, and S. Stobbe, [Reviews of Modern Physics](#) **87**, 347 (2015).
- [7] K. H. Madsen, S. Ates, T. Lund-Hansen, A. Löffler, S. Reitzenstein, A. Forchel, and P. Lodahl, [Physical Review Letters](#) **106**, 233601 (2011).
- [8] T. B. Norris, J.-K. Rhee, C.-Y. Sung, Y. Arakawa, M. Nishioka, and C. Weisbuch, [Physical Review B](#) **50**, 14663 (1994).

Chapter 6

Epitaxial lift-off for solid-state cavity quantum electrodynamics

Adapted from:

Lukas Greuter, Daniel Najer, Andreas V. Kuhlmann, Sebastian Starosielec, Sascha R. Valentin, Arne Ludwig, Andreas D. Wieck and Richard J. Warburton,
“Epitaxial lift-off for solid-state cavity quantum electrodynamics”,
Submitted, [arXiv:1505.00658](https://arxiv.org/abs/1505.00658) (2015).

We demonstrate an approach to incorporate self-assembled quantum dots into a Fabry-Pérot-like microcavity. Thereby a $3\lambda/4$ GaAs layer containing quantum dots is epitaxially removed and attached by van der Waals bonding to one of the microcavity mirrors. We reach a finesse as high as 4,100 with this configuration limited by the reflectivity of the dielectric mirrors and not by scattering at the semiconductor-mirror interface, demonstrating that the epitaxial lift-off procedure is a promising procedure for cavity quantum electrodynamics in the solid state. As a first step in this direction, we demonstrate a clear cavity-quantum dot interaction in the weak coupling regime with a Purcell factor in the order of 3. Estimations of the coupling strength via the Purcell factor suggests that we are close to the strong coupling regime.

6.1 Introduction

The interaction of optically active semiconducting nanostructures such as quantum dots (QDs) with light can be massively increased by placing the emitter into a microcavity, thereby allowing a study of cavity quantum electrodynamics (CQED) in the solid state. A measure of the cavity-emitter interaction is the cooperativity parameter, $C = 2g^2/\kappa\gamma$, which puts all involved rates in context: the emitter-cavity coupling rate g , the cavity photon decay rate κ and the effective total emitter dephasing rate $\gamma/2$. If $g \ll \kappa, \gamma$, the system is in the weak coupling regime and an emitted photon is irreversibly lost before it can be reabsorbed. However, the increased photon density of states associated with the cavity mode results in an accelerated spontaneous emission when the QD and cavity are in resonance [1]. This enhancement of the spontaneous emission increases the quantum efficiency of single photon sources [2, 3], an important feature for many applications in quantum information [4]. If $g \gg \kappa, \gamma$, the system is in the strong coupling regime and an energy quantum is coherently and reversibly exchanged between emitter and cavity mode resulting in new eigenstates, polaritons i.e. superpositions of cavity photon and emitter excitation. Strong coupling is the prerequisite for the realization of a single photon transistor [5] and enables QD-QD coupling with potential applications in quantum information [6]. Both regimes were already observed with self-assembled QDs in micropillars [7–9] and photonic crystals [10–13]. Alternative experiments with QDs coupled to fully tunable microcavities showed a clear Purcell enhancement [14–16] and even allowed the observation of strong coupling [17].

The threshold to observe a finite splitting in polariton energy is given by $4g > |\kappa - \gamma|$ from the Jaynes-Cummings Hamiltonian that describes the coupled system [18]. For high quality material at low temperature, γ is typically much smaller than κ : the main goal is to increase g and decrease κ by choosing an appropriate cavity design. The cavity decay rate κ is limited by the reflectivity of the mirrors and characterized by the quality factor $Q = \omega/\kappa$, where ω is the resonance angular frequency of the cavity. The coupling strength g is given by $\hbar g = \mu_{12}E_{\text{vac}}$, where μ_{12} is the emitter's dipole moment and the vacuum field $E_{\text{vac}} \propto 1/\sqrt{V_0}$ scales inversely with the square root of the cavity mode volume V_0 . Thus, efforts to achieve a strong QD-cavity coupling seek to decrease the mode volume at high cavity Q -factors.

Generally, for QDs coupled to micropillars or photonic crystal cavity modes, the benefit of a small mode volume comes at the cost of the Q -factor. Furthermore, spectral and spatial tunability remains limited in these cavities. An alternative is to employ a

tunable cavity design [19–22]. So far, experiments in a tunable cavity incorporate the InGaAs QDs in a heterostructure which also contains a semiconductor distributed Bragg reflector (DBR) consisting of several pairs of AlGaAs/GaAs [14–17]. These two materials have the same lattice constant but a different refractive index ($n_{\text{AlGaAs}} = 3.009$, $n_{\text{GaAs}} = 3.54$). There are three issues here. First, this material combination (equal lattice constant but significantly different refractive index) is unique to GaAs, unfortunately limiting DBR-based CQED applications with QDs to self-assembled InGaAs QDs. Second, the relatively low refractive index contrast results in a high penetration depth of the cavity field into the mirror thus enlarging the mode volume. Finally, semiconductor ‘supermirrors’ are essentially impossible to fabricate: growth of more than, say, 40 pairs is extremely time consuming.

We present here a best-of-both-worlds approach for CQED: it combines the benefits of a solid state emitter with a low-loss high-reflectivity dielectric DBR. The tantalizing possibility is to embed a fast, robust solid-state emitter in a low mode volume microcavity formed using dielectric supermirrors. We remove epitaxially a thin GaAs layer containing InGaAs QDs and bond the layer via van der Waals (VdW) forces to a dielectric DBR. This forms one of the end mirrors in the Fabry–Pérot-like tunable microcavity. The InGaAs QD is a suitable candidate, partly due to its relative short recombination time (i.e. large oscillator strength [23]). Dielectric mirrors enable an ultrahigh finesse (up to 10^6 [24]) with also a small penetration depth. We note that the approach shown here enhances greatly the flexibility of cavity experiments: each part of the cavity (bottom mirror, top mirror, optically active layer) can be individually designed and processed and then combined to create an optimized CQED system.

We demonstrate a successful epitaxial lift-off (ELO) and subsequent attachment to a dielectric DBR by van der Waals bonding. The mirror is then integrated into the tunable cavity design and we show that the finesse of the cavity remains high despite the presence of the new GaAs–DBR interface. Furthermore, we show a weak coupling of a single QD to the microcavity mode as revealed by a reduction of the lifetime when the QD is in resonance with the cavity. In fact an estimation of the coupling g implies that our system is close to the strong coupling regime and we state that by minor improvements the observation of the typical anticrossing is within reach in this system.

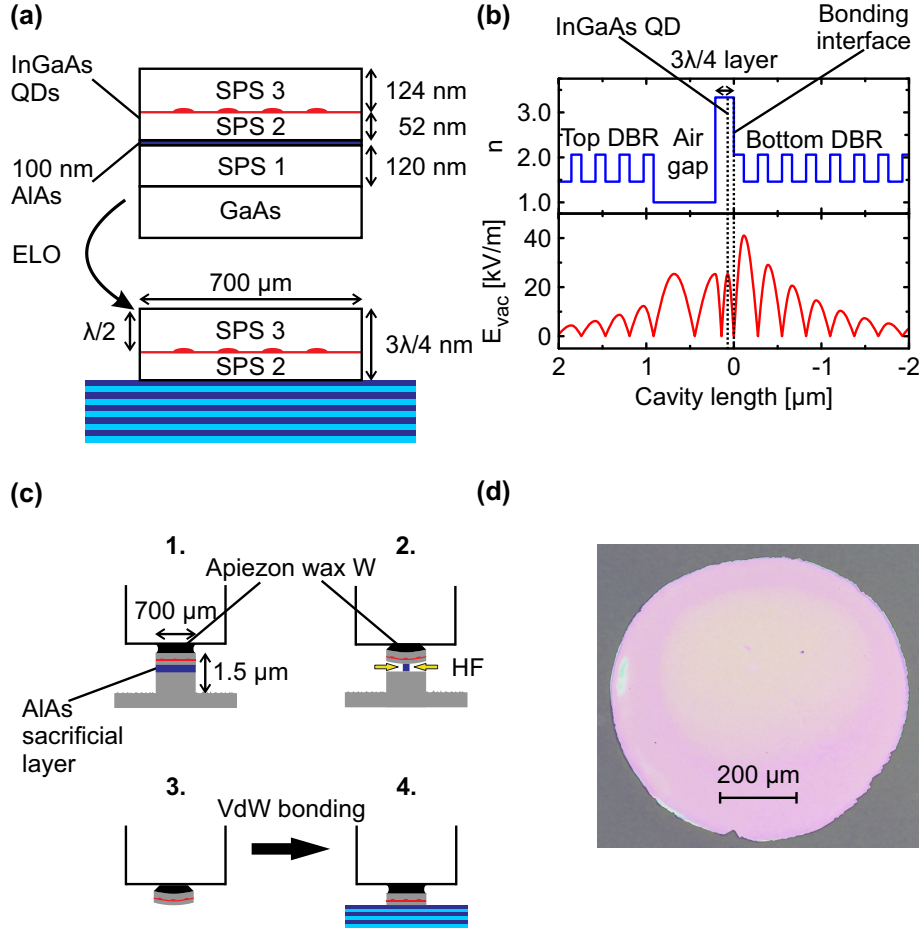


Figure 6.1. Epitaxial lift-off (ELO) procedure for cavity QED with QDs. (a) Sample structure before (top) and after (bottom) the ELO process. (b) 1D transfer matrix method simulation of the microcavity design with the bonded ELO layer. The design is chosen such that a field node is located at the bonding interface. (c) The fabrication consists mainly of the following steps: 1. Mesa-etching and attachment to an acid-resistant teflon stamp; 2. etching of the sacrificial AlAs layer in 10% HF until the GaAs substrate falls away; and 3. and 4. bonding to a dielectric DBR. (d) Optical microscope image of a $3\lambda/4$ thick GaAs layer bonded to a dielectric DBR after ultrasonic bath cleaning.

6.2 Sample

In the present proof of concept experiment, we bond a $3\lambda/4$ epitaxial layer that embeds the QDs onto a $\text{Ta}_2\text{O}_5/\text{SiO}_2$ DBR ending with the high refractive index material (Ta_2O_5). This serves as one mirror in the tunable cavity, while the other consists of a DBR ending with a Ta_2O_5 layer as well. A 1D transfer matrix method simulation of the vacuum field for this particular cavity design is shown in figure 6.1b. By design, an electric field node is located at the GaAs epilayer-mirror interface with the hope that fabrication imperfections may have only a limited effect on the finesse. This is a conservative

approach: the penetration depth into the bottom mirror could be further reduced by bonding a λ layer on a DBR ending with SiO_2 , but with the drawback of a field antinode at the interface.

6.2.1 Epitaxial lif-off

The sample before (after) the epitaxial lift-off is shown in figure 6.1a, top (bottom). The heterostructure is grown by molecular beam epitaxy (MBE) on a GaAs substrate followed by a 225 nm thick GaAs layer that includes a 120 nm thick short period superlattice (SPS₁) with composition GaAs(2 nm)/ Al_{0.33}Ga_{0.67}As(2 nm) for stress relief. On top of the SPS₁ a 100 nm thick AlAs layer is grown as sacrificial layer followed by the ELO layer with a total thickness of $3\lambda/4$ for a design wavelength of $\lambda = 940$ nm. The ELO layer contains the InGaAs QDs grown at a distance $\lambda/2$ from the surface such that they are located at an antinode of the vacuum field in order to maximize the coupling to the cavity (figure 6.1b). The QDs are surrounded by SPS₂ and SPS₃ each of composition GaAs(1 nm)/Al_{0.33}Ga_{0.67}As(3 nm). SPS₂ also serves as a stress relief for the following QD wetting layer, while SPS₃ enhances carrier recombination within the QDs. Both SPS show a lower average refractive index of the complete ELO layer $n = 3.332$.

Figure 6.1c shows the process of the epitaxial lift-off procedure and the subsequent van der Waals bonding. For the separation of the ELO-film, we first deposit a small piece of Apiezon wax on the sample and heat it to 125 °C for 1 hour. The melted wax defines a round structure with diameter of $\approx 700 \mu\text{m}$ for etching a mesa with a solution consisting of sulfuric acid (H_2SO_4), hydrogen peroxide (H_2O_2) and deionized water (H_2O) with a volume ratio of 1:8:120, commonly known as piranha-solution. We first etch $\approx 1.5 \mu\text{m}$ with the piranha solution such that the AlAs sacrificial layer is exposed for the subsequent etching with hydrofluoric acid (HF). The piranha-etched sample with the wax is then reheated to 70 – 80 °C and attached to a homemade teflon stamp before immersed into the 10 % HF solution (step 1. and 2. in figure 6.1c). The epitaxial lift-off is based on the high selectivity ($10^8 : 1$) on etching AlAs in GaAs in a 10 % HF-solution. During the etching process with HF, the stress induced by the surface tension of the wax bows the epitaxial layer and ensures an open etching channel [25, 26].

6.2.2 Van der Waals bonding

After the AlAs sacrificial layer is completely etched, the substrate falls away and the ELO-film stays attached to the teflon stamp (3. in figure 6.1c). The HF-solution is then

highly diluted ($\ll 0.001\%$) by rinsing with deionized water before the new host substrate is immersed into the liquid. The host substrate consists of silica coated with a distributed Bragg reflector (DBR) (design reflectivity 99.98%) consisting of alternating $\lambda/4$ layers Ta_2O_5 ($n = 2.06$) and SiO_2 ($n = 1.46$) ending with Ta_2O_5 . The ELO-film remains immersed in the solution throughout the exchange of the substrates and the subsequent bonding is conducted completely in DI-water. This provides a very clean environment and hence minimizes contamination with particles between the two surfaces [25]. The weight of the stamp results in pressure on the order of a few N/mm^2 on the sample during the bonding process (step 4. in figure 6.1c). After the highly diluted HF solution is poured away, the sample is dried for 24 h. Ideally, any remaining water film at the bonding interfaces evaporates and the ELO-film is pulled down by surface tension such that close range (VdW) forces bond the layer to the substrate. Experimentally however, a small gap between the interfaces can emerge during the bonding process as shown below. The bonded sample is then detached from the stamp by removing the wax with trichloroethylene (TCE). The resulting bottom mirror structure after bonding is shown in figure 6.1c. The bonding strength of VdW-bonding is sufficient high. Evidence for this is the optical microscope image in figure 6.1d, which shows an intact ELO-film bonded to a DBR mirror even after the immersion in an ultrasonic bath.

6.3 Cavity characterization and performance

6.3.1 Measurement setup

The DBR with the bonded ELO-film serves as an end mirror in the fully tunable plane-concave microcavity setup shown in figure 6.2a and described in detail in [22]. Here, the top mirror consists of a concave mirror with radius of curvature R of $13\text{ }\mu\text{m}$, fabricated by CO_2 -laser ablation and subsequent coating with a $\text{Ta}_2\text{O}_5/\text{SiO}_2$ DBR, exactly the same DBR as the substrate for ELO bonding. Spectral and spatial tunability is realized by mounting the bottom mirror on an xyz-piezo positioner such that it can be displaced in three dimensions with respect to the top mirror. We study the performance of the microcavity including the ELO-bonded bottom mirror at 4 K in a He bath cryostat.

For cavity excitation and detection, we interrogate the system with a coherent cw laser (linewidth 1 MHz) with a cross-polarized detection scheme realized by incorporating two polarizing beam splitters (PBS) in the microscope head at room temperature (figure 6.2b) [27]. The cavity is excited with a fixed linear polarization, while only light

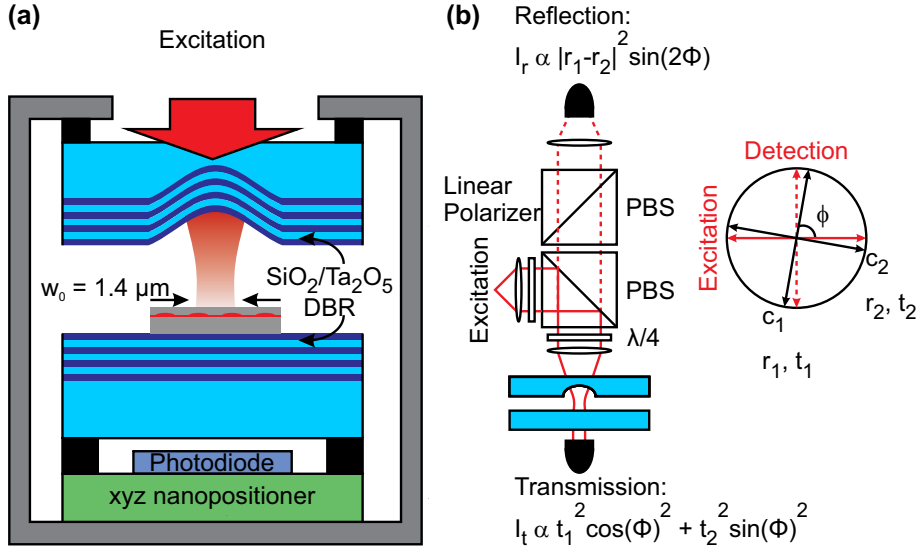


Figure 6.2. (a) Tunable microcavity setup. The ELO-layer is bonded on the dielectric DBR and the entire sample is mounted on an xyz-positioner stage that can be positioned with respect to the concave top mirror. (b) Cross-polarized darkfield detection scheme realized by two polarizing beam splitters. The polarization axes of the cavity mode are only slightly misaligned with respect to the axes of the microscope head.

orthogonally polarized to the excitation is detected. An additional Si-photodetector mounted directly underneath the bottom mirror facilitates cavity transmission measurements.

6.3.2 Cavity properties

Figure 6.3a shows a measurement of the cavity transmission signal as a function of cavity-length detuning for a fixed probe laser beam wavelength $\lambda = 940$ nm. We identify two fundamental cavity modes at physical distance of $\lambda/2$, accompanied by higher order modes. The structure of the cavity mode is described by Hermite-Gaussian TEM_{qnm} modes, where the transversal mode splitting is determined by the radius of curvature of the top mirror. Figure 6.3b shows one cavity resonance with Lorentzian lineshape and a full width at half maximum linewidth (FWHM) of $\delta d = 115 \pm 3$ pm. We identify the finesse in the spatial domain to be $F = \lambda/(2\delta d) = 4,100 \pm 100$. The absolute mode index $q = 2\delta d/\delta\lambda$ is determined by varying the probe wavelength for the first 3 available cavity modes (figure: 6.3c). We reach a minimum mode index of 7.26 ± 0.48 which translates to an effective cavity length of $l = 3.4 \pm 0.2$ μm . This length together with the measured finesse yields a quality factor of $Q = 2lF/\lambda = 30,000$ corresponding to a cavity linewidth

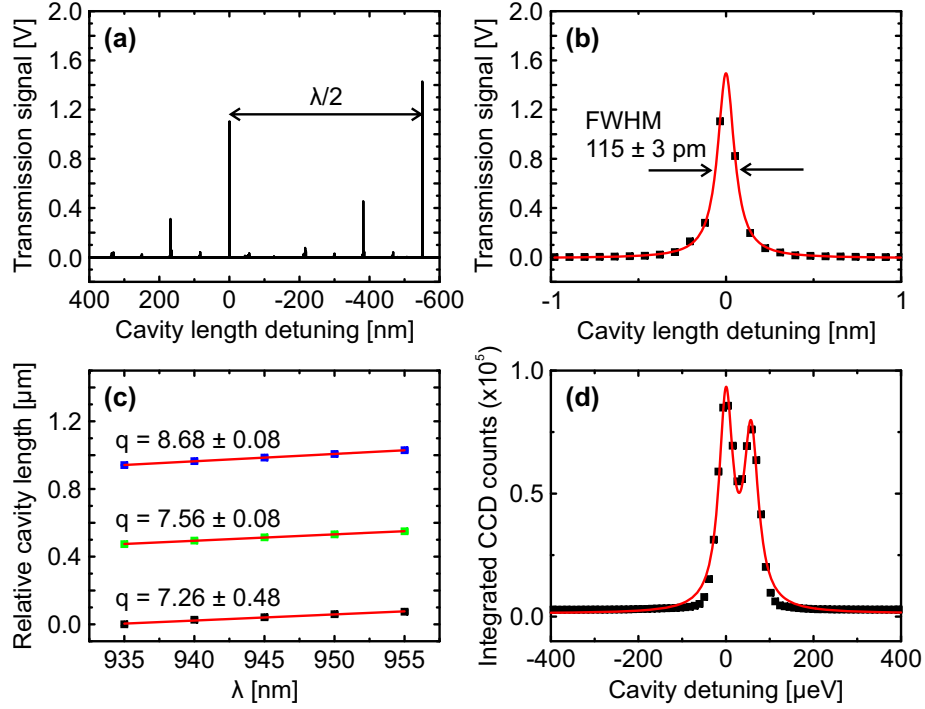


Figure 6.3. Performance of the cavity with an embedded ELO layer without QDs coupled to the cavity mode. (a) Transmission measurement revealing the fundamental and higher order cavity resonances. (b) A single transmission peak with full width half maximum (FWHM) of $\delta d = 115 \pm 3$ pm results in a Finesse of $4,100 \pm 100$. (c) Determination of the smallest accessible mode index by varying the excitation wavelength. (d) A cross-polarized detection of the cavity mode in reflection reveals a mode splitting not observed in transmission (see text).

of $44 \mu\text{eV}$. When measuring in reflection (figure 6.3d), we observe a fundamental mode splitting of $57.65 \mu\text{eV}$. The two modes reveal linewidths of $38.53 \mu\text{eV}$ and $40.29 \mu\text{eV}$ respectively (Q -factors: 34,200 and 32,700), agreeing well with the linewidths expected from finesse and cavity length measurements in transmission.

6.3.3 Cavity mode splitting

The fundamental mode splitting of the microcavity is indicated as c_1 and c_2 in figure 6.2b. The two modes are linearly polarized and we speculate that the splitting arises in the ELO-layer. We note that the linear polarization axes of the c_1 , c_2 modes coincide with the crystallographic axes of the epitaxial lift-off layer. The birefringence may be due to strain-induced anisotropy [28] and was also shown to determine the polarization properties of semiconductor vertical-cavity surface-emitting lasers (VCSELs) [29].

Figure 6.2b shows the alignment of our cross-polarized detection scheme with respect

to the linear polarized cavity modes with an angle ϕ close to $\pi/2$. The two cavity modes can be characterized by the detuning dependent reflection (transmission) coefficients r_1, r_2 (t_1, t_2) that obey the relation $r^2 + t^2 = 1$. We excite the cavity with an electric field amplitude E_0 along the excitation axis and detect orthogonally to it. The total signal that is projected on the detection axis is composed of the two electric amplitudes E_1 and E_2 that originate from the two cavity modes c_1 and c_2 :

$$E_1 = \frac{r_1}{2} E_0 \sin 2\phi, \quad (6.1a)$$

$$E_2 = -\frac{r_2}{2} E_0 \sin 2\phi. \quad (6.1b)$$

We detect an intensity in reflection $I_r = |E_1 + E_2|^2$:

$$I_r = \frac{I_0}{4} |r_1 - r_2|^2 \sin^2 2\phi. \quad (6.2)$$

For the transmission intensity I_t the signal depends solely on the alignment of the excitation with the cavity axis and we can derive:

$$I_t = t_1^2 \cos^2 \phi + t_2^2 \sin^2 \phi. \quad (6.3)$$

These two equations suggest that for an angle ϕ close to 90° only the c_1 mode is efficiently detected in transmission, while in reflection the signal is proportional to the contrast of the detuning-dependent reflection coefficients r_1 and r_2 .

In the present design, the refractive indices satisfy $n_{\text{Ta}_2\text{O}_5}^2 \approx n_{\text{ELO}} n_{\text{SiO}_2}$, close to the condition for an anti-reflection (AR) coating which results in a penetration depth of $6.70 \mu\text{m}$ into the bottom mirror and a minimal total cavity length of $7.32 \mu\text{m}$ when simulated with a 1D transfer matrix method. This is significantly larger than the $3.4 \mu\text{m}$ estimated from the absolute mode index in figure 6.3c. We explain this discrepancy between theory and experiment by an imperfect bonding of the ELO layer to the bottom mirror. A simulation of a 22 nm thick gap with refractive index $n = 1$ (equivalently a 17 nm thick H_2O -film) between the ELO layer and the bottom mirror supports this assumption. Such a configuration breaks the condition of the AR coating and the penetration depth is reduced to $2.06 \mu\text{m}$. Together with an air gap of $\approx 0.5 \mu\text{m}$ (due to imperfect parallelism of the two mirrors) we calculate a total cavity length of $3.00 \mu\text{m}$, in accordance with the measurement.

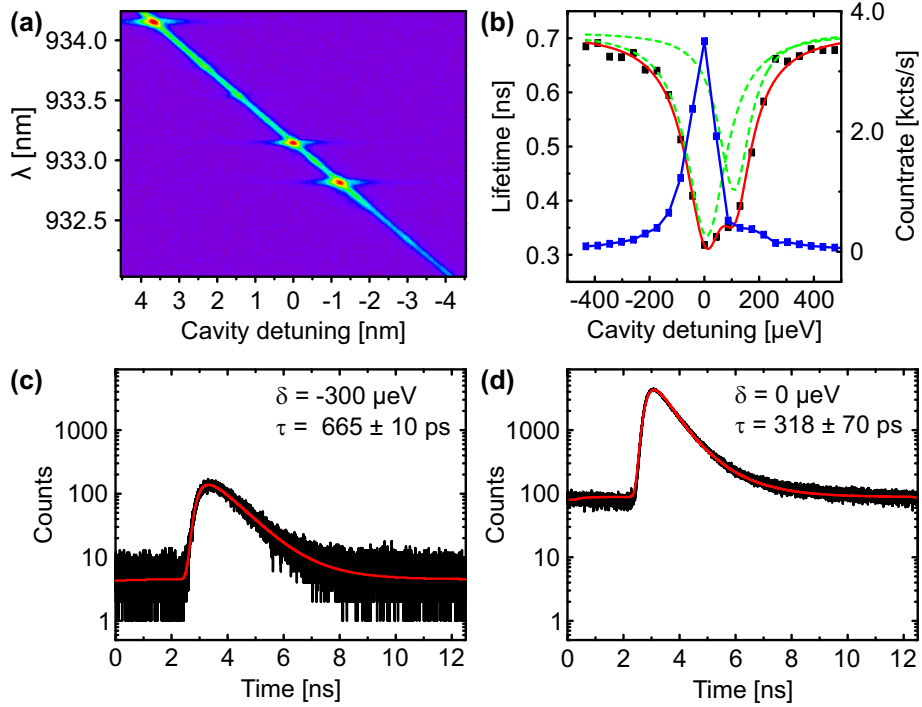


Figure 6.4. Quantum dot in a tunable microcavity. (a) PL spectrum as a function of cavity tuning. Distinct bright points signify the emission from single QDs. (b) Lifetime measurements (black dots) of the QD with $\lambda_{QD} = 933.18$ nm as a function of cavity-dot detuning. A clear reduction of the lifetime is observed on resonance owing to the Purcell effect. The blue dots show the simultaneously recorded total counts. The red curve is a fit to equation 6.4, where the green dashed lines indicate the two Lorentzians of the fit. (c),(d) Lifetime measurement of the cavity 300 μ eV detuned and on resonance. Single exponential fits taking into account the internal response function reveal lifetimes of 665 ps detuned and 318 ps on resonance.

6.4 Coupling quantum dots to the cavity

6.4.1 Photoluminescence measurements

We demonstrate weak coupling of a single InGaAs QD to our tunable microcavity by means of photoluminescence (PL). The cavity-QD system is nonresonantly excited in the wetting layer ($\lambda = 830$ nm) and the emitted signal is analysed by a CCD-based spectrometer with a spectral resolution of 40 μ eV. The cavity resonance is tuned by applying a voltage on the z-piezo, which acts on the cavity length. Figure 6.4a shows the spectrum as a function of cavity detuning. We detect an emission into the cavity mode for all values of z . Earlier crosscorrelation measurements [30, 31] interpreted this background as a hybridization of the higher QD states with the neighboring wetting layer [32]. The discrete bright spots at specific energies indicate the coupling of a single

QD to the cavity mode. The QD transitions observed here do not show a fine-structure splitting, a characterization feature of the neutral exciton X^0 . It is likely that the transitions observed here are charged excitons X^{-1} .

6.4.2 Lifetime measurements

To verify that the enhanced PL at the cavity resonance represents more than spectral filtering of the QD, we study the cavity-QD dynamics in the time domain for a single QD with $\lambda = 933.14$ nm. The cavity-QD system is excited by a Q -switched pulsed nonresonant laserdiode with repetition rate of 80 MHz and a pulse width of 50 ps. The excitation pulse defines the start signal. The stop signal is provided by the detection of an emitted photon by an avalanche photodiode with a timing resolution of 340 ps and a dark-count rate of 20 counts per second. Figure 6.4c shows a lifetime measurement of the cavity-QD system at 300 μeV detuning. A single exponential fit taking into account the internal response function (IRF) reveals a lifetime of 665 ± 10 ps (corresponding 1.00 ± 0.02 μeV). At zero detuning (figure 6.4d), the lifetime of the QD is reduced to 318 ± 70 ps (corresponding 2.07 ± 0.45 μeV) implying an increased spontaneous emission rate.

Figure 6.4b shows lifetime measurements for different cavity-QD detunings. Due to the cross-polarized detection, only one cavity mode is observed in PL (figure 6.4a). However, the QD still couples to both orthogonally polarized modes and we expect a lifetime reduction in both cases. Thus the simultaneously recorded countrate (blue dots in figure 6.4b) reduces at a detuning where the lifetime still remains low. Consequently, we fit the lifetime data in figure 6.4b with a double-Lorentzian:

$$\frac{\gamma_{\text{cavity}}}{\gamma_{\text{free}}} = \frac{F_{\text{P1}}\Delta_1^2}{4\delta_1^2 + \Delta_1^2} + \frac{F_{\text{P2}}\Delta_2^2}{4\delta_2^2 + \Delta_2^2} + \alpha. \quad (6.4)$$

The lifetime of five different QDs not coupled to the cavity mode were measured yielding an average freespace lifetime of 805 ± 150 ps, or $\gamma_{\text{free}} = 0.82 \pm 0.15$ μeV . In contrast, γ_{cavity} is the decay rate into the cavity mode. The first two terms in equation 6.4 describe the cavity-QD detuning-dependent relative decay rate according to the density of states in the two microcavity modes. The term α describes the relative decay rate into leaky modes of the cavity. F_{P1} (F_{P2}) is the Purcell factor corresponding to the first (second) cavity mode, Δ_1 and Δ_2 are the two cavity mode linewidths and δ_1 (δ_2) is the cavity-QD detuning with respect to the first (second) cavity mode.

From the fit, we determine Purcell factors of $F_{\text{P1}} = 1.27 \pm 0.04$, $F_{\text{P2}} = 0.79 \pm 0.04$

and $\alpha = 1.12 \pm 0.01$. The corresponding linewidths are $\Delta_1 = 121.83 \pm 5.8 \mu\text{eV}$ and $\Delta_2 = 106.93 \pm 10.71 \mu\text{eV}$ and the splitting between the modes is $100.14 \pm 5.11 \mu\text{eV}$. The errors on the determination of the two Purcell factors F_{P1} and F_{P2} arise from the statistical error of γ_{free} , while the errors in the widths arise from the double-Lorentzian fit. The linewidth values are significantly larger than those in figure 6.3d, where the cavity was probed with a laser and a cross-polarized detection scheme. An explanation for this would be a heating effect during nonresonant excitation that broadens the cavity resonance. However, this would not affect an increase in the cavity mode splitting as is observed in the experiment. Moreover, we attribute the broadening to the long integration times (30 minutes) for each point in figure 6.4b in order to achieve low noise decay curves. On these long timescales the cavity resonance drifts slightly since we do not actively stabilize the cavity length during measurement. This drift of the cavity increases the apparent mode-splitting by a factor of ≈ 2 . Therefore we argue that the estimated Purcell factors represents the lower limit that is reached in the present setup. Correcting for the drift we evaluate $F'_{P1} \approx 2.54$ and $F'_{P2} \approx 1.6$. We note also that if the c_1, c_2 splitting could be eliminated, F_p would rise to ~ 4.14 .

6.4.3 Estimation of the coupling strength

Once the Purcell factor is known an effective mode volume can be estimated by:

$$V_0 = \frac{3Q(\lambda/n)^3}{4\pi^2 F_p}, \quad (6.5)$$

with a Q -factor of 33,000 and an averaged refractive index n of the ELO-layer of 3.332. The free space decay rate $\gamma_{\text{free}} = 0.82 \mu\text{eV}$ translates into a dipole moment μ_{12} of $1.2 \text{ nm} \times e$ and we calculate the coupling g from

$$g = \sqrt{\frac{\mu_{12}^2 \omega}{2\epsilon_0 n^2 \hbar V_0}}. \quad (6.6)$$

We find $g = 10.7 \mu\text{eV}$ if the splitting would be eliminated ($F_p = 4.14$) and $g_1 = 8.37 \mu\text{eV}$ for the first mode with $F'_{P1} = 2.54$. We estimate a vacuum field E_{vac} at the location of the QDs via $\hbar g = \mu_{12} E_{\text{vac}}$ to be $E_{\text{vac}} = 0.9 \times 10^4 \text{ V/m}$. From the radius of curvature (13 μm) we estimate a beam waist of $w_0 = 1.74 \mu\text{m}$ by Gaussian optics. The transfer matrix method yields then a field antinode at the emitter of $E_{\text{vac}} = 2.5 \times 10^4 \text{ V/m}$ (see figure 6.1b). The experimental result from the Purcell effect ($0.9 \times 10^4 \text{ V/m}$) is lower

than the geometric estimate (2.5×10^4 V/m). Imperfections at the bonding interface may shift the maximum of the vacuum field such that the location of the QD does not coincide with the electric field antinode. However, simulations with an airgap of 22 nm between the ELO layer and the bottom mirror suggest that this effect is negligible: the shorter penetration depth results in an increased vacuum field compensating for the vertical displacement of the antinode.

Since we do not have immediate access to the QD uncoupled to the cavity in our setup, the free space decay rate γ_{free} remains the uncertain factor for the Purcell factor estimation. However, the estimation of the coupling strength g is stable with respect to γ_{free} . This is due to the fact that in our analysis the Purcell factor scales with $1/\gamma_{\text{free}}$ and hence $g \propto 1/\sqrt{\gamma_{\text{free}}}$, while simultaneously g is proportional to $\mu_{12} \propto \sqrt{\gamma_{\text{free}}}$ and the γ_{free} – dependency of g cancels out.

We point out with an observed coupling rate $g_1 \approx 8.4$ μeV and cavity rate $\kappa \approx 40$ $\mu\text{eV} \gg \gamma$, the cavity–QD dynamics are already close to the strong coupling regime $4g > |\kappa - \gamma|$. Moreover, our setup offers several possibilities to improve the cooperativity factor. Notably κ can be significantly reduced by using ‘supermirrors’ with an ultrahigh reflectivity. Furthermore, as mentioned above, the current configuration at the interface of $3\lambda/4$ ELO / $\lambda/4$ Ta₂O₅ / $\lambda/4$ SiO₂ results in a relatively high penetration depth and an unwanted reduction of the vacuum field strength. Now that a high quality ELO layer–DBR mirror is established, a λ –layer ELO can be bonded to a SiO₂–terminated DBR. Simulations suggest a reduction of the penetration depth from 6.70 μm to 4.30 μm and an increase of the vacuum field strength by factor 1.4 – already enough to observe a clear strong–coupling signature. To reduce the mode volume further, one possibility would be to use materials for the mirrors with a higher refractive index contrast.

6.5 Conclusion

In conclusion we have demonstrated a hybrid high– Q , low mode–volume tunable Fabry–Pérot microcavity consisting of a thin GaAs epilayer and dielectric mirrors. The fundamental requirements for cavity QED are met in this system: the finesse was high despite the new interface between dissimilar materials and the QDs remained optically active with low linewidths. Furthermore, we verified that the QD–cavity system operates in the weak coupling regime close to strong coupling. We argue that our epitaxial lift–off approach opens new possibilities for cavity QED in the solid state.

We acknowledge financial support from SNF (project 200020–156637) and NCCR

QSIT.

References

- [1] E. Purcell, [Physical Review](#) **69**, 681 (1946).
- [2] J. Vučković, D. Fattal, C. Santori, G. S. Solomon, and Y. Yamamoto, [Applied Physics Letters](#) **82**, 3596 (2003).
- [3] S. Strauf, N. G. Stoltz, M. T. Rakher, L. A. Coldren, P. M. Petroff, and D. Bouwmeester, [Nature Photonics](#) **1**, 704 (2007).
- [4] A. J. Shields, [Nature Photonics](#) **1**, 215 (2007).
- [5] K. M. Birnbaum, A. Boca, R. Miller, A. D. Boozer, T. E. Northup, and H. J. Kimble, [Nature](#) **436**, 87 (2005).
- [6] A. Imamoglu, D. D. Awschalom, G. Burkard, D. P. DiVincenzo, D. Loss, M. Sherwin, and A. Small, [Physical Review Letters](#) **83**, 4204 (1999).
- [7] J. M. Gérard, B. Sermage, B. Gayral, B. Legrand, E. Costard, and V. Thierry-Mieg, [Physical Review Letters](#) **81**, 1110 (1998).
- [8] J. Reithmaier, G. Sek, A. Löffler, C. Hofmann, S. Kuhn, S. Reitzenstein, L. Keldysh, V. Kulakovskii, T. Reinecke, and A. Forchel, [Nature](#) **432**, 197 (2004).
- [9] M. Lerner, N. Gregersen, F. Dunzer, S. Reitzenstein, S. Höfling, J. Mørk, L. Worschech, M. Kamp, and A. Forchel, [Physical Review Letters](#) **108**, 057402 (2012).
- [10] W.-H. Chang, W.-Y. Chen, H.-S. Chang, T.-P. Hsieh, J.-I. Chyi, and T.-M. Hsu, [Physical Review Letters](#) **96**, 117401 (2006).
- [11] T. Yoshie, A. Scherer, J. Hendrickson, G. Khitrova, H. M. Gibbs, G. Rupper, C. Ell, O. B. Shchekin, and D. G. Deppe, [Nature](#) **432**, 200 (2004).
- [12] D. Englund, A. Majumdar, M. Bajcsy, A. Faraon, P. Petroff, and J. Vučković, [Physical Review Letters](#) **108**, 093604 (2012).
- [13] K. Hennessy, A. Badolato, M. Winger, D. Gerace, M. Atatüre, S. Gulde, S. Fält, E. L. Hu, and A. Imamoglu, [Nature](#) **445**, 896 (2007).

- [14] R. J. Barbour, P. A. Dalgarno, A. Curran, K. M. Nowak, H. J. Baker, D. R. Hall, N. G. Stoltz, P. M. Petroff, and R. J. Warburton, [Journal of Applied Physics](#) **110**, 053107 (2011).
- [15] A. Muller, E. B. Flagg, M. Metcalfe, J. Lawall, and G. S. Solomon, [Applied Physics Letters](#) **95**, 173101 (2009).
- [16] J. Miguel-Sánchez, A. Reinhard, E. Togan, T. Volz, A. Imamoğlu, B. Besga, J. Reichel, and J. Estève, [New Journal of Physics](#) **15**, 045002 (2013).
- [17] L. Greuter, S. Starosielec, A. V. Kuhlmann, and R. J. Warburton, [arXiv:1504.06223](#) (2015).
- [18] L. C. Andreani, G. Panzarini, and J.-M. Gérard, [Physical Review B](#) **60**, 13276 (1999).
- [19] D. Hunger, T. Steinmetz, Y. Colombe, C. Deutsch, T. W. Hänsch, and J. Reichel, [New Journal of Physics](#) **12**, 065038 (2010).
- [20] S. Dufferwiel, F. Fras, A. Trichet, P. M. Walker, F. Li, L. Giriunas, M. N. Makhonin, L. R. Wilson, J. M. Smith, E. Clarke, M. S. Skolnick, and D. N. Krizhanovskii, [Applied Physics Letters](#) **104**, 192107 (2014).
- [21] S. Schwarz, S. Dufferwiel, P. M. Walker, F. Withers, A. A. P. Trichet, M. Sich, F. Li, E. A. Chekhovich, D. N. Borisenko, N. N. Kolesnikov, K. S. Novoselov, M. S. Skolnick, J. M. Smith, D. N. Krizhanovskii, and A. I. Tartakovskii, [Nano Letters](#) **14**, 7003 (2014).
- [22] L. Greuter, S. Starosielec, D. Najer, A. Ludwig, L. Duempelmann, D. Rohner, and R. J. Warburton, [Applied Physics Letters](#) **105**, 121105 (2014).
- [23] P. A. Dalgarno, J. M. Smith, J. McFarlane, B. D. Gerardot, K. Karrai, A. Badolato, P. M. Petroff, and R. J. Warburton, [Physical Review B](#) **77**, 245311 (2008).
- [24] G. Rempe, R. Lalezari, R. J. Thompson, and H. J. Kimble, [Optics Letters](#) **17**, 363 (1992).
- [25] E. Yablonovitch, D. M. Hwang, T. J. Gmitter, L. T. Florez, and J. P. Harbison, [Applied Physics Letters](#) **56**, 2419 (1990).

-
- [26] P. Demeester, I. Pollentier, P. De Dobbelaere, C. Brys, and P. Van Daele, [Semiconductor Science and Technology](#) **8**, 1124 (1993).
 - [27] A. V. Kuhlmann, J. Houel, D. Brunner, A. Ludwig, D. Reuter, A. D. Wieck, and R. J. Warburton, [Review of Scientific Instruments](#) **84**, 073905 (2013).
 - [28] J. P. van der Ziel and A. C. Gossard, [Journal of Applied Physics](#) **48**, 3018 (1977).
 - [29] A. K. Jansen van Doorn, M. P. van Exter, and J. P. Woerdman, [Applied Physics Letters](#) **69**, 1041 (1996).
 - [30] M. Winger, T. Volz, G. Tarel, S. Portolan, A. Badolato, K. J. Hennessy, E. L. Hu, A. Beveratos, J. Finley, V. Savona, and A. Imamoglu, [Physical Review Letters](#) **103**, 207403 (2009).
 - [31] M. Kaniber, A. Laucht, A. Neumann, J. M. Villas-Bôas, M. Bichler, M.-C. Amann, and J. J. Finley, [Physical Review B](#) **77**, 161303 (2008).
 - [32] K. Karrai, R. J. Warburton, C. Schulhauser, A. Hoge, B. Urbaszek, E. J. McGhee, A. O. Govorov, J. M. Garcia, B. D. Gerardot, and P. M. Petroff, [Nature](#) **427**, 135 (2004).

Chapter 7

Conclusion and outlook

7.1 Conclusion

This thesis describes the development of a fully tunable, miniaturized Fabry–Pérot microcavity and the coupling with single self assembled quantum dots. Generally, the open access of the system enables various two level emitters to be coupled to the microcavity and hence build a powerful tool for experiments in the field of cavity quantum electrodynamics (CQED). For applications in CQED the cooperativity, defined as $C = 2g^2/\kappa\gamma$, is the figure of merit that includes all the relevant rates: γ describing the emitter decay, κ the cavity decay and g the cavity–emitter interaction strength. A high cooperativity is desirable.

The microcavity consists of a plane–concave mirror pair; a small radius of curvature of the concave top mirror enables a reduction in the cavity mode volume. The small radius of curvature is achieved by CO₂ laser ablation of fused silica described in chapter 2. Here, the exact power and exposure time incident on the silica substrate is controlled by incorporating an acousto optical modulator into the CO₂ laser setup. This allowed for the reproducible production of craters with a large variety of different radii of curvature. The surface tension of the molten silica layer smoothens the roughness in the ablated craters, resulting in a root mean square surface roughness as low as 0.2 nm, as determined by atomic force microscopy. As a central result, concave structures have been produced with radii of curvature less than 10 μm .

The concave top mirrors were then coated with a distributed Bragg reflector (DBR) consisting of either pairs of TiO₂/SiO₂ or Ta₂O₅/SiO₂ before they were implemented into the fully tunable microcavity. The properties of the microcavity setup are described and analyzed in Chapter 3. Here, the precise spectral and spatial tuning is achieved by piezo–positioning of the two mirrors with respect to each other. By using a gold coated

GaAs substrate, the spacing of the higher-order modes was analyzed. Hence, it was verified that the small radii of curvature obtained by CO₂ laser ablation coincide with the optical radius inferred from the modes in the cavity. The corresponding cavity beam waist was determined by using a sharp gold/GaAs edge defined by electron beam lithography. By laterally moving the bottom mirror with respect to the top mirror, the position-dependent cavity finesse is determined, where the beam waist could be deduced from the edge. The possibility to record a position dependent finesse allows in principle for the realization of a microcavity microscope.

By using a combination of mirrors, where both have a Ta₂O₅/SiO₂-DBR coating, a cavity finesse of $\approx 15,000$ could be measured. However, the measured resonances reveal non-Lorentzian lineshapes due to acoustic noise broadening. The effect from the acoustic noise has been quantified in our system at 4 K, where an acoustic noise amplitude of 4.3 pm was revealed. This allows to work with a finesse of up to 11,000 in the present system.

Chapter 4 describes the coherent coupling of an InGaAs quantum dot (QD) grown on a semiconductor DBR to the fully tunable microcavity. A great advantage of the cavity design is that it is possible to position spatially the quantum dot inside the cavity and spectrally match the QD transition to the cavity resonance. The strong coupling regime was clearly reached, manifested as a clear anticrossing signature as the cavity is tuned across the QD resonance. A naive analysis that models the system with the well-known Jaynes-Cummings model results in a cooperativity value of 5.5, where the obtained spectra are not well reproduced. However, the measurement data could be explained by including a spectral diffusion that inhomogeneously broadens the QD resonance. Additional power depending resonance fluorescence measurements of several QDs from the same sample but uncoupled to the cavity, verified the presence of spectral diffusion in the sample. It is argued that by minimizing spectral wandering an estimated cooperativity value of 9.0 can be reached with this particular implementation.

The cooperativity can be further increased by reducing the mode volume and increasing the Q -factor of the cavity. An approach is presented in chapter 6 to meet these requirements. An epitaxially lift-off layer containing QDs is bonded to a high reflectivity mirror DBR, which is then incorporated into the tunable microcavity design. This represents a best-of-both-worlds approach, where an ideal emitter can be combined with a highly reflective mirror. Successful epitaxial lift-off and subsequent bonding of a $3\lambda/4$ layer on top of a Ta₂O₅/SiO₂ mirror is presented. This design is chosen such that an electric field node lies exactly at the bonding interface. The weak coupling regime

is demonstrated, which is manifested by a decreased lifetime of the QD when resonant with the cavity mode: the and the Purcell factor is 3.3.

7.2 Outlook

Overall the development of the fully tunable microcavity allowed the strong coupling regime using a single InGaAs QD. However, a clear goal is to improve the cooperativity with this setup. This is realized by improving essentially the three aspects that define the cooperativity: the cavity Q -factor (which determines κ), the coupling strength g and the emitter γ .

7.2.1 Cavity Q -factor

Higher Q -factors can be achieved by improving the reflectivity of the involved mirrors, realized by increasing the number of ion-beam sputtered DBR pairs. Here, finesse of up to 10^6 are possible for CQED [1]. However, a very high finesse requires an improved stability regarding acoustic noise in our setup. So far acoustic noise is reduced by putting the cryostat with the microcavity setup inserted into an acoustic-shielding box. However, the issue could further be addressed by implementing an active cavity-length stabilization protocol. Here, the idea is to use an additional laser with a different frequency, ideally outside the DBR-stopband, for which the finesse is not as high. The frequency of the stabilization laser is chosen such that the narrow cavity peak of the frequency under study lies at the edge of the broader resonance emerging from the stabilization laser light. Here, the stabilization signal is recorded in transmission and the cavity can now be stabilized by a proportional-integral-derivative (PID) feedback scheme. The microcavity system can be simultaneously studied in reflection, whereas distinguishing the probe laser from the stabilization laser is achieved using common razor edge filters.

7.2.2 Coupling strength g

The coupling strength is enhanced by reducing the cavity mode volume. This can be naturally achieved by decreasing the radius of curvature of the concave top mirror. Essentially a radius of curvature well below $10\ \mu\text{m}$ can be produced by CO_2 -laser ablation. However, small radii of curvature are only achieved with correspondingly deep craters that enlarges the cavity mode volume and render the cavity mode unstable. A possibility is to etch the craters post ablation without disturbing the radius of curvature. However

this is challenging to achieve in practice. A promising approach is to pre-etch a narrow cylinder with a moderate depth into the silica substrate. The structure is then locally melted by the CO₂-laser which transforms the cylinder structure into a concave shape. Here, the radius of curvature is determined by the dimensions of the etched cylinder. In principle concave mirrors can also be produced by ion-beam milling [2]. With this technique small radii of curvature for low crater depths can be fabricated but the surface roughness is not as smooth as for CO₂-laser ablation. A method here could be to combine ion beam milling with CO₂-laser ablation, where the small radii of curvature are produced by ion beam milling before subsequent smoothing with a short CO₂-laser pulse.

The reduction of the cavity mode volume is mainly limited by the finite penetration depths into the DBRs. The epitaxial lift-off approach presents here a possibility of decreasing further the cavity mode volume. In the approach presented so far the epitaxial lift-off layer had a thickness of $3\lambda/4$ bonded on a DBR mirror ending on the high index material (i.e Ta₂O₅). Here, the configuration was chosen such that an electric field node is located at the bonding interface and that fabrication imperfections only have limited influence on the cavity finesse. However, 1D transfer matrix simulation show that the penetration depth can be reduced by bonding a λ -layer on the low index material (SiO₂) which results in an enhancement of the vacuum field strength at the location of the dots by a factor of 1.4. We note here that generally the issue of a large penetration depth into DBR mirrors is addressed by choosing layers that exhibit a large refractive index contrast. A particularly interesting approach is to use a GaAs/air DBR [3]. Here, already a few pairs result in an extremely high reflectivity (e.g. for 3 pairs $R > 99.995\%$). Furthermore, the penetration can be reduced to $3.70\ \mu\text{m}$ compared to the $6.70\ \mu\text{m}$ from the $3\lambda/4$ configuration, resulting in an enhancement of the vacuum field by a factor of 1.6.

7.2.3 Emitter decay γ

The prior suggestions for enhancement of the cooperativity factor mainly focused on the improvement of the microcavity properties. However, this thesis demonstrates that spectral diffusion is present in our device, which increases the linewidth of the emitter and hence decreases the cooperativity value. To address this issue, the QDs can be incorporated in a p-i-n field effect structure before being incorporated into the microcavity [4]. Here, silicon-doped GaAs is used for the n-back contact, while a carbon doped GaAs constitutes the p-layer [5]. In the presence of such an epitaxial gate, the

charges that surround the QD can be electrostatically pulled away from the vicinity of the QD, hence minimizing the impact of charge noise on the QD [6]. Therefore the presence of an epitaxial gate narrows the line of the QDs. Furthermore, using an epitaxial gate allows the QD to be charged deterministically. In this case the bare cavity peak disappears as the charge switching of the QD is suppressed. Finally, the charge control inside a QD ultimately opens access to spin-physics inside the microcavity.

References

- [1] G. Rempe, R. Lalezari, R. J. Thompson, and H. J. Kimble, [Optics Letters](#) **17**, 363 (1992).
- [2] D. Ziyun, H. V. Jones, P. R. Dolan, S. M. Fairclough, M. B. Wincott, J. Fill, G. M. Hughes, and J. M. Smith, [New Journal of Physics](#) **14**, 103048 (2012).
- [3] J. Gessler, T. Steinl, A. Mika, J. Fischer, G. Şek, J. Misiewicz, S. Höfling, C. Schneider, and M. Kamp, [Applied Physics Letters](#) **104**, 081113 (2014).
- [4] J. Miguel-Sánchez, A. Reinhard, E. Togan, T. Volz, A. Imamoglu, B. Besga, J. Reichel, and J. Estève, [New Journal of Physics](#) **15**, 045002 (2013).
- [5] P. Borri, W. Langbein, S. Schneider, U. Woggon, R. L. Sellin, D. Ouyang, and D. Bimberg, [Physical Review Letters](#) **87**, 157401 (2001).
- [6] J. Houel, A. V. Kuhlmann, L. Greuter, F. Xue, M. Poggio, B. D. Gerardot, P. A. Dalgarno, A. Badolato, P. M. Petroff, A. Ludwig, D. Reuter, A. D. Wieck, and R. J. Warburton, [Physical Review Letters](#) **108**, 107401 (2012).

APPENDIX

Supplementary Information to Chapter 4

Appendix A

Towards high cooperativity strong coupling of a quantum dot in a tunable microcavity, supplementary information

A.1 Sample structure

A self-assembled InGaAs quantum dot is positioned at cavity mode electric field antinode, as depicted in figure A.1a. The heterostructure was grown by molecular beam epitaxy by Pierre Petroff at UCSB California, and consists of a 100 nm GaAs smoothing layer on a GaAs substrate, and a 32.5 pair $\lambda/4$ AlGaAs/GaAs distributed Bragg reflector (DBR) as the bottom mirror of the microcavity, which is terminated by a λ -layer GaAs host matrix. During growth, the InGaAs wetting layer is inserted at a $\lambda/2$ distance from the sample surface (figure A.1b). The top mirror is produced by CO₂ laser ablation from a fused silica substrate, where a concave depression with radius of curvature $\approx 13 \mu\text{m}$ is created before a Ta₂O₅ DBR coating is applied by ion-beam sputtering. The nominal reflectivities are $R_{\text{bot}} = 99.99\%$ and $R_{\text{top}} = 99.95\%$. The bottom mirror is mounted on an xyz piezo-driven positioner for sub-nm positioning, allowing both spectral and spatial tuning of the microcavity. Estimating from Gaussian optics a beam waist of $w = 1.4 \mu\text{m}$ at the quantum dot position from the cavity geometry, with one-dimensional transfer matrix method calculations we estimate a vacuum electric field of $E_{\text{vac}} \approx 2 \times 10^4 \text{V/m}$. At 4 K, single quantum dots can be addressed in the wavelength range of 930 . . . 960 nm.

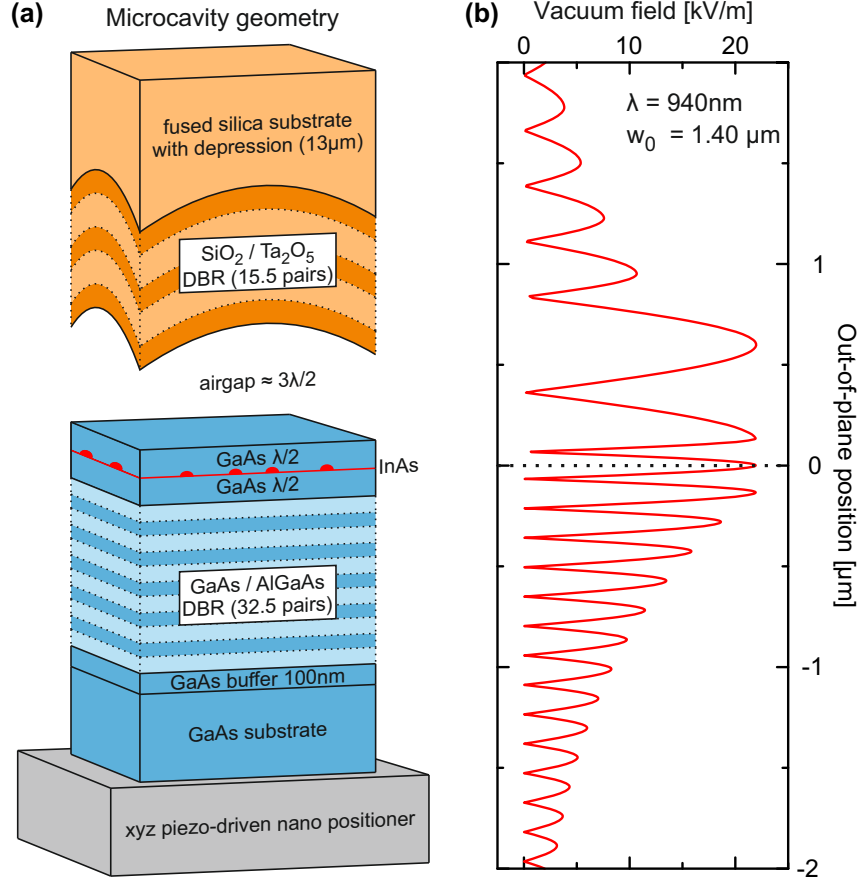


Figure A.1. (a) Sample structure within cavity configuration and (b) estimated vacuum field distribution for the design wavelength of $\lambda = 940$ nm. The field distribution is estimated from one-dimensional transfer matrix methods, with a Gaussian beam waist of $w_0 = 1.4 \mu\text{m}$.

A.2 Model calculation (M1)

The model Hamiltonian of the article reads, in the rotating frame of the coherent excitation at frequency ω_R ,

$$\mathcal{H} = \hbar(\omega_C - \omega_R) a^\dagger a + \hbar(\omega_X - \omega_R) b^\dagger b + \hbar g (a^\dagger b + b^\dagger a) + \hbar \epsilon (a^\dagger + a) \quad , \quad (\text{A.1})$$

where a denotes the bosonic annihilation operator of the cavity (C) and b the fermionic annihilation operator of the exciton transition (X). Here, g is the coherent cavity-exciton coupling rate, and ϵ is the coherent excitation rate driving the bare cavity resonance from an external laser field whose linewidth is neglected. Treating ϵ as a perturbation parameter, in the absence of other pumping mechanisms the resulting field amplitudes will be of order $a, b \propto \epsilon$.

The coherent and incoherent evolution of the density matrix ρ is given by the Lindblad operator description

$$\begin{aligned} \frac{d\rho}{dt} = & \frac{i}{\hbar}[\rho, \mathcal{H}] + \frac{\kappa}{2}(2a\rho a^\dagger - a^\dagger a\rho - \rho a^\dagger a) \\ & + \frac{\gamma_g}{2}(2b\rho b^\dagger - b^\dagger b\rho - \rho b^\dagger b) \\ & + \frac{\gamma_{pd}}{4}(b_z\rho b_z - \rho) , \end{aligned} \quad (\text{A.2})$$

with the cavity photon loss rate κ of the single cavity mode under consideration; γ_g denotes the exciton's spontaneous emission rate into other guided modes of the cavity. For completion, we also consider an exciton pure dephasing contribution γ_{pd} (where $b_z = 1 - 2b^\dagger b$), whose effect on the dynamics is considered further below.

Observables O inherit a time-dependent expectation value $\langle O \rangle(t) = \text{Tr}[\rho(t)O]$ from the density matrix. The expectation values of the lowest orders of normal-ordered field operators yield a set of optical Bloch equations

$$\frac{d}{dt}\langle a^\dagger \rangle = \left[i(\omega_C - \omega_R) - \frac{\kappa}{2} \right] \langle a^\dagger \rangle + ig\langle b^\dagger \rangle + i\epsilon \quad (\text{A.3a})$$

$$\begin{aligned} \frac{d}{dt}\langle b^\dagger \rangle = & \left[i(\omega_X - \omega_R) - \frac{\gamma_g + \gamma_{pd}}{2} \right] \langle b^\dagger \rangle + ig\langle a^\dagger \rangle \\ & - 2ig\langle a^\dagger b^\dagger b \rangle \end{aligned} \quad (\text{A.3b})$$

$$\frac{d}{dt}\langle a^\dagger a \rangle = -\kappa\langle a^\dagger a \rangle - [ig\langle a^\dagger b \rangle + i\epsilon\langle a^\dagger \rangle + \text{h.c.}] \quad (\text{A.3c})$$

$$\frac{d}{dt}\langle b^\dagger b \rangle = -\gamma_g\langle b^\dagger b \rangle + [ig\langle a^\dagger b \rangle + \text{h.c.}] \quad (\text{A.3d})$$

$$\begin{aligned} \frac{d}{dt}\langle b^\dagger a \rangle = & \left[i(\omega_X - \omega_C) - \frac{\gamma_g + \gamma_{pd} + \kappa}{2} \right] \langle b^\dagger a \rangle \\ & + ig(\langle a^\dagger a \rangle - \langle b^\dagger b \rangle) - i\epsilon\langle b^\dagger \rangle - 2ig\langle a^\dagger b^\dagger ab \rangle . \end{aligned} \quad (\text{A.3e})$$

The higher-order terms $\langle a^\dagger b^\dagger b \rangle$ and $\langle a^\dagger b^\dagger ab \rangle$ originate from the fermionic nature of the exciton after applying the commutator rule $[b, b^\dagger] = 1 - 2b^\dagger b$ and thus represent all saturation effects. At weak excitations $\epsilon \propto b \ll 1$ these contributions are suppressed and are further neglected. For vanishing pure dephasing rate $\gamma_{pd} \ll \gamma_g$, the set of optical Bloch equations are solved by the ansatz $\langle a^\dagger a \rangle = \langle a^\dagger \rangle \langle a \rangle$, $\langle b^\dagger b \rangle = \langle b^\dagger \rangle \langle b \rangle$ and $\langle b^\dagger a \rangle = \langle b^\dagger \rangle \langle a \rangle$

with $\langle a^\dagger \rangle$ and $\langle b^\dagger \rangle$ the solution to eq. (A.3a-b). The steady state ($d/dt \equiv 0$) yields

$$\langle a^\dagger \rangle = \frac{\epsilon(\omega_X - \omega_R + i\frac{\gamma_g}{2})}{g^2 - (\omega_X - \omega_R + i\frac{\gamma_g}{2})(\omega_C - \omega_R + i\frac{\kappa}{2})} \quad (\text{A.4a})$$

$$= \frac{\epsilon_+^a}{\omega_R - \omega_+} + \frac{\epsilon_-^a}{\omega_R - \omega_-} \quad (\text{A.4b})$$

$$\langle b^\dagger \rangle = \frac{\epsilon g}{g^2 - (\omega_X - \omega_R + i\frac{\gamma_g}{2})(\omega_C - \omega_R + i\frac{\kappa}{2})} \quad (\text{A.4c})$$

$$= \frac{\epsilon_+^b}{\omega_R - \omega_+} + \frac{\epsilon_-^b}{\omega_R - \omega_-} . \quad (\text{A.4d})$$

As a function of the resonant probe ω_R , a double pole structure arises at complex Rabi frequencies

$$\omega_\pm = \frac{\omega_C + \omega_X}{2} + i\frac{\kappa + \gamma_g}{4} \pm \sqrt{g^2 + \left(\frac{\omega_C - \omega_X}{2} + i\frac{\kappa - \gamma_g}{4} \right)^2} \quad (\text{A.5})$$

with projected excitation rates

$$\epsilon_\pm^a = \frac{\epsilon}{2} \left[1 \pm \frac{\frac{\omega_C - \omega_X}{2} + i\frac{\kappa - \gamma_g}{4}}{\sqrt{g^2 + \left(\frac{\omega_C - \omega_X}{2} + i\frac{\kappa - \gamma_g}{4} \right)^2}} \right] \quad (\text{A.6a})$$

$$\epsilon_\pm^b = \mp \frac{\epsilon}{2} \left[\frac{g}{\sqrt{g^2 + \left(\frac{\omega_C - \omega_X}{2} + i\frac{\kappa - \gamma_g}{4} \right)^2}} \right] . \quad (\text{A.6b})$$

So far, the detection channel has not been explicitly modelled. A weak coupling of the cavity to a continuum of lossy detection modes contributes a photon flux of $\eta\kappa\langle a^\dagger a \rangle$ to the observed intensity, where the collection efficiency η has no dependence on the cavity tuning. In the weak excitation regime, both the absolute value of $\langle a^\dagger a \rangle$ and the excitation rate ϵ are difficult to determine experimentally. We note that the detected intensity is proportional to $\langle a^\dagger a \rangle$, and limit our study to its dependence on ω_R . A partial fraction decomposition of the absolute square of $\langle a^\dagger \rangle$ from eq. (A.4a) yields

$$\begin{aligned} \langle a^\dagger a \rangle &= [V_+ + \text{Re } W] \mathcal{L}(\omega_R - \omega_+) + \text{Im } W \mathcal{D}(\omega_R - \omega_+) \\ &+ [V_- + \text{Re } W] \mathcal{L}(\omega_R - \omega_-) - \text{Im } W \mathcal{D}(\omega_R - \omega_-) , \end{aligned} \quad (\text{A.7})$$

i.e. a sum of unit-area Lorentzian and corresponding dispersive function lineshapes

$$\mathcal{L}(\omega_R - \omega_{\pm}) = \frac{\text{Im } \omega_{\pm} / \pi}{(\omega_R - \text{Re } \omega_{\pm})^2 + (\text{Im } \omega_{\pm})^2} \quad (\text{A.8a})$$

$$\mathcal{D}(\omega_R - \omega_{\pm}) = \frac{(\omega_R - \text{Re } \omega_{\pm}) / \pi}{(\omega_R - \text{Re } \omega_{\pm})^2 + (\text{Im } \omega_{\pm})^2} \quad (\text{A.8b})$$

with magnitudes

$$V_{\pm} = \frac{\pi |\epsilon_{\pm}^a|^2}{\text{Im } \omega_{\pm}} \quad \text{and} \quad W = 2\pi i \frac{\epsilon_+^a \epsilon_-^{a*}}{\omega_+ - \omega_-^*}, \quad (\text{A.9})$$

where $(*)$ denotes complex conjugation. The lineshape resonances are located at $\text{Re } \omega_{\pm}$ with FWHM parameter $2|\text{Im } \omega_{\pm}|$. The result for $\langle b^\dagger b \rangle$ is analogous to eq.(A.7), with ϵ^b substituted into the magnitudes eq. (A.9).

A.3 Model calculation (M2)

Model M1 assumes that the exciton behaves as a perfect two-level system. In Model M2 we introduce two major broadening mechanisms of the exciton and calculate their effects on the resonance lineshapes. One mechanism is a pure dephasing, i.e. an additional loss of exciton coherence in addition to radiative decay; the second mechanism is a spectral wandering, i.e. a temporal fluctuation of the bare exciton transition frequency ω_X . The dynamics under pure dephasing are governed by the Lindblad operator contribution proportional to γ_{pd} , the last term in eq. (A.2). We implement the spectral wandering by a convolution of the observable $\langle a^\dagger a \rangle$ with a distribution of ω_X with FWHM parameter γ_{sw} . As long as γ_{sw} is much smaller than the observed linewidths $\approx \kappa$, the details of the distribution shape are insignificant. For the sake of analytical simplicity, we choose a Lorentzian distribution.

The optical Bloch equations eq. (A.3) can be solved analytically for a nonzero pure dephasing rate γ_{pd} within the weak excitation regime. The ω_R dependence of the result is

$$\langle a^\dagger a \rangle = \langle a^\dagger a \rangle' + \frac{\mathcal{C}_{\text{pd}}}{|\omega_R - \omega'_+|^2 |\omega_R - \omega'_-|^2} \quad (\text{A.10})$$

where the primed expressions correspond to the previous results when γ_g is renormalized

by $\gamma_g \rightarrow \gamma_g + \gamma_{pd}$. The correction amplitude \mathcal{C}_{pd} is given by

$$\mathcal{C}_{pd} = 4|\epsilon|^2 g^4 \frac{\gamma_{pd}}{\gamma_g} \frac{\kappa + \gamma_g + \gamma_{pd}}{\kappa} \left[4g^2 \frac{(\kappa + \gamma_g)(\kappa + \gamma_g + \gamma_{pd})}{\kappa \gamma_g} + (\kappa + \gamma_g + \gamma_{pd})^2 + 4(\omega_C - \omega_X)^2 \right]^{-1}. \quad (\text{A.11})$$

In the experimental regime of the article ($g \approx 10 \mu\text{eV}$, $\kappa \approx 20 \mu\text{eV}$, $\gamma_g \approx 2 \mu\text{eV}$) we expect only a weak dependence of \mathcal{C}_{pd} on the experimental control parameters, namely the cavity detuning $\omega_C - \omega_X$.

The Lorentzian convolution $(*)$ of $\langle a^\dagger a \rangle$, eq. (A.7), with respect to ω_X with FWHM parameter γ_{sw} is based on the algebraic form of eq.(A.4a). Observing the identity

$$\left| \frac{\omega_X - A}{\omega_X - B} \right|^2 * \mathcal{L}_{sw} = \left| \frac{\omega_X - A'}{\omega_X - B'} \right|^2 - \frac{\pi \gamma_{sw}}{4} \frac{|A - B|^2}{\text{Im } B \text{ Im } B'} \mathcal{L}_{B'}(\omega_X) \quad (\text{A.12})$$

valid in the regime $\text{Im } A, \text{Im } B < 0$, we identify $A = \omega_R - i\gamma_g/2$ and $B = A + g^2/(\omega_C - \omega_R + i\kappa/2)$. The primed expressions are renormalized according to $\gamma_g \rightarrow \gamma_g + \gamma_{sw}$. Here, $\mathcal{L}_{B'}$ is a Lorentzian located at $\text{Re } B'$ with FWHM parameter $2 \text{Im } B'$. Similar to the pure-dephasing case, we find a corresponding algebraic structure

$$\langle a^\dagger a \rangle = \langle a^\dagger a \rangle' + \frac{\mathcal{C}_{sw}}{|\omega_R - \omega'_+|^2 |\omega_R - \omega'_-|^2} \quad (\text{A.13})$$

with the correction amplitude from spectral wandering

$$\mathcal{C}_{sw} = 4|\epsilon|^2 g^4 \frac{\gamma_{sw}}{\gamma_g} \left[4g^2 \frac{\kappa}{\gamma_g} + \kappa^2 + 4(\omega_R - \omega_C)^2 \right]^{-1}. \quad (\text{A.14})$$

Different to the pure dephasing case, the correction amplitude for spectral wandering \mathcal{C}_{sw} depends on $\omega_R - \omega_C$. However, as for \mathcal{C}_{pd} , the dependence on experimental parameters (ω_R, ω_C) is only weak as $g \approx \kappa \gg \gamma_g$.

Treating both correction amplitudes \mathcal{C}_{pd} , \mathcal{C}_{sw} as approximately constant, the emitter broadening induces, along with the renormalization of γ_g , a correction to the Lorentzian and dispersive lineshape constituents according to

$$\begin{aligned} \langle a^\dagger a \rangle &= \langle a^\dagger a \rangle' \\ &+ \text{Re } U_+ \mathcal{L}(\omega_R - \omega'_+) + \text{Im } U_+ \mathcal{D}(\omega_R - \omega'_+) \\ &+ \text{Re } U_- \mathcal{L}(\omega_R - \omega'_-) + \text{Im } U_- \mathcal{D}(\omega_R - \omega'_-) , \end{aligned} \quad (\text{A.15})$$

with amplitudes

$$U_{\pm} = \frac{\pi}{\text{Im } \omega'_{\pm}} \frac{\mathcal{C}}{(\omega'_{\pm} - \omega'_{\mp})(\omega'_{\pm} - \omega'^{*}_{\mp})} . \quad (\text{A.16})$$

From symmetry we find $\text{Im } U_{+} = -\text{Im } U_{-}$. In the strong coupling regime, and also for large cavity-emitter detuning, U_{\pm} is largely real valued. Hence we expect as the main signature of emitter broadening a significant increase of the Lorentzian lineshape contribution, while the dispersive lineshape constituent remains unaffected.

A.4 Contribution to signal from exciton decay

We address the role of the bare exciton population $\langle b^{\dagger}b \rangle$ whose contribution to the detection signal is expected to be negligible as the experiment is performed in a confocal detection scheme such that the coupling to the bare cavity mode only is efficient. From the model M1 eq. (A.4) we find

$$\frac{\langle b^{\dagger}b \rangle}{\langle a^{\dagger}a \rangle} = \frac{g^2}{(\omega_X - \omega_R)^2 + (\gamma_g/2)^2} , \quad (\text{A.17})$$

i.e. a parasitic contribution from $\langle b^{\dagger}b \rangle$ to the detection signal must show the following signatures: (i) be proportional to $\langle a^{\dagger}a \rangle$ and (ii) be strongly enhanced at $\omega_R \approx \omega_X$. Signature (i) is clearly not observed in the experiment: $\langle a^{\dagger}a \rangle$ is small in the polariton gap yet the deviation between M1 and the experimental data is largest here. Signature (ii) is not observed for strong cavity-exciton detuning where model M1 perfectly reproduces both cavity-like and exciton-like resonance amplitudes at $\omega_R = \omega_C$ and $\omega_R = \omega_X$, respectively. We thus conclude that the contribution of $\langle b^{\dagger}b \rangle$ cannot explain the most dominant deviations between model M1 and the experimental results.

A.5 Bare emitter optical properties

The analysis in Appendix A.3 was limited to the weak excitation regime where a broadening effect on the emitter can be quantified, while the underlying mechanism (pure dephasing or spectral wandering) remained ambiguous. This limitation is lifted in the strong excitation regime: when saturation effects become important a distinction can be made. The full cavity-coupled emitter dynamics are difficult to solve, however the bare emitter dynamics are readily accessible. The bare exciton emission under resonant

excitation – commonly referred to as resonance fluorescence – follows the Hamiltonian

$$\mathcal{H} = \hbar(\omega_X - \omega_R)b^\dagger b + \frac{\hbar\Omega}{2}(b^\dagger + b) , \quad (\text{A.18})$$

where Ω is the Rabi frequency of the resonant excitation of the emitter. As before, we introduce the radiative decay rate γ in freespace and pure dephasing rate γ_{pd} by Lindblad operators. The optical Bloch equations on the exciton population and coherence then read

$$\frac{d}{dt}\langle b^\dagger b \rangle = -\gamma\langle b^\dagger b \rangle - \frac{i\Omega}{2}\langle b^\dagger \rangle + \frac{i\Omega}{2}\langle b \rangle \quad (\text{A.19a})$$

$$\frac{d}{dt}\langle b^\dagger \rangle = \left[i(\omega_X - \omega_R) - \frac{\gamma + \gamma_{\text{dp}}}{2} \right] \langle b^\dagger \rangle + \frac{i\Omega}{2} - i\Omega\langle b^\dagger b \rangle . \quad (\text{A.19b})$$

The steady-state population results in a Lorentzian line

$$\langle b^\dagger b \rangle = \frac{\Omega^2 \bar{\gamma} / \gamma}{4(\omega_R - \omega_X)^2 + \bar{\gamma}^2 + 2\Omega^2 \bar{\gamma} / \gamma} , \quad (\text{A.20})$$

with the combined rate $\bar{\gamma} = \gamma + \gamma_{\text{pd}}$. The observed experimental linewidth Γ , when the emitter is subject to an additional broadening due to spectral wandering γ_{sw} , is after Lorentzian convolution

$$\Gamma = \sqrt{\bar{\gamma}^2 + 2\Omega^2 \bar{\gamma} / \gamma} + \gamma_{\text{sw}} . \quad (\text{A.21})$$

The resonance fluorescence peak intensity $I = \beta\langle b^\dagger b \rangle$ at resonance $\omega_R = \omega_X$ is given by

$$I = \beta \frac{\Omega^2}{\bar{\gamma}\gamma + 2\Omega^2} \times \frac{\Gamma - \gamma_{\text{sw}}}{\Gamma} \quad (\text{A.22a})$$

$$= I_{\text{sat}} \left(1 - \left[\frac{\Gamma_0 - \gamma_{\text{sw}}}{\Gamma - \gamma_{\text{sw}}} \right]^2 \right) , \quad (\text{A.22b})$$

where I_{sat} is the peak intensity at saturation for $\Omega \gg \gamma$, $\Gamma_0 = \gamma + \gamma_{\text{pd}} + \gamma_{\text{sw}}$ is the linewidth for $\Omega \rightarrow 0$, and β is the overall instrumentation factor. Equation (A.22b) expresses the power-dependent resonance fluorescence intensity I in terms of convenient observables I_{sat} and Γ , where β and the Rabi frequency Ω have been eliminated. In the case $\gamma_{\text{sw}} = 0$, the intensity I yields a linear relation to Γ^{-2} with intersects at I_{sat} and T_2 -limited rate $\bar{\gamma}$. A non-vanishing spectral wandering rate $\gamma_{\text{sw}} \neq 0$ violates the linear relation, allowing γ_{sw} to be used as a robust fitting parameter.

We investigate the spectral wandering of single quantum dots in the same sample area

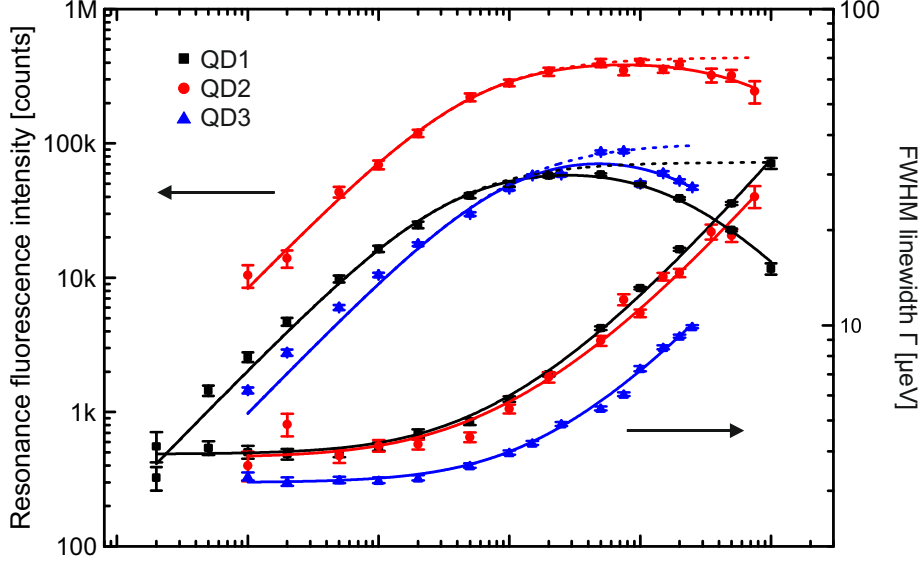


Figure A.2. Resonance fluorescence peak intensity (left scale) and FWHM linewidth (right scale) for three investigated quantum dots (symbols). The peak intensity dependence with resonant pump power matches a three-level-description to a high degree, where the assumed third level is nonresonantly pumped (solid lines). From the three-level description we extrapolate to the corresponding two-level dynamics (dashed lines) where the third level is eliminated from the dynamics. The linewidth dependence with resonant pump power is already well reproduced by the two-level description.

and wavelength as in the microcavity experiment of the article. Although the very same quantum dot cannot be conserved between configurations, we assume a close statistical resemblance.

Figure A.2 shows as symbols the peak resonance fluorescence intensity I as a function of the resonant excitation power P for three different quantum dots as well as their corresponding resonance FWHM linewidths. Additional with the resonant excitation, we require an ultraweak non-resonant excitation to observe the resonance fluorescence, as was the case in the experiment in the article. Beyond saturation at about 10 nW of monitored resonant excitation power, the resonance fluorescence peak intensity drops with further increase in excitation power, in contrast to the two-level model. We attribute this breakdown to a spurious coupling to a third level (e.g. a different charge state, either of the quantum dot or the environment). Indeed from a simple rate equation model, where a third state is non-resonantly driven from either the upper or lower level at smaller rate ϵP , the steady-state population of the upper level is

$$I_3 = \beta \frac{(1 + \epsilon \eta_1)P}{\xi_0 + (2 + \epsilon \xi_1)P + \epsilon \xi_2 P^2}, \quad (\text{A.23})$$

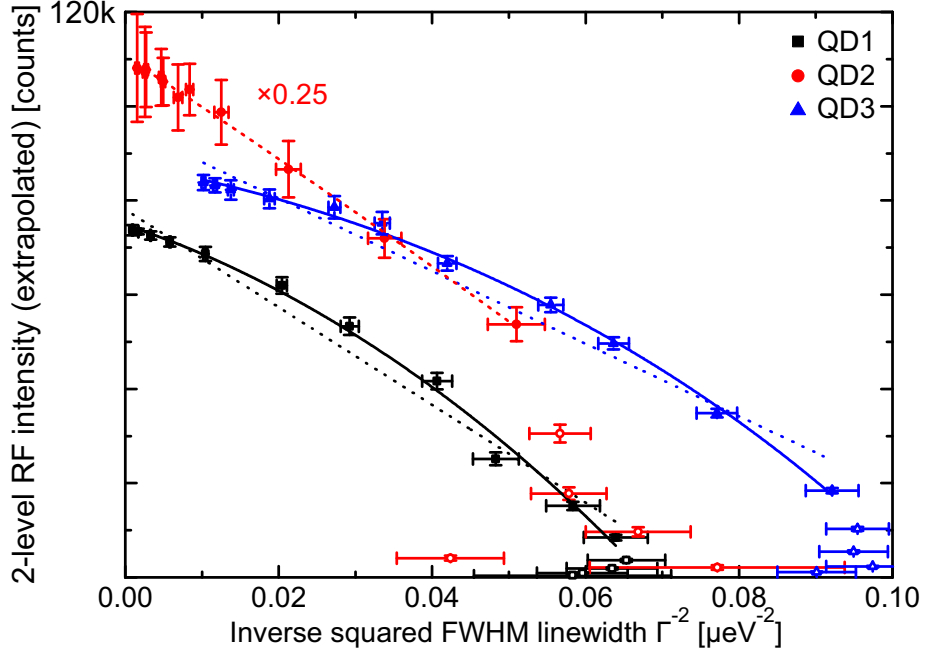


Figure A.3. Measurement of the resonance fluorescence peak intensity versus the inverse squared linewidth (symbols) for the three investigated quantum dots. A vanishing spectral wandering rate yields a linear relation (dotted line), while the experimental data is consistent with a spectral wandering rate of $\approx 1.5 \mu\text{eV}$ for QD₁ and QD₃. On QD₂ no consistent determination of the spectral wandering rate is found. The open symbols at very low resonant excitation power have been disregarded from the fit, as the collected intensity is dominated by photoluminescence from an ultraweak non-resonant excitation scheme.

where the coefficients $\eta_1 < 1$ and ξ_i depend on the details of the relaxation rates. The power dependence of I_3 in eq. (A.23) is quantitatively well reproduced in the experimental data. Under the assumption $\epsilon\eta_1, \epsilon\xi_1 \ll 1$ we determine ξ_0 and $(\epsilon\xi_2)^{-1}$ (see Table A.1). Taking the limit $\epsilon\xi_2 \rightarrow 0$, this allows us to extrapolate from the resonance fluorescence intensity I_3 of the three-level system the expected resonance fluorescence intensity $I_2 = P/(\xi_0 + 2P)$ of an effective two-level system where the third level contribution is eliminated. The extrapolated intensity is shown in figure A.2 as dashed line. In terms of resonance linewidth, the experimental data show no significant deviation from a two-level description.

Figure A.3 shows as symbols the resonance fluorescence intensity as a function of the inverse squared linewidth Γ^{-2} for the three investigated quantum dots (filled symbols). At very low resonant excitation powers, the collected intensity is dominated by the photoluminescence intensity from the additional ultraweak non-resonant excitation scheme. For this reason, we discard the data for very low collected intensities (open

Table A.1. Experimental results on the bare emitter system for QD₁₋₃.

Quantity	Unit	QD ₁	QD ₂	QD ₃
λ	nm	941.79	937.41	939.04
ξ_0	nW	7.0 ± 0.5	10.3 ± 0.9	20.3 ± 6.5
$(\epsilon\xi_2)^{-1}$	μW	0.111 ± 0.09	0.55 ± 0.08	0.113 ± 0.051
Γ_0	μeV	3.84 ± 0.04	3.17 ± 0.08	3.10 ± 0.02
γ_{sw}	μeV	1.4 ± 0.3	0.2 ± 0.3	1.5 ± 0.1
γ_{pd}	μeV	≈ 1.6	—*	≈ 0.8

* No consistent determination of γ_{sw} was found for QD₂.

symbols). Applying the relation eq. (A.22b) to the data, for QD₁ and QD₃, the relation is well reproduced for $\gamma_{\text{sw}} = 1.5 \pm 0.1 \mu\text{eV}$ and $1.4 \pm 0.2 \mu\text{eV}$ respectively (solid line). For comparison the best fit for $\gamma_{\text{sw}} = 0$ (dotted line) is in clear contradiction to the experimental data. For QD₂ no significant spectral wandering is observed, however we note that the relative error on the resonance fluorescence intensity is considerably larger than for the other QDs and no consistent behaviour at low intensity is found. Thus on QD₂ no reliable estimation of the spectral wandering rate can be obtained. The T_2 -limited linewidth $\bar{\gamma} = \gamma + \gamma_{\text{pd}} = \Gamma_0 - \gamma_{\text{sw}}$ evaluates to $\approx 2.44 \mu\text{eV}$ ($1.6 \mu\text{eV}$) for QD₁ (QD₃). As the transform-limited radiative decay rate $\gamma \approx 0.8 \mu\text{eV}$, we estimate a corresponding pure dephasing rate of $\gamma_{\text{pd}} \approx 1.6 \mu\text{eV}$ ($\approx 0.8 \mu\text{eV}$) for QD₁ (QD₃).

In summary, we observe that spectral wandering is likely to represent a dominating broadening mechanism in the investigated sample. This result underlines the major statement of the article: the cavity-coupled exciton cooperativity can be readily enhanced if the additional emitter broadening, identified as spectral wandering, can be reduced.

Acknowledgments

At this point I would like to thank all the people that helped me one way or the other to finish this thesis. First and foremost, I want to express my gratitude to Richard Warburton for accepting me as a PhD student in his group. I could always count on his support and profit a lot from the fair and inspirational leadership style. Many thanks to Peter Lodahl from the Niels Bohr Institute in Copenhagen for taking the time to read my thesis and being a part of the PhD committee.

A lot of people were directly involved in this project and made a significant contribution to the results presented in this thesis. Many thanks to Sebastian Starosielec for being such a pleasant and patient co-worker. In countless discussion with you I could really profit a lot from your clear way of analytical thinking. I am sure that without your effort and skills we would not understand the strong coupling data as thoroughly as we do now. Also many thanks to Arne Ludwig, who was a post doc in the beginning of the cavity project. Your creative ideas were fundamental for the successful fabrication of the curved mirrors and the functioning of the microcavity. I was very glad that the cooperation also went on when you moved back to the Ruhr-Universität in Bochum. Thanks to Sascha Valentin for growing our samples and for showing us how to develop a working ELO procedure. In the context of this project, I also had the pleasure to supervise a few Master students, whereas I probably profited more from them than they did from me. Thank you Dominik Rohner and Luc Dümpelmann, the cavity development process really sped up when the two of you joined the microcavity team. Daniel Najer, thanks for your hard work in the ELO process and characterization of the cavity. I am sure you will reach an extremely high cooperativity very soon. All the best to you and your new family.

I owe special thanks to the first generation of PhD students in Richards Group in Basel: Andreas Kuhlmann, Gunter Wüst and Jonathan Prechtel. It was really enjoyable to work with you and to spend time outside the lab together. Thank you Andi for patiently sharing your expertise. Gunter, I profited a lot from your skills in the lab and also when it came down to repairing my mountain bike. Johnny, thank you for all your help and

for always being up for a competition in the various sports we did together. I also want to thank the people that have joined the group in the last years and contributed to a great working atmosphere. Thank you Julien Houel, Mathieu Munsch, Timo Kaldewey, Daniel Riedel, Jan-Philipp Jahn, Martina Renggli and Marta Arcari.

I think it is safe to say that the work presented in this thesis would not have been possible without the great effort of the technicians that are working at the department. Many thanks to Sascha Martin, your innovation and effort was essential for the stability and functioning of our microcavity setup. Patrick Stöcklin, Stephan Gentsch and Dominik Sifrig thank you for always being so uncomplicated and helpful. Many thanks go to Willy Tschudin for cutting the silica substrates into a manageable size. Further thanks to Michael Steinacher and all the members of the electrical workshop for their support and helpful advice. I also want to thank IT specialist Beat Glatz for always being supportive when I was responsible for the computers in our group.

I further want to thank my former roommates Lucas, This, Tinu, Philipp and Simone for the wonderful time we had together (especially on Thursday evenings). Special thanks to Carlos, Damian, Nico and all friends that accompanied me in any way. Finally, I am deeply grateful to my family for the unconditional support I always could count on in all these years.

Curriculum Vitae

Lukas Emanuel Greuter

Department of Physics
University of Basel
Klingelbergstrasse 82
4056 Basel
Switzerland

Personal Information

Birth: July 22, 1985
Place of birth: Zürich, Switzerland
Nationality: Swiss
Hometown: Zürich, ZH

Education

2015 **PhD in Experimental Physics**
University of Basel, Switzerland
Advisor: Prof. Richard J. Warburton
Thesis: *Self-assembled quantum dots in a fully tunable microcavity*

2010 **MSc Thesis**
Delft University of Technology, Netherlands
Advisor: Prof. Lieven M.K. Vandersypen
Thesis: *Towards electron shuttling in a triple quantum dot*

2010 **Master of Science** Nanoscience, University of Basel, Switzerland

2009 **Bachelor of Science** Nanoscience, University of Basel, Switzerland

2004 **Matura**, Gymnasium Münchenstein, Switzerland

List of Publications

1. J. Houel, A. V. Kuhlmann, L. Greuter, F. Xue, M. Poggio, B. D. Gerardot, P. A. Dalgarno, A. Badolato, P. M. Petroff, A. Ludwig, D. Reuter, A. D. Wieck, and R. J. Warburton,
Probing single-charge fluctuations at a GaAs/AlAs interface using laser spectroscopy on a nearby InGaAs quantum dot,
[Physical Review Letters **108**, 107401 \(2012\)](#).
2. A. V. Kuhlmann, J. Houel, A. Ludwig, L. Greuter, D. Reuter, A. D. Wieck, M. Poggio, and R. J. Warburton,
Charge noise and spin noise in a semiconductor quantum device,
[Nature Physics **9**, 570 \(2013\)](#).
3. J. H. Prechtel, A. V. Kuhlmann, J. Houel, L. Greuter, A. Ludwig, D. Reuter, A. D. Wieck, and R. J. Warburton,
A frequency-stabilized source of single photons from a solid-state qubit,
[Physical Review X **3**, 041006 \(2013\)](#).
4. L. Greuter, S. Starosielec, D. Najer, A. Ludwig, L. Duempelmann, D. Rohner, and R. J. Warburton,
A small mode volume tunable microcavity: Development and characterization,
[Applied Physics Letters **105**, 121105 \(2014\)](#).
5. L. Greuter, S. Starosielec, A. V. Kuhlmann, and Richard J. Warburton,
Towards high cooperativity strong coupling of a quantum dot in a small tunable microcavity,
Submitted, [arXiv:1504.06223 \(2015\)](#).
6. L. Greuter, D. Najer, A. V. Kuhlmann, S. Starosielec, S. Valentin, A. Ludwig, D. Wieck, and R. J. Warburton,
Epitaxial lift-off for solid-state cavity quantum electrodynamics,
Submitted, [arXiv:1505.00658 \(2015\)](#).